2013

Engineering And Application Of Ultrafast Laser Pulses And Filamentation In Air

Nicholas Barbieri
University of Central Florida

STARS Citation

Barbieri, Nicholas, "Engineering And Application Of Ultrafast Laser Pulses And Filamentation In Air" (2013). *Electronic Theses and Dissertations, 2004-2019*. 2956.
https://stars.library.ucf.edu/etd/2956

ENGINEERING AND APPLICATION OF ULTRAFAST LASER PULSES AND FILAMENTATION IN AIR

by

NICHOLAS PAUL BARBIERI
B. S. Florida Atlantic University, 2003
M. S. University of Central Florida, 2006
M. S. Georgia Institute of Technology, 2008
M. S. University of Central Florida, 2010

A dissertation submitted in partial fulfillment of the requirements
for the degree of Doctor of Philosophy
in the Department of Physics
in the College of Science
at the University of Central Florida
Orlando, Florida

Spring Term
2013

Major Professor: Martin Richardson

ABSTRACT

Continuing advances in laser and photonic technology has seen the development of lasers with increasing power and increasingly short pulsewidths, which have become available over an increasing range of wavelengths. As the availability of laser sources grow, so do their applications. To make better use of this improving technology, understanding and controlling laser propagation in free space is critical, as is understanding the interaction between laser light and matter.

The need to better control the light obtained from increasingly advanced laser sources leads to the emergence of beam engineering, the systematic understanding and control of light through refractive media and free space. Beam engineering enables control over the beam shape, energy and spectral composition during propagation, which can be achieved through a variety of means. In this dissertation, several methods of beam engineering are investigated. These methods enable improved control over the shape and propagation of laser light. Laser-matter interaction is also investigated, as it provides both a means to control the propagation of pulsed laser light through the atmosphere, and provides a means to generation remote sources of radiation.

ACKNOWLEDGMENTS

I would like to acknowledge guidance and support of my advisor Dr. Richardson for whom my research projects would not be possible. He has been a very patient and understanding advisor and has been very helpful in shaping my graduate career.

I would like to thank Dr. Christodoulides, Dr. Shivamoggi and Dr. Heinrich for serving on my dissertation committee.

Dr. Christodoulides provided much of the initial theoretical background needed to begin my investigation into non-diffracting and helical beams. Without his assistance, I would have never undertaken research into helical beams and a large portion of the research that comprises this dissertation would have never been carried out. I am very grateful for his generosity.

Dr. Shivamoggi is has provided me with a lot of support of the past 5 years. He has provided me with considerable theoretical assistance, he has instructed several upper level graduate courses I have taken, and has provided me with excellent personal and professional advice over the course of my doctoral studies.

I would also like to acknowledge the support of my colleagues in the Filament Engineered Propagation Team, especially Matthew Weidman, Kahn Lim, Matthieu Baudelet and Magali Durand. Without their support I would not have been able to carry out any of my research.

I would also like to acknowledge the support of our collaborators at Clemson: Zahra Hosseinimakram, Zachary Roth and Dr. Eric Johnson for designing and fabricating the specialized optics used in my beam engineering experiments.

I would like to thank the rest of the Laser Plasma Laboratory for their support. My colleagues within LPL have always been willing to lend their time and knowledge to my endeavors when asked.

I would like to thank the entire CREOL faculty for their willingness to assist both my fellow students and I with their knowledge and expertise.

To my family: Paul Barbieri, Jean Barbieri, Michael Barbieri, Emily Barbieri and Stephen Barbieri for supporting me in all my endeavors.

TABLE OF CONTENTS

LIST OF FIGURES ix

LIST OF TABLES xii

CHAPTER 1: INTRODUCTION 1

- 1.1 Summary of Dissertation 4

CHAPTER 2: EQUIPMENT AND FACILITIES 5

- 2.1 Ultrafast Pulses and Their Associated Physics 5
- 2.2 Ultrafast Lasers 9
- 2.2 The MTFL Laser 13
  - 2.2.1 Oscillator 14
  - 2.2.2 Stretcher/Compressor 15
  - 2.2.3 Amplifiers 15
- 2.3 The Terawatt Laser 16
  - 2.3.1 Oscillator 16
  - 2.3.2 Stretcher/Compressor 17
  - 2.3.3 Terawatt Amplifiers 18
- 2.4 Laser Range 20
- 2.5 Beam Imaging Systems 21

CHAPTER 3: NON-DIFFRACTING BEAMS, BESSEL BEAMS, AND HELICAL BEAMS 24

- 3.1 Diffraction Theory 25
- 3.2 Consequences of Diffraction 27
- 3.3 Bessel Beams 28
- 3.4 Generating Bessel Beams through Spatial Filtering 31
- 3.5 Bessel Beam Generation Using an Axicon Lens 34
- 3.6 Helical Beams 40
- 3.7 Coaxial Helical Beam Synthesis 43
- 3.8 Longitudinal Compression Due to the Addition of a Lens 50
- 3.9 Numerical Modeling of Helical Beams 53
- 3.10 Helical Beam Experimental Setup 56

3.11 Helical Beam Experimental Results 60
3.12 Conclusion 63
CHAPTER 4: LASER FILAMENTATION IN AIR 64
4.1 Filament Characteristics 64
4.2 Filamentation Physics 66
4.3 Nonlinear Schrodinger Equation 68
4.4 Ionization within a Filament 70
4.5 Effects of the Plasma on Filament Propagation 74
4.6 Rayleigh-Sommerfeld Model 75
4.7 Helical Filaments 81
CHAPTER 5: REMOTE GENERATION OF RF RADIATION USING FILAMENTS 91
5.1 RF Generation Model 93
5.2 RF Detection and Measurement 103
5.3 Terawatt Filament Experiments 106
5.4 High Frequency Experiments 110
5.5 Focal Length Resolved FIRF Experiments 116
5.6 Conclusion 124
CHAPTER 6: MICROWAVE GUIDING USING FILAMENTS 126
6.1 Filaments as Waveguiding Elements 127
6.2 Synthesis of Guiding Structures 128
6.3 Filament Transmission Line 129
6.4 Waveguiding Using Filaments 136
6.5 Index Guiding Using Filaments 141
CHAPTER 7: CONCLUSION 147
7.1 Contingencies 149
7.2 Future Prospects 150
7.2.1 Fresnel Axicons 151
7.2.2 Photonic Time-Stretch Microwave Detection 152
APPENDIX A: PHYSICAL CONSTANTS 155
APPENDIX B: GAS PROPERTIES 157
APPENDIX C: KNOWN INTEGRALS 159

APPENDIX D: METHOD OF STATIONARY PHASE 161
APPENDIX E: NONLINEAR SCHRODINGER EQUATION 163
APPENDIX F: WAVEGUIDING EQUATIONS 169
REFERENCES 174

LIST OF FIGURES

Figure 1: The MTFL laser. 13
Figure 2: Technical layout of the MTFL laser. 14
Figure 3: Layout of the terawatt oscillator 17
Figure 4: Terawatt pulse stretcher. 18
Figure 5: Terawatt pulse compressor. 18
Figure 6: Terawatt regenerative amplifier layout. 19
Figure 7: Layout of the various LPL lasers (including MFTL and TW), the laser range, and end station diagnostics. 20
Figure 8: End station located at the end of the 50 m end range. 21
Figure 9: Initial transverse imaging setup. 22
Figure 10: Modified transverse imaging setup. 23
Figure 11: Geometric illustration of the diffraction-free length of a Bessel beam generated from an axicon illuminated with a Gaussian beam. 38
Figure 12: Geometric representation of the linear scaling of on-axis Bessel beam irradiance with propagation distance. 39
Figure 13: The transverse irradiance (top) and phase (bottom) profiles of order ± 1 *Bessel beams and their resulting superposition (right).* 41
Figure 14: Conceptual layout of an optical configuration used for helical beam synthesis 43
Figure 15: Transformation of the propagation axis illustrating the effect of a lens on non-diffracting beam generation. The propagation axis is compressed as it approaches the Fraunhofer plane. For originally periodic non-diffracting beams, this results in a decrease in beam period during propagation. 52
Figure 16: Fresnel diffraction simulation flowchart. 55
Figure 17: Optical setup used to generated and characterize continuous and pulsed helical beams. TL1 and TL2 form a telescope which increases the beam diameter by a factor of 3. 57
Figure 18: Three-dimensional color map renderings of the surface of the two vortex plates used in experiments. The sign azimuthal charge associated with each plates can be switched by inverting the plate orientation. 58
Figure 19: Transverse helical beam profiles as a function of propagation distance obtained using the setup shown in Figure 17 from both simulation and experiment. Upper Row: Simulation, Middle Row: Continuous Beam, Bottom Row: Pulsed Beam 61
Figure 20: Cumulative rotation angle as a function of propagation distance. The way in which the rotation angle is defined is show on the right figure, while the data is plotted in the left figure. 62
Figure 21: Filament beam waist as a function of propagation distance, as obtain from the Rayleigh-Sommerfeld model and experiment. 79
Figure 22: Transverse beam profiles obtained from simulation and experiment at the beginning of the filament. 80
Figure 23: Experimental Setup 82

Figure 24: Optical setup used to record transverse images of high peak power and filamenting ultrafast pulses. 83
Figure 25: Layout and dimensions of the electrodes used to evaluate filament plasma density. 84
Figure 26: Electrode driving circuit. High-voltage is applied across VDC. Signal is measured by monitoring the voltage drop across the variable resistor. 85
Figure 27: Protection and amplification circuit used to evaluate the voltage drop obtained from the electrode driver circuit. 85
Figure 28: Helical beam transverse profiles as a function of propagation distance. Helical beams generated using 133 uJ pulses are shown in the upper figure associated with each distance, those obtained using 11.9 mJ pulses are shown in the lower figures. 86
Figure 29: Helical beam cumulative rotation angle as a function of propagation distance. 87
Figure 30: Fluence as a function of propagation distance, both both 133 uJ pulses (left) and 11.9 mJ pulses (right). Both plots share the same scale. 88
Figure 31: Ionization signal strength as a function of beam propagation distance. A typical ionization signal is shown on the left, while aggregate data is shown on the right. 89
Figure 32: Nitrogen fluorescence obtained when a telescope with a 40 cm equivalent focal length was used in conjunction with the helical beam synthesizer. Two longitudinally separate ionization peaks can clearly be observed. 90
Figure 33: Illustrated summary of the model used to evaluate filament-matter induced RF radiation. 94
Figure 34: Code flow chart describing the filament matter induced RF radiation simulation. 101
Figure 35: Horn antennas used in all RF experiments. 103
Figure 36: Heterodyne signal processing system used to evaluate RF radiation. 104
Figure 37: Experimental setup used to evaluate filament induced RF radiation in the Terawatt experiments. 106
Figure 38: Raw oscilloscope traces. 107
Figure 39: Spectral measurements of laser-matter induced RF radiation, conducted using a horizontally polarized antenna. 108
Figure 40: Spectral measurements of laser-matter induced RF radiation, conducted using a vertically polarized antenna. 109
Figure 41: Experimental setup used to evaluate 21-35 GHz laser filament induced RF radiation. 111
Figure 42: Sample time domain measurement of filament induced RF radiation and corresponding spectra. 112
Figure 43: Filament induced RF radiation evaluated at several orientations relative to the surface normal for irradiated copper. 113
Figure 44: FIRF measurements taken out of the horizontal plane. 114
Figure 45: Orientation of RF polarizations in spherical coordinates. 115
Figure 46: Experimental setup used to evaluate the effect of focality on filament induced RF radiation. 118
Figure 47: Time domain samples collected for a 50 cm focal length lenses. 120

Figure 48: RF spectra generated from laser-matter interaction with copper lying within the focal plane of a spherical lens. For each lens evaluated, 30 spectra where recorded and averaged. RF radiation background measurements are shown in yellow, while RF signal measurements are given in blue. 121
Figure 49: Integrated RF pulse field strength as a function of focal length. 122
Figure 50: Comparison of simulation results to data for filament-matter induced RF radiation. 123
Figure 51: Depiction of a twin-lead line with relevant dimensions. 131
Figure 52: Frequency dependent propagation losses of twin-lead filament lines of various spacings ... 133
Figure 53: Frequency dependent losses of twin-lead lines of various spacings possessing conductivity 100 times that of unaugmented laser filaments. 134
Figure 54: Irradiance profile of a higher order Bessel beam (left) and the filament array resulting from the propagation of a 12th order Bessel beam in water recorded by Shiffler et al. [139] 140

LIST OF TABLES

Table 1: Total spectral irradiance as a function of laser polarization and orientation relative to the target for horizontally polarized copper measurements. 116

CHAPTER 1: INTRODUCTION

Continual advances in ultrafast laser technology have resulted in a wide range of laser systems suitable both for laboratory experiments and practical applications. Making optimal use of this technology requires continually improving the understanding of how ultrafast laser pulses behave, both during propagation and during their interaction with matter.

The propagation of light is dictated and limited by diffraction physics [1]. Diffraction represents a fundamental limit in the transport and application of electromagnetic waves. Diffraction dictates the distance a confined beam of light can be transported, the minimum area an electromagnetic wave may be confined, and the interaction between electromagnetic waves and obstructions. Diffraction limits can be readily overcome using waveguiding structures, such as optical fiber [2]. Overcoming diffraction in free space or in homogeneous optical media is considerably more difficult, but a wide variety of techniques are available to manage diffraction effects under these circumstances.

Non-diffracting beams are obtained from linear optical techniques which employ Eigen modes of the Helmholtz wave equation in the generation of waves for which a limited region is impervious to the effects of diffraction [3]. The applications of non-diffracting beams range from enabling the propagation of individual features of an electromagnetic wave well beyond the Rayleigh limit [4] to the curving [5] and twisting of light during propagation [6]. As a linear phenomenon, non-diffracting beams can be employed in both vacuum and material media. However, non-diffracting beams require optics with apertures that are typically far larger than the transverse diameter of the non-diffracting effect being produce, and must still collectively transport energy and momentum in the direction of propagation.

Laser filamentation exploits the interplay of several nonlinear effects in transparent media to guide confined beams of light well beyond the Rayleigh range [7] [8], enabling propagation of beams a few hundred micrometers in diameter over distances as large as several kilometers [9]. Laser filamentation is a result of an induced inhomogeneous refractive index obtained through the optical Kerr effect, which acts as a focusing lens, and refractive index modifications arising from a breakdown plasma once sufficient beam irradiance is achieved, which acts to counteract the Kerr effect and prevent further reduction of the beam diameter [10]. Once a stable beam diameter is obtained, the filament propagates until losses in the breakdown plasma reduce beam power to the point in which the nonlinear effects can no longer be maintained. In addition to their application as a long distance beam guiding mechanism, the breakdown plasma resulting from the filamentation process can be used as a temporary conductive channel for a variety of purposes, including the guiding of electric discharges in air [11] [12], and the confinement and guiding of microwaves through free space [13]. Because of the large instantaneous power required to drive the nonlinearities responsible for filamentation, in practice only ultrafast lasers or pulsed ultraviolet lasers are used to generate laser filaments. As a nonlinear effect, filamentation cannot be employed in vacuum, but is suitable for propagation in air, water and glass among other transparent media.

Remote generation of radiation enables the bypass of diffraction effects. By using intense radiation to produce ionization, it is possible to produce temporary plasmas which serve as broadband radiation sources [14]. When these remote sources are used, the relevant diffraction effects will now apply to the spatial arrangement of the new source. Such remote plasmas also serve as a source of radiation frequencies which may not have been originally available [15] [16] [17]. However, generating radiation in this manner is subject to rather large conversion losses.

In transparent media, nonlinear effects can be employed to generate temporary guiding structures that operate as analogs to more conventional waveguides and transmission lines. These guiding structures can then be used to improve the confinement of electromagnetic wave propagation. Index guiding structures can be obtained through inhomogeneous modification of the refractive index through specially shaped pulsed beams, properly arranged arrays of pulsed beams, or arrays of laser filaments [18]. Transmission lines and conductive waveguides can be obtained from organized arrays of transient breakdown plasmas, which can be readily obtained using laser filaments [12]. In both cases, the physics of the relevant guiding devices will dictate the modified wave propagation. Because of the limited control available over refractive index and plasma conductivity available through laser modified nonlinear effects, the transient guiding structures will suffer from suboptimal properties resulting in inferior guiding of electromagnetic radiation when compared to their physical counterparts.

1.1 Summary of Dissertation

A limited investigation into each of these topic areas was conducted. Non-diffracting beams are discussed in Chapter 3, with an emphasis on Bessel beams and a new class of non-diffracting beam structures obtained from a Bessel beam superposition, helical beams. Chapter 4 discusses filamentation and the use of diffraction free beams in general and helical beams in particular for enhancing and controlling laser filamentation. Chapter 5 discusses the application of laser filaments for the remote generation of radio frequency radiation. The use of non-diffracting beams and filaments in the synthesis of radio frequency and microwave structures is discussed in Chapter 6, completing the investigation. Chapter 2 summarizes the equipment and facilities used in this study.

CHAPTER 2: EQUIPMENT AND FACILITIES

A large range of experimental equipment and facilities were used over the course of this investigation. Two separate laser systems were employed. Multiple laser ranges were used to study propagation, and several imaging systems were used to evaluate beam shape and profile. High voltage electrodes and electronics were used to evaluate the ionization of laser filaments. To evaluate remotely generated radio frequency radiation, broadband horn antennas were used in conjunction with a specialized analog signal processing system and a single shot oscilloscope. Equipment not discussed in this section will be described in the relevant chapters.

2.1 Ultrafast Pulses and Their Associated Physics

Laser pulses lasting a few picoseconds or less are generally referred to as ultrafast pulses. Excluding high-harmonic generation, ultrafast pulses vary in duration from several picoseconds for modelocked fiber lasers [19] to a few femtoseconds for few cycle modelocked solid-state lasers [20] [21]. Ultrafast pulses provide a number of practical and experimental advantages over the use of continuous laser beams and longer duration laser pulses. The short pulse duration enables the use of ultrafast pulses as high time resolution probes, providing detailed temporal information on physical events that would be too fast to resolve otherwise [22] [23]. Ultrafast pulses also provide an efficient means of laser machining, as the entirety of the pulse energy can be deposited in a material and induce changes before thermal conduction can draw energy from the machining site [24] [25]. The short duration of the pulses also enable efficient energy compression, allowing the extraction of gigawatt to pettawatt instantaneous powers from millijoule to joule level pulse energies [26]. The high instantaneous power obtained from these pulses can then be used to drive nonlinear processes, dielectric breakdown, laser filamentation or other physical processes which are dependent upon instantaneous power, irradiance or electric field strength.

Ultrafast pulses are composed of the simultaneous, synchronized oscillation of a large number of cavity modes, which are obtained using modelocked oscillators. The pulse duration extracted from the oscillator is inversely proportional to the bandwidth spanned by the active cavity modes. Collectively, the temporal and spectral pulse width are limited by the time-bandwidth product. For a Gaussian pulse of temporal pulse width τ

$$E(t) = E_0 \exp\left(-\frac{t^2}{\tau^2}\right) \tag{1}$$

the corresponding spectra will be

$$E(\omega) = E_0' \exp\left[-\frac{\omega^2}{(\Delta\omega)^2}\right] = E_0\sqrt{\frac{2}{\tau}} \exp\left[-\frac{\omega^2}{\left(\frac{2}{\tau}\right)^2}\right] = \mathcal{F}\left[E_0 \exp\left(-\frac{t^2}{\tau^2}\right)\right] \tag{2}$$

This immediately leads to the time bandwidth product limitation for Gaussian beams

$$\tau\Delta\nu = \frac{\tau\Delta\omega}{2\pi} = \frac{1}{\pi} \tag{3}$$

Femtosecond pulses are by definition obtained when

$$\tau < 1\, ps \tag{4}$$

Substituting this value into Equation 3 gives the minimum bandwidth possessed by a femtosecond pulse

$$\Delta\nu > 318\,GHz \tag{5}$$

Applying the relation

$$\Delta\nu = c\frac{\Delta\lambda}{\lambda^2} \tag{6}$$

the bandwidth requirements at 800 nm can alternatively be expressed as

$$\Delta\lambda > 678\,pm \tag{7}$$

The ultrafast lasers used in this study have pulse durations ranging from 30 fs to 100 fs, thus having minimum spectral bandwidths of $\sim 20\,nm$ and $\sim 7\,nm$, respectively. When propagating through matter, the large pulse spectral bandwidth can undergo severe dispersion, which often requires compensation.

Because of the large instantaneous power and irradiances readily obtained with ultrafast pulses, optical nonlinearities will readily manifest themselves when propagating ultrafast pulses through material media. At low irradiance, there are no differences between propagation in vacuum and media save the reduction in wavelength resulting from the change in refractive index and the effects associated with them. Propagation is entirely dictated by the Helmholtz equation and diffraction. Of particular importance is that the spectral composition of the pulse is maintained in the linear case; no additional spectral components can be generated under linear conditions.

Once the pulse irradiance is sufficient to drive nonlinearities, a large number of new optical phenomenon are obtained. The Kerr effect modifies the diffraction of light, while self-phase modulation, three-wave mixing and four-wave mixing generate new spectral components. For particular strong laser fields, dielectric breakdown and plasma generation can occur. In general, these nonlinearities can be treated using the modified Helmholtz equation [27]

$$\nabla^2\vec{E} - \frac{n^2}{c^2}\frac{\partial^2\vec{E}}{\partial t^2} = \frac{1}{\epsilon_0 c^2}\frac{\partial^2\vec{P}_{NL}}{\partial t^2} \tag{8}$$

The left hand side of Equation 8 is the Helmholtz equation, while the nonlinearities are incorporated by the nonlinear polarization term on the right hand side.

The optical Kerr effect is an increase in the refractive index driven by the laser field. In its simplest form, the Kerr effect is expressed as

$$n = n_0 + n_2 I \tag{9}$$

where n is the nonlinear refractive index, n_0 is the linear refractive index in the absence of the laser field, n_2 is the Kerr index, and I is the instantaneous irradiance. In air, the Kerr index takes a value of $n_2 = 3 \cdot 10^{-19}\ cm^2/W = 30\ \mu m^2 \cdot fs/mJ$ [28] [29]. For a 50 fs pulse, a fluence of $1500\ mJ/\mu m^2$ is required to obtain a value of unity for the Kerr effect, thus millijoule level ultrafast pulses are typically required to observe this effect in air.

Spatially inhomogeneous fields of sufficient irradiance will generate non-uniform spatial refractive index distributions, modifying the diffraction behavior of light. One of the most common behaviors obtained as a consequence of the Kerr-effect is self-focusing, where the higher irradiances obtained at the center of Gaussian and similarly shaped laser pulses induces a refractive index profile analogous to that obtained using a lens, leading to the focusing of collimated laser pulses during propagation.

Additional frequencies can be generated from an optical field through the second and third order polarization nonlinearities, typically expressed as

$$\vec{P}^{(2)}(t) = 2\epsilon_0\chi^{(2)}\vec{E}\vec{E}^* \tag{10}$$

$$\vec{P}^{(3)}(t) = \epsilon_0\chi^{(3)}\vec{E}\vec{E}\vec{E}^* \tag{11}$$

Expressing the electric field as a pair of spectral tones

$$\vec{E} = \vec{E}_0[\cos(\omega_1 t) + \cos(\omega_2 t)] \tag{12}$$

A series of new spectral tones will be generated

$$P^{(2)}(t) \propto \cos(2\omega_1 t) + \cos(2\omega_2 t) + \cos[(\omega_1 + \omega_2)t] + \cos[(\omega_2 - \omega_1)t] \tag{13}$$

$$P^{(3)}(t) \propto \cos(3\omega_1 t) + \cos(3\omega_2 t) + \cos[(\omega_1 + 2\omega_2)t] + \cos[(2\omega_2 - \omega_1)t] + \cdots \tag{14}$$

These new frequencies include the effects of second and third harmonic generation, three wave mixing and four wave mixing. For a continuous spectrum, the resulting of mixing between infinitely dense tones will lead to supercontinuum generation.

2.2 Ultrafast Lasers

To produce and maintain modelocked oscillation necessary for the generation of ultrafast pulses, three conditions must be satisfied. First, both the laser medium and oscillator feedback elements must be of sufficient bandwidth to place all of the required cavity modes above the lasing threshold. Cavity dispersion must be eliminated or minimized across the operating bandwidth so that mode synchronization is possible. And finally, a means of synchronizing and maintaining synchronization between all cavity modes must be employed.

Several materials provide a gain bandwidth suitable for ultrafast modelocked operation, with the choice in particular material typically dictated by the required center wavelength. Early modelocked lasers employed aqueous solutions containing an organic dye, which could provide up to 40 nm of gain bandwidth [30]. Such organic die lasers have since been replaced with solid-state lasers, which have greater stability, endurance and ease of use. For solid-stae lasers, a large number of crystal possess gain spectra sufficiently broad for modelocked operation are available, including Alexandrite, Cr:LiSAF and Ti:Sapphire. For 800 nm operation, Ti:Sapphire crystal are the most frequently employed. These crystals have a 700-820 nm gain bandwidth and 380-630 nm pump band [30]. The gain media will typically introduce undesired dispersion into the laser cavity. To correct for this dispersion, prisms, gratings, or other dispersive elements with opposite dispersion properties are placed with the cavity in an attempt to obtain zero dispersion across the oscillator bandwidth.

Several methods are available to synchronize or modelock the cavity modes. The most common technique employed in ultrafast solid state oscillators is Kerr lens modelocking. In the presence of high instantaneous irradiance, nonlinear phase lag introduced along the optical axis of the confined modes within the gain medium will cause the mode to come to focus within the oscillator. Because increased irradiance is obtained for shorter pulses, this effect will be the greatest when all the cavity modes are synchronized and the oscillator pulses are the shortest. By placing an aperture stop of appropriate dimensions at the Kerr induced cavity focal point, cavity losses are introduced for non-modelocked operation, creating a bias for modelocked operation. If the aperture stop is implemented correctly, the cavity will naturally bring itself to and maintain modelocked operation.

The power and energy that can be extracted from an ultrafast oscillator is limited. For any application requiring significant pulse energy, ultrafast pulses must be subsequently amplified after extraction from the oscillator using additional laser amplifier stages. Like the oscillator gain medium, the laser amplifiers must also possess a gain bandwidth sufficient to amplify all of the modes which comprise the ultrafast pulse. Insufficient bandwidth will result in spectral narrowing of the ultrafast pulse and a corresponding increase in temporal pulse width. It is common for the same gain media to be employed in both the laser oscillator and amplifier, as it automatically ensures the amplifier will have sufficient bandwidth.

The high instantaneous power and irradiance that are readily obtained from ultrafast pulses present an additional problem to the amplifier stages of ultrafast lasers. As pulse energy increases, the high irradiance can both drive undesired nonlinear effects and cause damage to the amplifier optics and gain media. These effects can be avoided by reducing the instantaneous pulse power through chirped pulse amplification [31].

Chirped pulse amplification is a technique which employs dispersive elements to temporally chirp ultrafast pulses, extending their temporal duration by several orders of magnitude. By stretching the pulse, a corresponding reduction in instantaneous pulse power and irradiance is obtained. This delays the onset of high peak irradiances obtained from the pulse during amplification, which are sufficient to both drive unwanted nonlinearities and damage optical equipment, increasing the total gain which may be obtained before these effects set in by several orders of magnitude. Once the stretched pulse has been amplified, additional dispersive elements can be employed to counteract the beam chirp and recover a pulse possessing the initial temporal duration but at the newly obtained pulse energy.

A recently developed alternative to laser amplifiers are optical parametric amplifiers [32]. Optical parametric amplifiers use nonlinear mixing to transfer energy between the pump and signal fields in place of stimulated emission. The advantage to this approach is the medium being employed as an amplifier does not need to be excited, limiting thermal loading. This technique can be combined with chirped pulse amplification to reduce the peak irradiance applied to the amplifiers, the combination of techniques being referred to as optical parametric chirped pulsed amplification [33].

The Laser Plasma Laboratory (LPL) has developed or obtained several ultrafast laser systems used for the investigation of ultrafast, high-energy optical and electromagnetic physics. One of the first systems to be developed was the Terawatt (TW) laser. TW is a flashlamp pumped Cr:LiSAF based solid-state ultrafast laser using chirped-pulsed amplification, and is capable of generating 200 mJ pulses at 0.1 Hz. The MTFL is a modern, commercially obtained chirp-pulsed amplified Ti:Sapphire solid-state laser using diode pumps, and is capable of generating 20 mJ at 10 Hz. The laser system is currently being upgraded by LPL, and should be capable of generating pulses as high as 200 mJ when completed. LPL is currently developing a new laser system, designated HERACLES, which uses optical parametric amplification in combination with a carrier-envelope phase locked cavity to generated ultrafast, few-cycle pulses. When completed, this system should be suitable to carry out experiments in high-harmonic generation [34].

2.2 The MTFL Laser

Figure 1: The MTFL laser.

The majority experiments conducted using pulsed laser light used the MTFL laser, depicted in Figure 1 and Figure 2, as the pulse laser source. This includes all experiments conducted in both Chapters 3 and 4. MTFL is a Ti:Sapphire modelocked oscillator seeded, Ti:Sapphire amplified chirped pulsed amplified laser. The laser operates at a center wavelength of 790 nm, has a spectral bandwidth of 21 nm, and can produce pulses of 50 fs in the absence of spectral chirp. MFTL can generate pulses up to 2 mJ of energy at 1 kHz, and pulses up to 20 mJ of energy at 10 Hz.

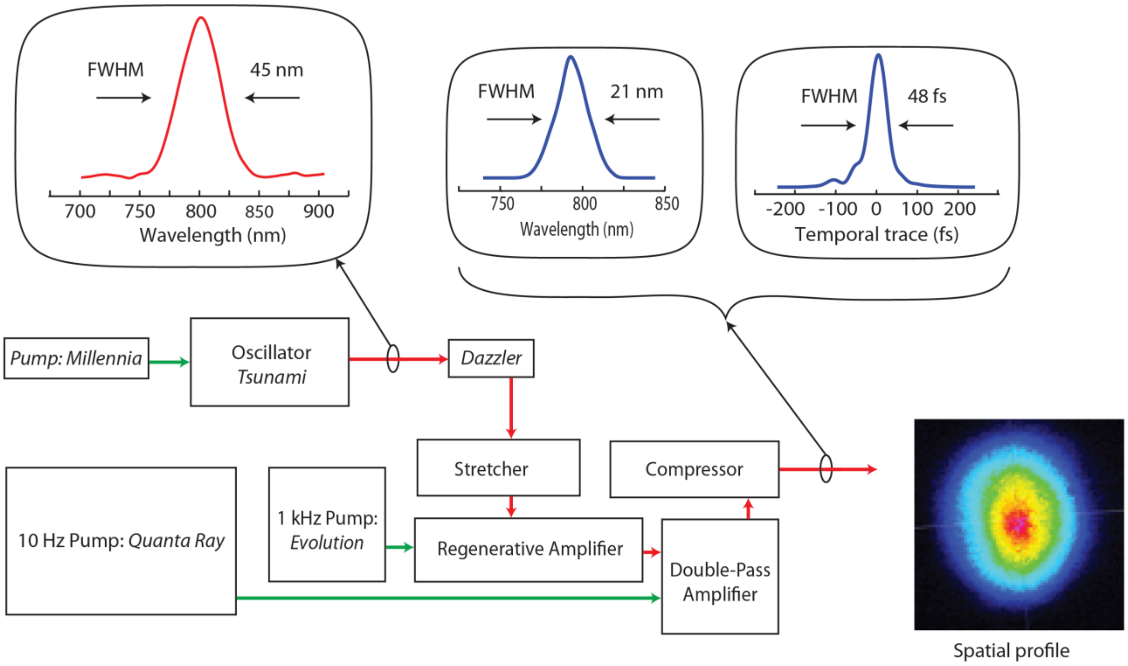

Figure 2: Technical layout of the MTFL laser.

2.2.1 Oscillator

MTFL employs a 800 nm, 50 fs, modelocked Ti:Sapphire oscillator (*Tsunami*, Spectra Physics). The oscillator produces a 75 MHz train of 6 nJ pulses, each approximately 45 nm in bandwidth. The Ti:Sapphire crystal was pumped using a 5 W, 532 nm diode-pumped frequency-doubled Nd:YVO4 laser (*Millennia*, Spectra Physics). An acousto-optic modulator was used to actively modelock the cavity.

2.2.2 Stretcher/Compressor

Both MFTL and TW employ chirped pulsed amplification to obtain high pulse energies. For the MTFL system, a Martinez grating stretcher is used to induce sufficient positive dispersion to stretch oscillator pulses to a temporal duration of 250 ps. After amplification, the pulse was compressed to 50 fs using negative dispersion obtain from a Tracey grating compressor [35].

2.2.3 Amplifiers

Two amplifiers in series were used to amplify the stretched oscillator pulses. Pulses were initially amplified over 13 passes within a Ti:sapphire regenerative amplifier, extracting 3 mJ of energy. The amplifier Ti:sapphire crystal was double end pumped using a pair of 10 W pulses obtained from a Q-switched, diode-pumped Nd:YLF laser (*Evolution 30*, Spectra Physics). Pulses extracted from the regenerative amplifier were either sent directly to the compressor, in the case of 1 kHz operation, or alternatively sent a second amplifier stage, in the case of 10 Hz operation.

A double pass Ti:sapphire amplifier was used as the second amplifier stage, from which pulse energies of 30 to 40 mJ were extracted. The laser was pumped using 360 mJ pulses obtained from a frequency doubled flash lamp pumped Nd:YAG laser (*Quanta Ray*, Spectra Physics). This served as the final amplifier stage in the MTFL system.

2.3 The Terawatt Laser

Experiments carried out in Chapter 4 used the Terawatt laser in addition to the MTFL laser. Terawatt is a Ti:Sapphire seeded, Cr:LiSAF amplified, chirped pulse amplified laser. Terawatt was designed and assembled by a group of LPL students including Steve Grantham, Paul Beaud, Edward Miesak, Bruce Chai, Kai Gabel, and Gregory Shimkaveg [36] [37]. Since its assembly and operation, it has been maintained and modified by Robert Bernath. Terawatt is capable of generating 200 fs, 50 nm bandwidth pulses at a center wavelength of 845 nm. The laser repetition rate varies from 1 kHz to 0.1 Hz depending on pulse energy. Pulse energies as high as 150 mJ can be achieved with this laser system.

2.3.1 Oscillator

Terawatt employs a Kerr-lens modelocked, Ti:Sapphire oscillator operating at 845 nm to generate a 2-5 nJ, 92 MHz pulse train. The oscillator is depicted in Figure 3. A Ti:Sapphire crystal is located within a cavity with a single 12.5% output coupler (OC). The Ti:Sapphire crystal is pumped using a 5 W Argon-Ion laser at 514 nm. A plano-convex lens with a 150 mm focal length is used to focus pump light onto the Ti:Sapphire crystal, at the location of the cavity minimum beam waist as dictated by the concave mirrors CM1 and CM2, to maximize mode volume. A prism pair (FS) is used for cavity dispersion compensation.

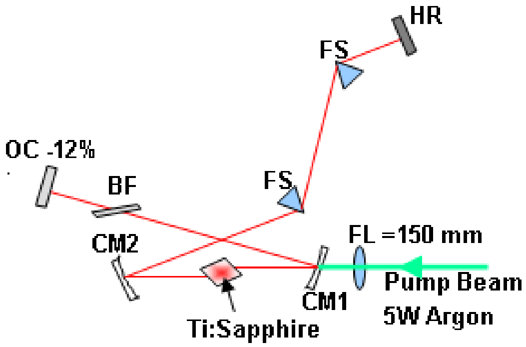

Figure 3: Layout of the terawatt oscillator.

Typically Ti:Sapphire oscillators operate at a center wavelength 800 nm. To shift the center wavelength to 845 nm for optimal use with Cr:LiSAF amplifiers, an adjustable slit was placed between the prism pair, and aligned to bias the cavity for operation for longer wavelength operation. The slit was also used to set the cavity bandwidth to 14 nm, again for optimal use with the Cr:LiSAF oscillators.

2.3.2 Stretcher/Compressor

To enable chirped-pulse amplifying operation, terawatt employs conventional grating stretchers and compressors. A folded Martinez-stretcher, depicted in Figure 4, is used to stretch the pulse obtained from the oscillator by inducing positive dispersion to chirp the pulse. Here, an 1800 lines/mm grating was placed 30 cm from a 58 cm focal length spherical lens. The chirp obtained from the stretcher was sufficient to increase the temporal pulse width by a factor of 3,000.

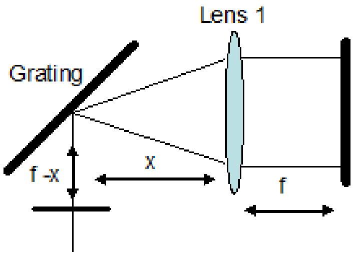

Figure 4: Terawatt pulse stretcher.

Pulse compression was accomplished using the Treacy compressor depicted in Figure 5. This compressor provides negative dispersion sufficient to retrieve a time-bandwidth limited pulse from the chirped pulse extracted from the amplifier stages of Terawatt. The Treacy compressor depicted was implemented using a pair of 1200 lines/mm gratings separated 20 cm apart.

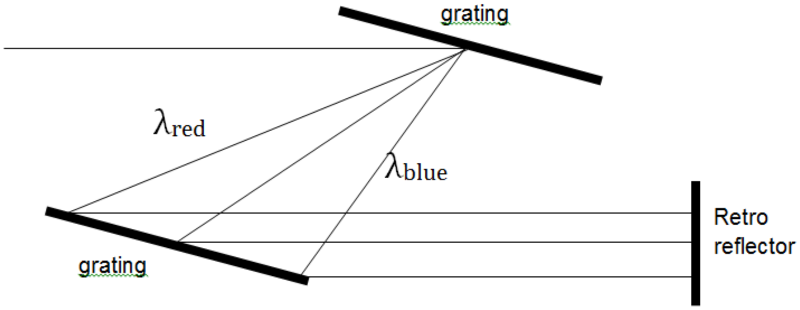

Figure 5: Terawatt pulse compressor.

2.3.3 Terawatt Amplifiers

Terawatt employs a series of amplifiers to increase pulse energy from 2-5 nJ to energies as great as 150 mJ. The first amplifier in series, depicted in Figure 6, is a regenerative amplifier, which employs a pair of Pockels cells (PC1 and PC 2) along with polarization optics to temporally trap incident light pulses within a second optical cavity. A flash lamp pumped Cr:LiSAF amplifier is located within the cavity, which amplifies pulses in the cavity during every pass, requiring 40 passes to extract the crystal gain after the flash lamp fires. Pulses are extracted using a 40% output coupler (OC) at the end of the cavity, resulting in an amplified pulse train at the output. A pulse slicer composed of a Pockels cell and two Glan-Taylor polarizers is used to extract a single amplified pulse from the pulse train extracted at the output. Pulse energies of approximately 4 mJ are extracted from this amplifier.

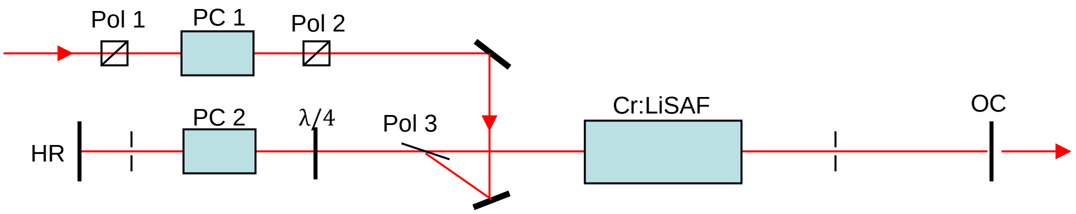

Figure 6: Terawatt regenerative amplifier layout.

A double-pass, Cr:LiSAF amplifier is used as the second stage amplifier. This amplifier employs a flash lamp pumped 7 x 105 mm Cr:LiSAF rod to obtain a double-pass gain of 12, increasing pulse energy to 50 mJ. To maintain good spatial beam quality, a spatial filter is placed in series with the amplifier. This setup is followed by a single pass Cr:LiSAF amplifier of the same dimensions, possessing a single-pass gain of 3, increasing pulse energy to 150 mJ.

2.4 Laser Range

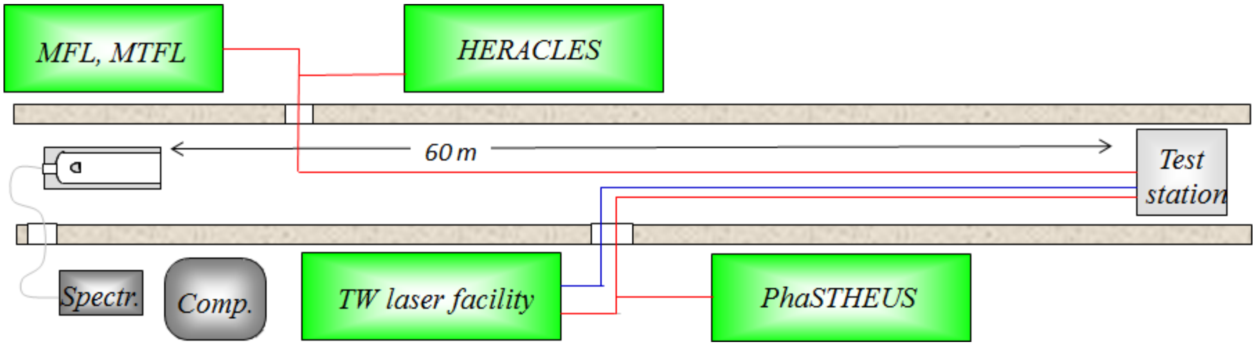

Figure 7: Layout of the various LPL lasers (including MFTL and TW), the laser range, and end station diagnostics.

Two laser ranges were available to carry out experiments. A 10 m range within the MTFL laser bay was used for short propagation distance experiments. When 10 m was insufficient for propagation experiments, or when the TW laser was employed, a 50 m range adjacent to the laser range was used. The 50 m range was accessed by both lasers through the use of turning mirrors. An end station located at the end of the 50 m range was used to mount optics and diagnostic equipment for long distance propagation experiments. The experiments involving RF and microwave measurements, the 50 m range also serves to distance the measurement equipment from the MTFL laser, preventing the RF measurements from recording RF radiation generated from the laser electronics, such as the Pockels cells.

Figure 8: End station located at the end of the 50 m end range.

2.5 Beam Imaging Systems

To evaluate beam geometry obtained from beam engineering experiments, the quantitative evaluation of laser beam transverse profiles was necessary. Such measurements can be carried out using conventional CCD cameras, provided the camera's operating characteristics are sufficiently well understood to obtain physical dimensions from the images. The principle difficulty in using cameras for beam profile measurements is that the high instantaneous irradiance of the ultrafast pulses employed during experiments is not only sufficient to saturate a CCD camera, but destroy the CCD sensor array. Thus a means to attenuate the transverse beam profile is required. Two optical configurations were employed to this end.

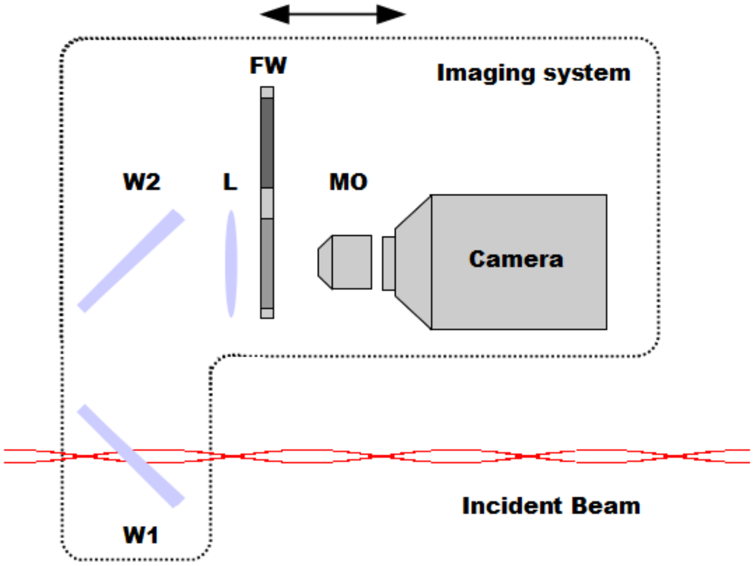

Figure 9: Initial transverse imaging setup.

The first of the two optical layouts is shown in Figure 9. Here the incident beam is reflected off of a pair of wedges (W1 and W2) oriented 45^o relative to the angle of incidence, before being transmitted through a filter wheel (FW) to the camera. The first wedge (W1) is mounted to a translation oriented perpendicular to the surface normal. The translation stage enables movement of the wedge surface between shots, preventing damage from a previous shot from degrading the imaging performance of the setup in subsequence shots. A lens (L) and microscope objective (MO) in series is used to image the surface of the first wedge to the camera, ensuring the transverse image recorded is that of the beam as it intersects the first wedge.

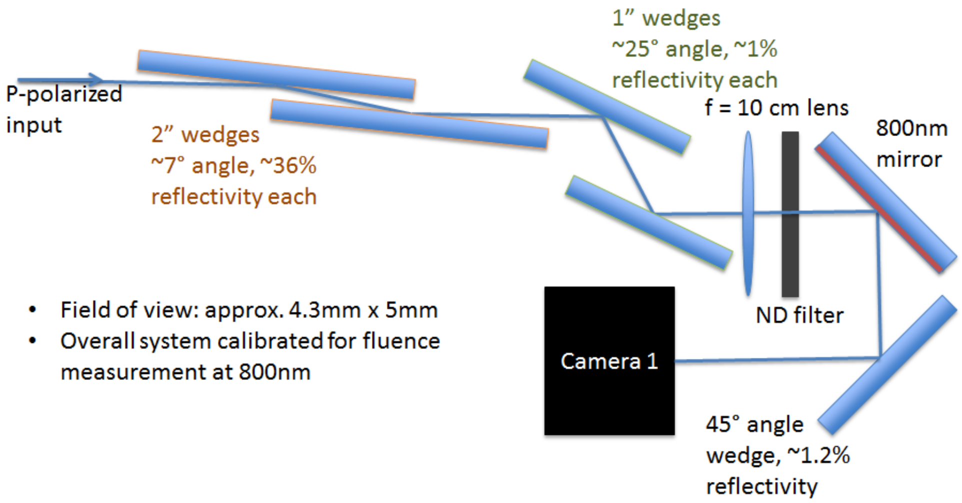

Figure 10: Modified transverse imaging setup.

To avoid the continual adjustments necessary when using the original imaging system to evaluate filaments, a second optical setup was devised by Khan Lim to image the transverse profiles of pulsed laser light. The modified optical configuration is shown in Figure 10. This setup employs a series of six wedges and a calibrated set of neutral density filters to attenuate incident light, and a single lens to image the surface of the first optical wedge onto the camera. The first two wedges use a grazing incidence of 7^o in place of the original 45^o angle. Because of the grazing incident angle, the peak irradiance of incident laser pulses, including those obtained during filamentation, was insufficient to damage the wedge due to the increase in projected area, omitting the need for a translation stage.

CHAPTER 3: NON-DIFFRACTING BEAMS, BESSEL BEAMS, AND HELICAL BEAMS

Diffraction is a feature that underlies all light propagation in nature [1] [38]. It imposes strict limits on optical systems, such as the minimum spot size that can be obtained with a lens, the maximum resolution that can be obtained with a microscope, and the minimum far field beam divergence that can be obtained with a laser. Ordinarily, these are fundamental physical limitations for which the physicist and the optical engineer must work around. However, a number of techniques are available to overcome such limitations.

One such technique is the use of diffraction-free or non-diffracting beams [3], which have been a topic of active research for more than 20 years [39]. Non-diffracting beams are exact solutions to the Helmholtz equation [8]. By virtue of their field shape, non-diffracting beams propagate unaltered through free space, maintaining the exact transverse field shape of the beam after propagating over an arbitrary distance [8], undergoing no changes beyond the addition of an arbitrary phase. Thus the shape and features of the beam remain unaltered during propagation. The Rayleigh range, which defines the spread of individual features found within the beam, is effectively infinite for this class of beams [39] [40] [4].

Non-diffracting beams possess a number of unique properties beyond features impervious to diffraction. Non-diffracting beams are capable of reconstructing their geometry after propagating through solid obstructions, enabling regeneration of the beam during propagation [41] [40] [42]. In special cases, motion of beam transverse features can be obtained during propagation. This includes accelerating, lateral translation that has been observed in the case of Airy beams [5] [43], and rotational and spiraling motion that has been observed for Bessel beams [44] [45] [46] [47] [48] [49].

Ideal non-diffracting beams have both infinite energy and infinite spatial extension, making them unrealizable in a laboratory setting. However, there exist finite energy, spatially confined approximations of non-diffracting beams which can be produced in a lab [50]. Such approximately non-diffracting beams can propagate a finite distance through space unaltered before diffraction effects set it.

3.1 Diffraction Theory

Light has been understood as the propagation of electromagnetic waves since Maxwell compiled a complete set of equations describing electrodynamics. Like all waves, its propagation physics are dictated by diffraction. Diffraction physics therefore dictate the limits and capabilities of light propagation.

Light diffraction is dictated by the Helmholtz equation. In the absence of free charge or currents, Maxwell's equations are reduced to [51]

$$\nabla \cdot \vec{E} = 0 \tag{15}$$

$$\nabla \cdot \vec{B} = 0 \tag{16}$$

$$\nabla \times \vec{E} = \frac{\partial \vec{B}}{\partial t} \tag{17}$$

$$\nabla \times \vec{B} = \frac{n^2}{c^2}\frac{\partial \vec{E}}{\partial t} \tag{18}$$

If polarization effects are neglected, such as by assuming the electromagnetic wave is of uniform polarization, an assumption consistent with most laser light sources, the Helmholtz equation can be obtained as a simultaneous solution to the above set of equations. The Helmholtz equation is given as

$$\nabla^2 E - \frac{n^2}{c^2}\frac{\partial^2 E}{\partial t^2} = 0 \tag{19}$$

The Helmholtz equation dictates all scalar diffraction effects within a linear media in the absence of free charge or current. Diffraction can be alternatively described using the Rayleigh-Sommerfeld diffraction integral [1]

$$E(x_2, y_2, z) = \frac{z}{i\lambda}\iint_{-\infty}^{\infty} E(x_1, y_1, 0)\frac{e^{ikl}}{l^2}dx_1 dy_1 \tag{20}$$

$$l = \sqrt{(x_2 - x_1)^2 + (y_2 - y_1)^2 + z^2} \tag{21}$$

which can be approximated using the Fresnel diffraction integral

$$E(x_2, y_2, z) = \frac{e^{ikz}}{i\lambda z}\iint_{-\infty}^{\infty} E(x_1, y_1, 0)\exp\left[\frac{ik}{2z}((x_2 - x_1)^2 + (y_2 - y_1)^2)\right]dx_1 dy_1 \tag{22}$$

for values of z for which

$$z^3 \gg \frac{\pi}{4\lambda}\left[(x_2 - x_1)^2 + (y_2 - y_1)^2\right]_{max}^2 \tag{23}$$

The integral formulation of diffraction provided in equations 20 and 22 have proven sufficient to describe the evolution of Bessel beams and their superpositions from both spatial filters and axicons, as will be discussed.

3.2 Consequences of Diffraction

Diffraction places inherent limits on optical imaging and beam propagation. In the case of beam propagation, beam confinement and the range over which a beam is confined during propagation is limited by diffraction and the Rayleigh range [30]. For a Gaussian beam, which provides an accurate representation for the beam shape found in most lasers and optical systems, the Rayleigh range scales as the square of the minimum beam spot size. Specifically, for a Gaussian beam described by

$$E(r,z) = E_0(z)\exp\left(-\frac{r^2}{w^2(z)}\right)\exp[i\psi(r,z)] \tag{24}$$

the beamwaist $w(z)$ will diverge at a rate described by [30]

$$w(z) = w_0\sqrt{1+\left(\frac{z}{z_R}\right)^2} \tag{25}$$

where w_0 is the minimum beam waist which is typically used to defined the radius of the minimum beam spot size and z_R is the Rayleigh range defined by

$$z_R \equiv \frac{n\pi w_0^2}{\lambda} \tag{26}$$

which can be observed to scale are the square of the minimum beam waist. As the beam expands the electric field strength is reduced by

$$E_0(r) = \frac{z_R}{\sqrt{z^2+z_R^2}}E_0 \tag{27}$$

The beam wavefront curvature is given by $\psi(r,z)$ which is described by

$$\psi(r,z) = \frac{r^2}{R^2(z)} + \arctan\frac{z}{z_R} \tag{28}$$

where $R(z)$ is the beam radius of curvature described by

$$R(z) = z\left[1 + \left(\frac{\pi w_0^2}{\lambda z}\right)^2\right] \tag{29}$$

From equations 25 and 26 it is apparent the beam will only remained confined to the minimum beam waist for a distance proportional to the square of that beam waist, and that the far-field beam divergence will be inversely proportional to the minimum beam waist. This introduces a problematic tradeoff: the smaller the beam spot required, the shorter the distance the beam can propagate while being confined to the required radius. It is a problem that can be rectified using non-diffracting beams.

3.3 Bessel Beams

Perhaps the most extensively investigated non-diffracting beam geometry is the Bessel beam [50]. Bessel beams are a family of beams which comprise a complete set of exact solutions to the Helmholtz equation when expanded in cylindrical-polar coordinates [39] [8]. The transverse profile which describes the electric field strength of the Bessel beam perpendicular to the direction of propagation is described by a Bessel function, giving this class of beams their name. In addition to satisfying the Helmholtz equation, Bessel beams form a complete orthonormal basis for scalar waveforms in three dimensional space [52]. Axial symmetric beams are described entirely by order zero Bessel beams within this basis. Conversely, any azimuthal asymmetry present in a scalar waveform requires Bessel beams of order other than zero to describe when expanded in this particular basis.

As per all non-diffracting beams, ideal Bessel beams contain both infinite energy and require an infinite beam aperture [53]. In practice, truncated approximations of Bessel beams must be employed to carry out experiments. Typically, Bessel-Gauss beams are employed as approximations of the ideal case [50]. Bessel-Gauss beams are an aperture limited version of the ideal case, limited in both diameter and propagation distance by a Gaussian envelope.

Bessel-Gauss beams can be obtained in the laboratory through the use of an axicon [54] [55], spatial filtering [56], specially designed holographic plates [57] [58], or a system of diffractive optical elements [59]. The aforementioned techniques will typically yield order zero Bessel beams. Higher order Bessel beams can be obtained by using these techniques in conjunction with either azimuthal phase elements that introduce integer topological charge [60] [61], or a Laguerre-Gauss beam [62] [63].

Bessel beam generation can be described using diffraction theory [39]. To evaluate Bessel beam diffraction, cylindrical-polar coordinates are used. The Fresnel diffraction integral in cylindrical coordinates is given by

$$\begin{gathered}
E_2(r_2,\phi_2) = \frac{\exp(ikz)}{i\lambda z}\exp\left[i\frac{kr_2^2}{2z}\right] \\
\cdot\int_0^\infty dr_1\int_0^{2\pi} d\phi_1\left[r_1E_1(r_1,\phi_1)\exp\left(i\frac{kr_1^2}{2z}\right)\exp\left(-i\frac{kr_1r_2}{z}\cos(\phi_2-\phi_1)\right)\right]
\end{gathered} \tag{30}$$

Expanding the electric field as a Fourier series in ϕ,

$$E(r,\phi) = \sum_{m=-\infty}^{\infty} E_m(r)\exp(im\phi) \tag{31}$$

employing the Jacobi-Anger expansion,

$$\exp\left[-\frac{k_0 r_1 r_2}{z}\cos(\phi_2-\phi_1)\right] = \sum_{m=-\infty}^{\infty}(-i)^m J_m\left(\frac{kr_1r_2}{z}\right)\exp(-im\phi_1)\exp(im\phi_2) \tag{32}$$

observing the orthogonally relationship,

$$\begin{aligned}\int_0^{2\pi} d\phi_1 \sum_{l=-\infty}^{\infty}\sum_{m=-\infty}^{\infty}(-i)^l E_m(r)\,\mathrm{J}_l\left(\frac{kr_1r_2}{z}\right)\exp(im\phi_1)\exp(-il\phi_1)\exp(im\phi_2)\\ = 2\pi\sum_{m=-\infty}^{\infty}(-i)^m E_m(r_1)J_m\left(\frac{kr_1r_2}{z}\right)\exp(im\phi_2)\end{aligned} \tag{33}$$

and substituting the results into the Fresnel diffraction integral yields

$$\begin{aligned}E_2(r_2,\phi_2) = \frac{kexp(ikz)}{iz}\exp\left[i\frac{kr_2^2}{2z}\right]\cdot\\ \sum_{m=-\infty}^{\infty}(-i)^m\exp(im\phi_2)\int_0^{\infty}dr_1\, r_1E_{1m}(r_1)J_m\left(\frac{kr_1r_2}{z}\right)\exp\left(i\frac{kr_1^2}{2z}\right)\\ = \sum_{m=-\infty}^{\infty}(-i)^m\exp(im\phi_2)\,E_{2m}(r_2)\end{aligned} \tag{34}$$

Equation 34 is the Fresnel diffraction integral represented using a modified Hankel transform

$$E_{2m}(r_2) = \frac{kexp(ikz)}{iz}\exp\left[i\frac{kr_2^2}{2z}\right]\int_0^{\infty}dr_1\, r_1E_{1m}(r_1)J_m\left(\frac{kr_1r_2}{z}\right)\exp\left(i\frac{kr_1^2}{2z}\right) \tag{35}$$

Equations in 34 and 35 can be used in place of the Fresnel diffraction integral when working in cylindrical-polar coordinates.

While there are numerous means to truncate a Bessel beam, only Bessel-Gauss beams will be considered using the above equations. Of the numerous methods for generating Bessel beams, only two methods where investigated experimentally, both of which can be described explicitly through the use of diffraction theory. Ideal Bessel beams can be taken as a special case of Bessel-Gauss beams for which the Gaussian beam waist $w \rightarrow \infty$, for which the subsequent analysis is also valid.

3.4 Generating Bessel Beams through Spatial Filtering

Spatial filtering is a means to construct an arbitrary beam shape through the application of the spatial Fourier transform. When undergoing diffraction, the Fourier transform of a transverse wavefront will be obtained in the Fraunhofer limit, normally expressed as

$$z \gg \frac{D^2}{\lambda} \tag{36}$$

where D is the beam diameter. Thus under normal circumstances, a spatial Fourier transform of the wavefront can only be obtained at large propagation distances. However, if a wavefront is incident on a spherical lens, its spatial Fourier transform will instead be found at the lens focal plane.

Beam synthesis through the application of spatial filtering is obtained by first determining the spatial Fourier transform of the desired beam. A mask is then used to selectively block any components not part of the desired spatial Fourier transform in the beam. The remaining filtered beam is transmitted through a lens, after which the desired beam shape will be found at the lens focal plane.

This method benefits from simple experimental implementation as spherical lenses are readily available and the mask required to shape the beam can be quickly fabricated using a mill and sheets of basic materials, such as plastics and metals. However, this method makes inefficient use of incident light, as any light not present in the desired spatial frequencies is lost.

Bessel beams can be represented as an infinite collection of plane waves, all of which whose normals make the same angle relative to the optical axis [3]. Each plane is of different azimuthal orientation, and collectively the plane waves are distributed evenly around the optical axis. The spatial Fourier transform corresponding to such a configuration is a uniform irradiance, infinitely thin ring. An implementation of this Fourier transform can then be obtained by placing and aligning a ring slit in the path of a collimated beam, followed by a spherical lens in series, for which a Bessel beam is obtained.

Mathematically, synthesis of a Bessel beam through the use of spatial filtering can be described through the application of the previously derived diffraction integrals. Starting with a Gaussian beam with an azimuthal charge of m

$$E(r) = E_0 \exp\left(-\frac{r^2}{w^2}\right) \exp(im\phi) \qquad \textbf{(37)}$$

The Gaussian beam is filtered using a ring mask, which is a thin annular aperture of radius r_0 and radial width Δr. The electric field immediately after the mask will be

$$E(r,\phi) = E_0 \Delta r \exp\left(-\frac{r_0^2}{w^2}\right) \delta(r - r_0) \exp(im\phi) \tag{38}$$

If this field is then transmitted through a lens of focal length f immediately after the annular mask, the resulting field will be

$$E(r,\phi) = E_0 \Delta r \exp\left(-\frac{r_0^2}{w^2}\right) \delta(r - r_0) \exp\left(-i\frac{kr^2}{2f}\right) \exp(im\phi) \tag{39}$$

Substituting this expression into the Fresnel diffraction integral

$$\begin{aligned} E_2(r_2,\phi_2) &= (-i)^m E_{2,m}(r_2) \exp(im\phi_2) \\ &= (-i)^m E_0 \Delta r \exp\left(-\frac{r^2}{w^2}\right) \frac{kexp(ikz)}{iz} \exp\left[i\frac{kr_2^2}{2z}\right] \exp(im\phi_2) \\ &\quad \cdot \int_0^\infty dr_1\, r_1 J_m\left(\frac{kr_1 r_2}{z}\right) \delta(r - r_0) \exp\left[i\frac{kr_1^2}{2}\left(\frac{1}{z} - \frac{1}{f}\right)\right] \\ &= (-i)^m E_0 \Delta r \exp\left(-\frac{r_0^2}{w^2}\right) J_m\left(\frac{kr_0}{z} r_2\right) \frac{kr_0 \exp(ikz)}{z} \exp\left[i\frac{kr_2^2}{2z}\right] \exp(im\phi) \end{aligned} \tag{40}$$

At the focal plane of the lens, where $z = f$

$$E(r) = (-i)^m E_0 \Delta r \frac{kr_0}{f} \exp\left(-\frac{r_0^2}{w^2}\right) J_m\left(\frac{kr_0}{f} r\right) \exp\left[ik\left(f - \frac{r^2}{2f}\right)\right] \exp(im\phi) \tag{41}$$

The irradiance corresponding to this electric field distribution is

$$I(r) = I_0 \left(\frac{kr_0}{f} \Delta\mathrm{r}\right)^2 \exp\left(-\frac{r_0^2}{w^2}\right) J_m^2\left(\frac{kr_0}{f} r\right) \tag{42}$$

Equation 42 describes an order *m* Bessel beam which is present in the immediate vicinity of the lens focal length. Because the spatial Fourier transform is only present near the lens focal plane, the spatial extent of Bessel beams generated in this manner is limited. This limitation corresponds in part to the limited energy that is typically extracted from the spatial filtering technique.

3.5 Bessel Beam Generation Using an Axicon Lens

Axicons provide a means for generating Bessel beams that is both simple and makes efficient use of incident radiation power. Axicons are conical lenses. Like conventional lenses, axicons introduce a radially dependent phase lag across an incident wavefront. Due to axicon geometry, the phase lag varies linearly with radial distance, while a conventional lens induces a quadratic phase lag across the wavefront of an incident wave.

By transmitting a Gaussian beam through an axicon, Bessel-Gauss beams are readily obtained [55] [62]. As in the case of spatial filtering, the fixed refraction angle of the axicon generates a family of azimuthally symmetric plane waves possessing normals making identical angles with respect to the optical axis. Axicons are defined by a conical apex angle, which determines the slope of the axicon conical geometry and dictates scale and propagation of the Bessel beams resulting from axicon synthesis.

Axicon synthesis can be described analytically by applying the stationary phase approximation to the Fresenel diffraction integral [39]. To describe the effects of an axicon on an incident wavefront, the thin lens approximation is used. In the thin lens approximation, the refracted wavefront of immediately after an axicon is described as

$$E_{refracted}(r,\phi) = E_{incident}(r,\phi) \cdot \exp(-ik\beta r) \tag{43}$$

where β is the refraction angle associated with the axicon. The refraction angle is related to the axicon conical apex angle α_p by

$$\beta = (n-1)\frac{(\pi - \alpha_p)}{2} \tag{44}$$

where n is the refractive index of the axicon glass. Starting with a Gaussian beam having peak irradiance I_0 an associated peak electric field strength, $E_0 = \sqrt{\frac{2}{c\epsilon_0} I_0}$, and an azimuthal charge of m (obtainable through the application of a vortex phase plate)

$$E_{incident} = E_0 \exp\left(-\frac{r^2}{w^2}\right) \exp(im\phi) \tag{45}$$

and applying the axicon wavefront phase lag yields

$$E_1 = E_0 \exp\left(-\frac{r^2}{w^2}\right) \exp(-ik\beta r) \exp(im\phi) \tag{46}$$

Substituting this result into the Fresnel diffraction integral gives

$$\begin{aligned} E_2(r_2,\phi_2) &= (-i)^m E_{2,m}(r_2) \exp(im\phi_2) \\ &= (-i)^m E_0 \frac{k \exp(ikz)}{iz} \exp\left[i\frac{kr_2^2}{2z}\right] \exp(im\phi_2) \\ &\cdot \int_0^\infty dr_1 r_1 J_m\left(\frac{kr_1r_2}{z}\right) \exp\left(-\frac{r_1^2}{w^2}\right) \exp\left(i\frac{kr_1^2}{2z}\right) \exp(-ik\beta r_1) \end{aligned} \tag{47}$$

To solve Equation 47, the stationary phase method is used (see Appendix D). Applying the method of stationary phase

$$\psi = \frac{kr_1^2}{2z} - k\beta r_1 \tag{48}$$

$$\frac{\partial\psi}{\partial r_1} = \frac{kr_1}{z} - k\beta = 0 \tag{49}$$

$$\frac{\partial^2\psi}{\partial r_1^2} = \frac{k}{z} \tag{50}$$

$$r_1 = \beta z \tag{51}$$

and substituting the results yields

$$\begin{aligned} E_2(r_2,\phi_2) = (-i)^m E_0\beta k\, \mathrm{J}_m(\beta k r_2)\exp\left(-\frac{\beta^2 z^2}{w^2}\right)\exp(ikz)\exp\left[i\frac{\beta^2 kz}{2}\right]\exp\left[i\frac{kr_2^2}{2z}\right] \\ \cdot\int_0^\infty dr_1 \exp\left[i\frac{k}{2z}(r_1-\beta z)^2\right] \end{aligned} \tag{52}$$

Solving the integral associated with the second order phase term gives

$$\begin{aligned} \int_0^\infty dr_1 \exp\left[i\frac{k}{2z}(r_1-\beta z)^2\right] = \int_{-\beta z}^\infty du \exp\left[i\frac{k}{2z}u^2\right] \\ = \sqrt{\frac{\pi z}{2k}}\exp\left(-i\frac{\pi}{4}\right)\left[1+\mathrm{erf}\left(\sqrt{i\frac{\beta^2 kz}{2}}\right)\right] \end{aligned} \tag{53}$$

Defining the quantities

$$k_\perp = \beta k \tag{54}$$

$$l_{nd} = \frac{w}{\beta} \tag{55}$$

$$G(z) = \left[1 + \mathrm{erf}\left(\sqrt{i\frac{k_\perp^2 z}{2k}}\right)\right] \tag{56}$$

the diffracted field can then be reduced to

$$E_2(r_2) = e^{-i\frac{(3+2m)\pi}{4}}$$
$$\cdot E_0 J_m(k_\perp r_2)\sqrt{\pi\frac{k_\perp^2 z}{2k}}\exp\left(-\frac{z^2}{l_{nd}^2}\right)\exp\left(i\frac{kr_2^2}{2z}\right)\exp\left[i\left(k - \frac{k_\perp^2}{2k}\right)z\right]\exp(im\phi)\,G(z) \tag{57}$$

Here the quantities $k_\perp$ and l_{nd} have definite physical meaning. The quantity l_{nd} is the non-diffracting length of the Bessel-Gauss beam. It represents the finite propagation distance of the Bessel-Gauss beam as a consequence of its finite spatial extent, as illustrated in Figure 11. A Bessel beam of infinite spatial extent can be obtained by taking $w \to \infty$ for which $l_{nd} \to \infty$. In this case the Bessel beam propagates indefinitely as expected.

The quantity $k_\perp$ is the component of the wavevector normal to the direction of propagation, which can also be obtained through the dispersion relationship derived from the Helmholtz equation. The dispersion relation obtained here and that obtained from the Helmholtz equation are equivalent for $k_\perp \ll k$ or $\beta \ll 1$. Because for all experiments carried out the refraction angle was limited to $\beta < 0.005$, this condition is always satisfied. Under this condition the dispersion relation

$$k^2 = k_z^2 + k_\perp^2 \tag{58}$$

can be shown to reduce to

$$k_z = k\sqrt{1 - \frac{k_\perp^2}{k^2}} \approx k - \frac{k_\perp^2}{2k} \quad \textbf{(59)}$$

which is the longitudinal wavenumber given in Equation 57. The irradiance of the Bessel beam can then be obtained from the electric field

$$I(r) = \frac{1}{2} c\epsilon_0 E^* E \quad \textbf{(60)}$$

$$I(r) = I_0 \pi^2 J_m^2(k_\perp r)\frac{k_\perp^2 z}{2k}\exp\left(-\frac{2z^2}{l_{nd}^2}\right)|G(z)|^2 \quad \textbf{(61)}$$

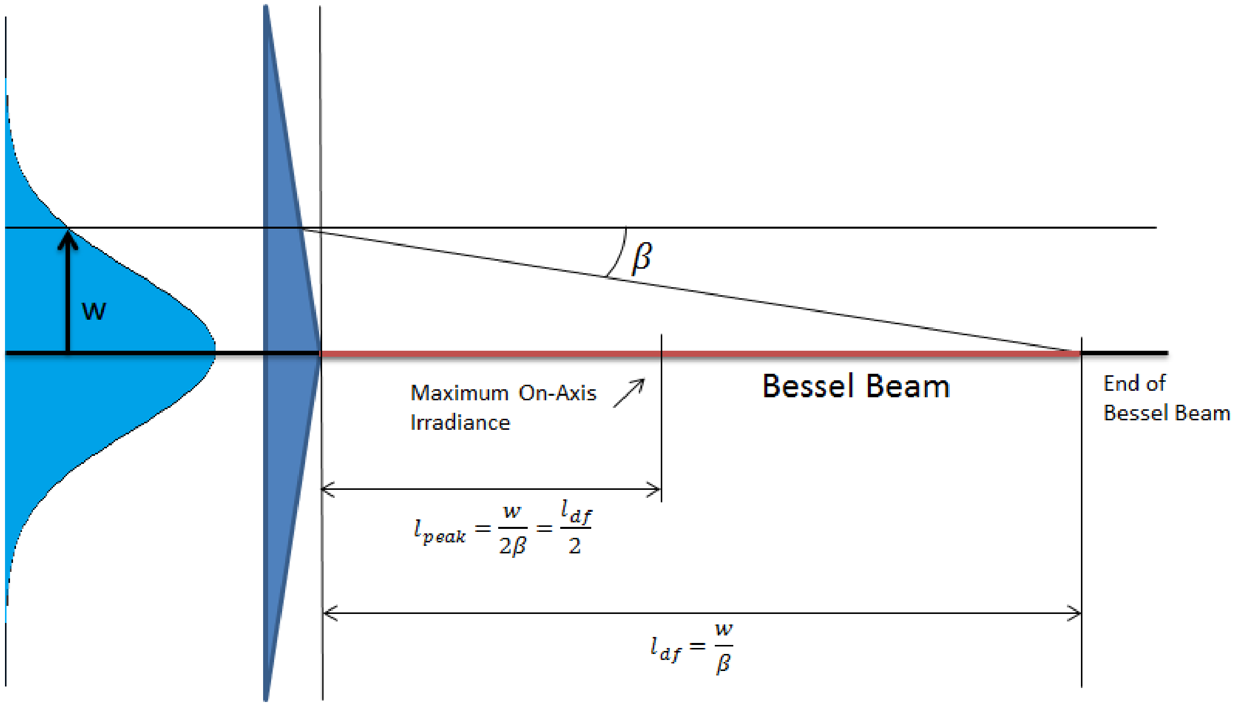

Figure 11: Geometric illustration of the diffraction-free length of a Bessel beam generated from an axicon illuminated with a Gaussian beam.

From Equation 61, an axicon generated Bessel beam is expected to propagate from $z = 0$ to $z = l_{nd}$, with a maximum on axis irradiance at $z = \frac{l_{nd}}{2}$ as shown in Figure 11. On axis, irradiances on the order of $I \cong \frac{\beta^2 \pi^3}{\lambda} I_0$ are obtained, well in excess of the Gaussian beam peak irradiance I_0. The falloff of beam irradiance with distance described by the exponential of the Bessel beam is a consequence of the limited aperture of the beam as previously described.

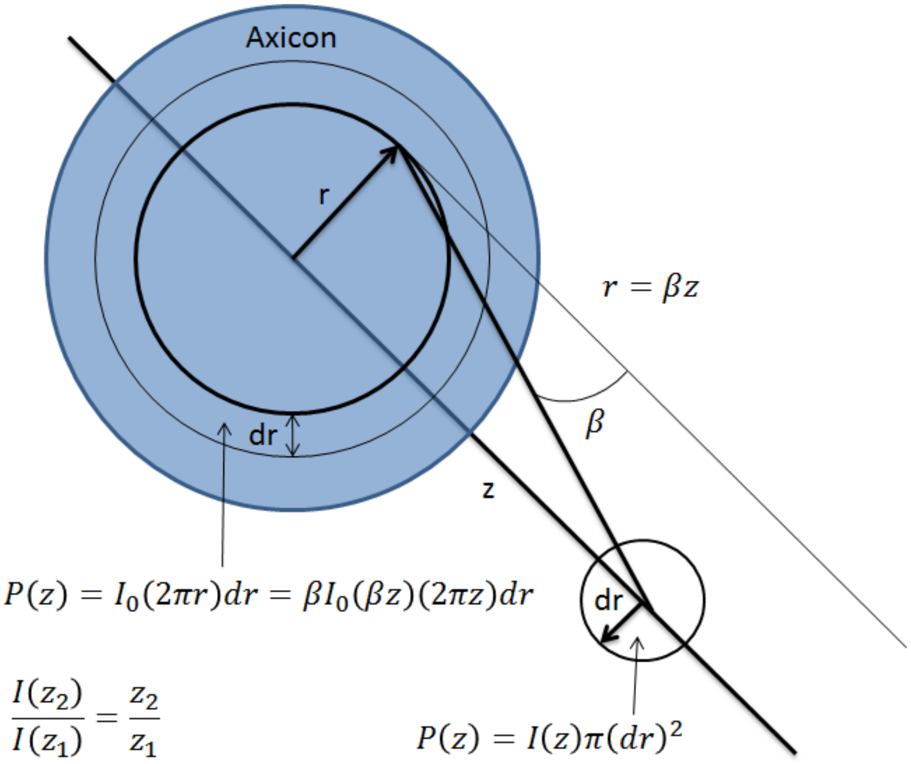

Figure 12: Geometric representation of the linear scaling of on-axis Bessel beam irradiance with propagation distance.

The linear increase of beam irradiance with distance observed in Equation 61 is an artifact of axicon generation. The fixed refraction angle of an axicon results in a direct linear mapping of radial displacement along the axicon to longitudinal displacement along the propagation axis. Irradiance along the beam axis corresponds to irradiance integrated over the circumference of the axicon at a fixed radius, as shown in Figure 12. For increasing propagation distance, the radius of this circumference will increase, corresponding to an increase in integrated power if the irradiance incident on the axicon is uniform.

Because of the extended propagation distance and high conversion efficiencies, axicon generation is ideal when extended, high irradiance Bessel beams are desired. Such benefits will prove suitable for the generation of Bessel filaments, to be discussed in Chapter 4.

3.6 Helical Beams

Beam geometries of greater complexity can be obtained through the superposition of multiple Bessel beams [60] [64] [65] [66] [67]. Such beam superposition exhibit transverse irradiance profiles that are periodic with propagation distance [68], rather than invariant with beam propagation as in the case of a single Bessel beam. Such beam superposition techniques have enabled the synthesis of a variety of beam structures, which can be observed to rotate either as a function of propagation distance [56] [68] [49] [45] [46], or as a function of optical system parameters [48] [69] [70]. Rotating beam geometries have a wide variety of applications, including optical micromanipulation [66] [67] [70] [71] [72] [73], vortex motion in Bose-Einstein condensates [69], high resolution imaging [74] [75] [76], complex optofluidity [77], and propeller solitons [78] [79] [80].

Helical beams are a class of non-diffracting beams characterized by a pair of diffraction impervious irradiance peaks arranged in diametrically opposite locations across the propagation axis, which rotate about the propagation axis during beam propagation. Helical beams are obtained through the superposition of two order one Bessel beams of opposite azimuthal charge, as previously illustrated mathematically by Bekshaev et al. [44]. While the features of individual non-diffracting beams remained unaltered with the exception of a phase term during propagation, the resulting superposition of the two beams will not maintain its transverse shape due to the mutual interference between the individual Bessel beams. However, such transverse structure will vary periodically while propagating through space [68]. In the case of helical beams, such periodic variations in the beam profile correspond to the rotation of the helical beam about the optical axis.

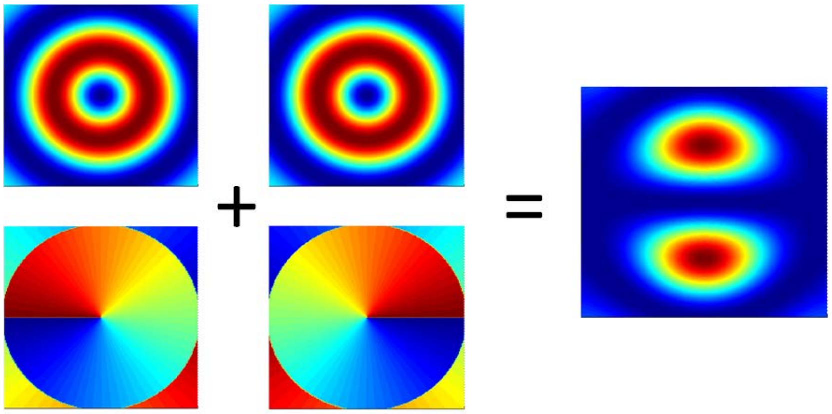

$E = J_1(r)e^{im\phi}$ $E = J_{-1}(r)e^{-im\phi}$

Figure 13: The transverse irradiance (top) and phase (bottom) profiles of order ± 1 *Bessel beams and their resulting superposition (right).*

To illustrate the construction of a helical beam from a Bessel beam basis, consider two arbitrary order one Bessel beams of opposite azimuthal charge and equal on axis field strength as depicted in Figure 13.

$$E_1(r, \phi, z) = J_1(k_{\perp_1} r) \exp(i\phi) \exp\left[i\left(k - \frac{k_{\perp_1}^2}{2k}\right)z\right] \qquad \textbf{(62)}$$

$$E_{-1}(r,\phi,z) = J_1\left(k_{\perp_{-1}}r\right)\exp(-i\phi)\exp\left[i\left(k - \frac{k_{\perp_{-1}}^2}{2k}\right)z\right] \tag{63}$$

where the approximation in Equation 59 was used to satisfy the dispersion relation. If the perpendicular wavenumbers are sufficiently close that the approximation $J_1\left(k_{\perp_1}r\right) \cong J_1\left(k_{\perp_2}r\right)$ is valid, than the superposition of the two Bessel beams is

$$\begin{aligned} E(r,\phi,z) &= E_1(r,\phi,z) + E_{-1}(r,z) \\ &\cong J_1\left(k_{\perp_1}z\right)\exp(ikz)\left\{\exp\left[i\left(\phi - \frac{k_{\perp_1}^2}{2k}z\right)\right] + \exp\left[-i\left(\phi + \frac{k_{\perp_{-1}}^2}{2k}z\right)\right]\right\} \\ &= 2J_1\left(k_{\perp_1}z\right)\cos\left(\phi - \frac{k_{\perp_1}^2 - k_{\perp_{-1}}^2}{4k}z\right)\exp\left[i\left(k - \frac{k_{\perp_1}^2 + k_{\perp_{-1}}^2}{2k}z\right)\right] \end{aligned} \tag{64}$$

The spatial irradiance corresponding to this field shape is

$$I(r,\phi,z) \propto J_1^2\left(k_{\perp_1}z\right)\cos^2\left(\phi - \frac{k_{\perp_1}^2 - k_{\perp_{-1}}^2}{4k}z\right) \tag{65}$$

The cosine term in Equation 65 indicates the beam irradiance rotates at the rate of defined by

$$\frac{d\theta}{dz} = \frac{k_{\perp_1}^2 - k_{\perp_{-1}}^2}{4k} \tag{66}$$

From the above equations it can be concluded that under the appropriate conditions, helical beams can be obtained as a superposition of two order one Bessel beams.

3.7 Coaxial Helical Beam Synthesis

While Helical beams synthesis is conceptually simple as it only requires a sum of two discrete components in a natural basis of the Helmholtz equation, achieving helical beams experimentally requires precise alignment in space, and for the case of pulsed light, precise alignment in time. Helical beam synthesis therefore requires an approach that can readily deal with the alignment problems presented in obtaining the correct Bessel beam superposition.

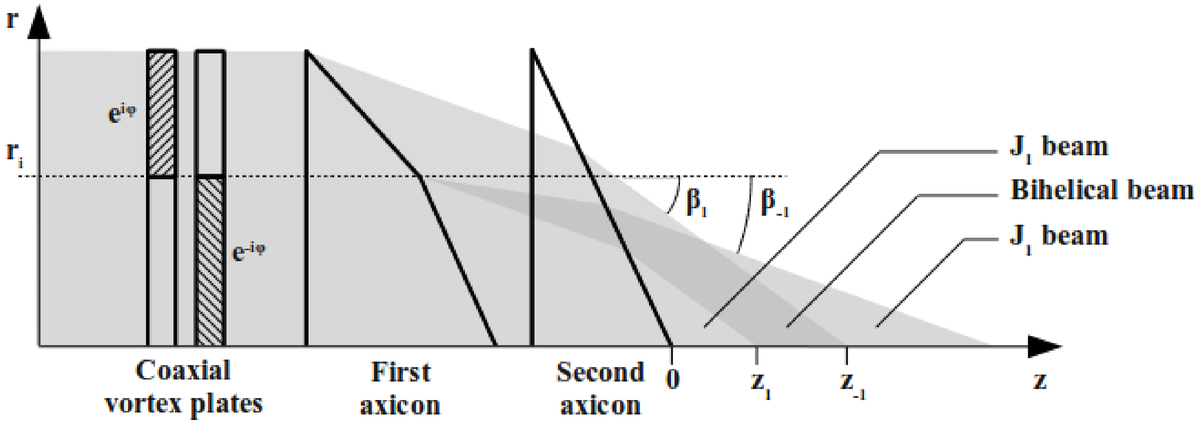

Figure 14: Conceptual layout of an optical configuration used for helical beam synthesis.

To overcome the alignment problems present in obtaining an aligned Bessel beam superposition, a coaxial beam synthesis approach was adopted. Coaxial helical beam synthesis is carried out by applying the phase necessary to generate two oppositely charge Bessel beams to radially disparate sections of the same incident beam. In this approach, a unit azimuthal charge and fixed refraction angle is applied to the beam within a radius r_S, while the opposite azimuthal charge and a different refraction angle will be applied the remainder of the beam outside of this radius. A conceptual diagram of a coaxial helical beam setup is illustrated in Figure 14.

To ensure both beams overlap along the optical axis, a greater diffraction angle must be applied to the outermost beam, ensuring faster convergence of the outer beam towards the optical axis. Mathematically, this optical configuration depicted in Figure 14 is represented by

$$E_{inner} = \exp(-i\phi)\exp(-ik\beta_i r)\,E_{incident} \tag{67}$$

for $r < r_s$, and by

$$E_{outer} = \exp(i\phi)\exp(-ik\beta_o r)\,E_{incident} \tag{68}$$

for $r > r_s$, where $E_{incident}$ is the incident Gaussian beam, r_s is the separation radius between the inner and outer section of the coaxial optics, and β_i and β_o are the cumulative refraction angles associated with the inner and outer radial regions of the optics.

As in the previous cases, this optical configuration can be evaluated using the Fresnel diffraction integral. Expressing the beam immediately after the refractive elements as

$$E_1(r,\phi) = E_0 \exp\left(-\frac{r^2}{w^2}\right)[u(r-r_s)\exp(ik\beta_o r)\exp(i\phi) + u(r_s - r)\exp(-ik\beta_i r)\exp(-i\phi)] \tag{69}$$

where $u(r)$ is the step function, and substituting the resulting field into the Fresnel diffraction integral yields

$$E_2(r_2,\phi_2) = -iE_{2,1}(r_1)\exp(i\phi) + iE_{2,-1}(r_1)\exp(-i\phi) \tag{70}$$

where

$$E_{2,1}(r_2) = E_0 \frac{k \exp(ikz)}{iz} \exp\left[i \frac{kr_2^2}{2z}\right]$$

$$\cdot \int_0^\infty dr_1 r_1 u(r_1 - r_s) J_1\left(\frac{kr_1r_2}{z}\right) \exp\left(-\frac{r_1^2}{w^2}\right) \exp\left(i\frac{kr_1^2}{2z}\right) \exp(-ik\beta_o r_1) \tag{71}$$

$$E_{2,-1}(r_2) = -E_0 \frac{k \exp(ikz)}{iz} \exp\left[i \frac{kr_2^2}{2z}\right]$$

$$\cdot \int_0^\infty dr_1 r_1 u(r_s - r_1) J_1\left(\frac{kr_1r_2}{z}\right) \exp\left(-\frac{r_1^2}{w^2}\right) \exp\left(i\frac{kr_1^2}{2z}\right) \exp(-ik\beta_i r_1) \tag{72}$$

Here the identity $J_{-n}(x) = (-1)^n J_n(x)$ was employed to express $E_{2,-1}(r)$ in terms of J_1. Solving equations 71 and 72 using the stationary phase approximation yields

$$E_{2,1}(r_2) = e^{-i\frac{3\pi}{4}} \cdot$$

$$E_0 u\left(z - \frac{r_s}{\beta_o}\right) J_1(k_{\perp,o} r_2) \sqrt{\pi \frac{k_{\perp,o}^2 z}{2k}} \exp\left(-\frac{z^2}{l_{df,o}^2}\right) \exp\left(i\frac{kr_2^2}{2z}\right) \exp\left[i\left(k - \frac{k_{\perp,o}^2}{2k}\right)z\right] G_o(z) \tag{73}$$

$$E_{2,-1}(r_2) = e^{i\frac{\pi}{4}} \cdot$$

$$E_0 u\left(z - \frac{r_s}{\beta_i}\right) J_1(k_{\perp,i} r_2) \sqrt{\pi \frac{k_{\perp,i}^2 z}{2k}} \exp\left(-\frac{z^2}{l_{df,i}^2}\right) \exp\left(i\frac{kr_2^2}{2z}\right) \exp\left[i\left(k - \frac{k_{\perp,i}^2}{2k}\right)z\right] G_i(z) \tag{74}$$

where

$$k_{\perp,o} = \beta_o k \tag{75}$$

$$k_{\perp,i} = \beta_i k \tag{76}$$

$$l_{df,o} = \frac{w}{\beta_o} \tag{77}$$

$$l_{df,i} = \frac{w}{\beta_i} \tag{78}$$

For $\frac{r_s}{\beta_o} < z < \frac{r_s}{\beta_i}$, interference between the two Bessel beams is obtained on the optical axis resulting in the field described by

$$\begin{gathered} E_2(r_2, \phi_2) = e^{i\frac{3\pi}{4}} E_0 \cdot \\ \left[J_1(k_{\perp,o} r_2) \sqrt{\pi \frac{k_{\perp,o}^2 z}{2k}} \exp\left(-\frac{z^2}{l_{df,o}^2}\right) \exp\left(i\frac{k r_2^2}{2z}\right) \exp\left[i\left(k - \frac{k_{\perp,o}^2}{2k}\right) z\right] \exp(i\phi)\, G_o(z) + \right. \\ \left. J_1(k_{\perp,i} r_2) \sqrt{\pi \frac{k_{\perp,i}^2 z}{2k}} \exp\left(-\frac{z^2}{l_{df,i}^2}\right) \exp\left(i\frac{k r_2^2}{2z}\right) \exp\left[i\left(k - \frac{k_{\perp,i}^2}{2k}\right) z\right] \exp(-i\phi)\, G_i(z) \right] \end{gathered} \tag{79}$$

Defining the quantity

$$H(r,z) = 1 - \frac{k_{\perp,o}}{k_{\perp,i}} \frac{J_1(k_{\perp,o} r) G_o(z)}{J_1(k_{\perp,i} r) G_i(z)} \exp\left[\left(\frac{1}{l_{df,i}^2} - \frac{1}{l_{df,o}^2}\right) z\right] \tag{80}$$

and rearranging

$$\begin{gathered} E_2(r, \phi) = e^{i\frac{3\pi}{4}} E_0 J_1(k_{\perp,o} r) \sqrt{\pi \frac{k_{\perp,o}^2 z}{2k}} \exp\left(-\frac{z^2}{l_{df,o}^2}\right) \exp\left(i\frac{k r^2}{2z}\right) G_o(z) \\ \left[\exp\left[i\left(k - \frac{k_{\perp,o}^2}{2k}\right) z\right] \exp(i\phi) + \exp\left[i\left(k - \frac{k_{\perp,i}^2}{2k}\right) z\right] \exp(-i\phi)\right] \\ + e^{i\frac{3\pi}{4}} E_0 H(r,z) \cdot \\ J_1(k_{\perp,i} r) \sqrt{\pi \frac{k_{\perp,i}^2 z}{2k}} \exp\left(-\frac{z^2}{l_{df,i}^2}\right) \exp\left(i\frac{k r^2}{2z}\right) \exp\left[i\left(k - \frac{k_{\perp,i}^2}{2k}\right) z\right] \exp(-i\phi)\, G_i(z) \end{gathered} \tag{81}$$

and observing that

$$\begin{aligned}&\exp\left[i\left(k-\frac{k_{\perp,o}^2}{2k}\right)z\right]\exp(i\phi)+\exp\left[i\left(k-\frac{k_{\perp,i}^2}{2k}\right)\right]\exp(-i\phi)\\&\qquad=2\cos\left(\phi-\frac{k_{\perp,o}^2-k_{\perp,i}^2}{4k}z\right)\exp\left[i\left(k-\frac{k_{\perp,o}^2+k_{\perp,i}^2}{4k}\right)z\right]\end{aligned}\tag{82}$$

the diffracted field reduces to

$$\begin{aligned}E(r,\phi)=\ &e^{i\frac{3\pi}{4}}2E_0J_1\left(k_{\perp,o}r\right)\sqrt{\pi\frac{k_{\perp,o}^2z}{2k}}\exp\left(-\frac{z^2}{l_{df,o}^2}\right)\exp\left(i\frac{kr^2}{2z}\right)\cdot\\&G_o(z)\cos\left(\phi-\frac{k_{\perp,o}^2-k_{\perp,i}^2}{4k}z\right)\exp\left[i\left(k-\frac{k_{\perp,o}^2+k_{\perp,i}^2}{4k}\right)z\right]+\ e^{i\frac{3\pi}{4}}E_0H(r,z)\cdot\\&J_1\left(k_{\perp,i}r\right)\sqrt{\pi\frac{k_{\perp,i}^2z}{2k}}\exp\left(-\frac{z^2}{l_{df,i}^2}\right)\exp\left(i\frac{kr^2}{2z}\right)\exp\left[i\left(k-\frac{k_{\perp,i}^2}{2k}\right)z\right]\exp(-i\phi)\,G_i(z)\end{aligned}\tag{83}$$

The irradiance corresponding to the electric field in Equation 83 is

$$\begin{aligned}I(r,\phi)=\ &4\pi\frac{k_{\perp,o}^2z}{2k}I_0J_1^2\left(k_{\perp,o}r\right)\exp\left(-\frac{2z^2}{l_{df,o}^2}\right)|G_o(z)|^2\cos^2\left(\phi-\frac{k_{\perp,o}^2-k_{\perp,i}^2}{4k}z\right)\\&+\ \pi\frac{k_{\perp,i}^2z}{2k}I_0H^2(r,z)J_1^2\left(k_{\perp,i}r\right)\exp\left(-\frac{2z^2}{l_{df,i}^2}\right)G_i^2(z)\\&+4\pi\frac{k_{\perp,o}k_{\perp,i}z}{2k}I_0J_1\left(k_{\perp,o}r\right)J_1\left(k_{\perp,i}r\right)|H(r,z)G_o(z)G_i(z)|\cdot\\&\exp\left[-\left(\frac{1}{l_{df,o}^2}+\frac{1}{l_{df,i}^2}\right)z\right]\cos^2\left(\phi-\frac{k_{\perp,o}^2-k_{\perp,i}^2}{4k}z\right)\end{aligned}\tag{84}$$

In the lim $\beta_i\to\beta_o$, $H(r,z)\to 0$, and the irradiance reduces to

$$I(r,\phi)=\ 4\pi\frac{k_{\perp,o}^2z}{2k}I_0J_1^2\left(k_{\perp,o}r\right)\exp\left(-\frac{2z^2}{l_{df,o}^2}\right)|G_o(z)|^2\cos^2\left(\phi-\frac{k_{\perp,o}^2-k_{\perp,i}^2}{4k}z\right)\tag{85}$$

which is contains both the Bessel profile and the cosine term responsible for rotation found in Equation 65, which are responsible for the fundamental properties of the helical beam. The remaining terms are those found in Equation 61 for a Bessel beam obtained from a Gaussian beam and axicon, and are the artifacts and aperture limitations associated with axicon generation of the non-diffracting beam.

The beam irradiance rotates during propagation according to

$$\theta(r,z) = \phi - \frac{k_{\perp,o}^2 - k_{\perp,i}^2}{4k} \tag{86}$$

with a rotation rate of

$$\frac{\partial\theta}{\partial z} = \frac{k_{\perp,o}^2 - k_{\perp,i}^2}{4k} = \frac{\pi}{2}\frac{\beta_o^2 - \beta_i^2}{\lambda} \tag{87}$$

For the coaxial optical setup, beam rotation is dictated entirely by the two refractive angles used and the wavelength of light. The quadratic dependence of rotation rate implies more full rotations of the helical beam can be obtained for greater refractive angles, as non-diffracting distance scales only as the inverse with respect to the axicon refraction angles.

The scale of the helical beam can also be estimated from Equation 85. Observing that each irradiance peak is bounded by the first and second zeros of $J_1(k_{\perp,o}r)$, the diameter of the individual irradiance peaks cannot exceed

$$d_{max} = \frac{3.8317}{k_\perp} = \frac{1.22\lambda}{\beta_o + \beta_i} \tag{88}$$

The spacing of the helical beam irradiance peaks can similarly be estimated. Assuming each irradiance peak is centered on the first extremum of $J_1\left(k_{\perp,o}r\right)$, and observing that the cosine term in Equation 85 requires an azimuthal separation of π, then the center of the irradiance peaks are separated by a distance of

$$d_{sep} = \frac{3.6824}{k_\perp} = \frac{1.17\lambda}{\beta_o + \beta_i} \quad \textbf{(89)}$$

Equations 87, 88 and 89 illustrate that the refraction angles β_o and β_i dictate the rotation rate, size and separation of the helical beam. The rotation rate scales quadratically with the refraction angles, while the beam diameter scales inversely with respect to these angles. Thus the beam size can be increased at the cost of beam rotation rate.

To obtain helical beams with propagation distances on the order of a meter or more, refraction angles less than a degree are used. Using refraction angles of $\beta_i = 0.15°$ and $\beta_o = 0.25°$ at $\lambda = 800\ nm$ to synthesize helical beams will result in a pair of $140\ \mu m$ helical beams spaced $134\ \mu m$ apart which complete a single rotation about the optical axis every 27 cm as derived from equations 87-89.

3.8 Longitudinal Compression Due to the Addition of a Lens

Bessel and helical beams are assumed to be generated using a collimated Gaussian beam. In practice, departures from collimation may be present, and both Bessel and helical beams may be synthesized using diverging or converging Gaussian beams. Such departures from collimation can be modeled, or even caused by, a lens being placed in series with an axicon. If the lens is assumed to be sufficiently close to the axicon, the resulting diffraction integral only needs to be evaluated once.

To calculate the effects of a lens on an otherwise known diffracted field, assume the incident field originally takes the form

$$E(r,\phi) = f(r)\exp[-ig(r)]\exp(im\phi) \tag{90}$$

Applying the phase of a lens of focal length f

$$E(r,\phi) = f(r)\exp[-ig(r)]\exp\left(-i\frac{kr^2}{2f}\right)\exp(im\phi) \tag{91}$$

and substituting in the Fresnel diffraction integral gives

$$\begin{aligned} E_2(r_2,\phi_2) = {} & (-i)^m E_{2,m}(r_2)\exp(im\phi_2) = (-i)^m \frac{kexp(ikz)}{iz}\exp\left[i\frac{kr_2^2}{2z}\right]\exp(im\phi_2) \\ & \cdot\int_0^\infty dr_1\, r_1 f(r_1) J_m\left(\frac{kr_1r_2}{z}\right)\exp[-ig(r_1)]\exp\left[i\frac{kr_1^2}{2}\left(\frac{1}{z}-\frac{1}{f}\right)\right] \end{aligned} \tag{92}$$

Applying the stationary phase approximation as described previously

$$\psi(r_1) = \frac{kr_1^2}{2}\left(\frac{1}{z}-\frac{1}{f}\right) - g(r_1) \tag{93}$$

$$\frac{\partial \psi(r_1)}{\partial r_1} = k r_1 \left(\frac{1}{z} - \frac{1}{f}\right) - \frac{\partial g(r_1)}{\partial r_1} = 0 \tag{94}$$

$$\frac{\partial^2 \psi(r_1)}{\partial r_1^2} = k \left(\frac{1}{z} - \frac{1}{f}\right) - \frac{\partial^2 g(r_1)}{\partial r_1^2} \tag{95}$$

$$r_1 = \frac{1}{k}\frac{\partial g(r_1)}{\partial r_1}\left(\frac{1}{z} - \frac{1}{f}\right)^{-1} = \left(1 - \frac{z}{f}\right)^{-1}\left(\frac{1}{k}\frac{\partial g(r_1)}{\partial r_1}\right) z = F(z)\beta(r_1) z \tag{96}$$

$$\int \exp\left[\frac{i}{2}\frac{\partial^2 \psi(r_1)}{\partial r_1^2}(r_1 - F(z)\beta(r_1)z)^2\right] dr_1 \tag{97}$$

where

$$\beta(r) = \frac{1}{k}\frac{\partial g(r)}{\partial r} \tag{98}$$

is the generalized refraction angle and

$$F(z) = \left(1 - \frac{z}{f}\right)^{-1} \tag{99}$$

From this equation the effects of a lens can be represented by the transformation

$$z' = \frac{z}{F(z')} \tag{100}$$

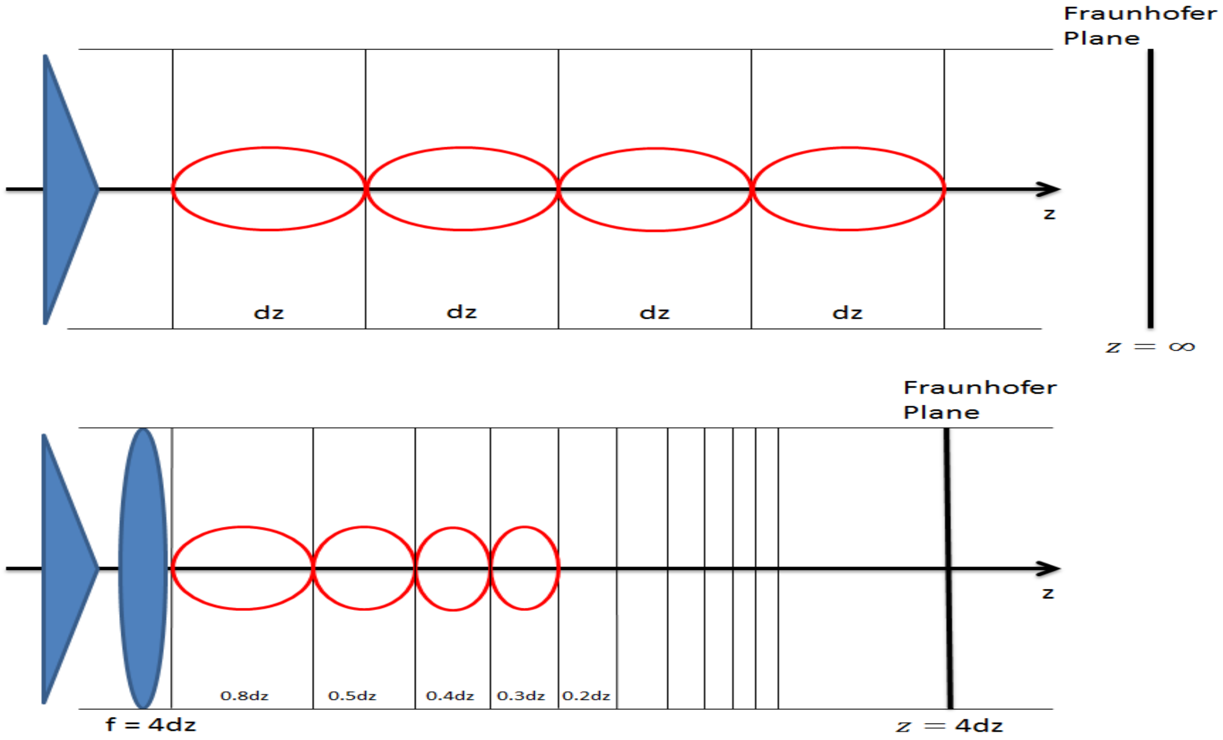

Figure 15: Transformation of the propagation axis illustrating the effect of a lens on non-diffracting beam generation. The propagation axis is compressed as it approaches the Fraunhofer plane. For originally periodic non-diffracting beams, this results in a decrease in beam period during propagation.

Equation 100 describes a spatially dependent contraction of the propagation axis, which is depicted in Figure 15. The contraction of the propagation is highly non-uniform, with no contraction occurring at $z = 0$ and infinite contraction occurring at $z = f$ where the infinite propagation values for the collimated case coincide with the focal plane in the lens augmented case. By contracting the propagation axis for any beam evaluated using the stationary phase approximation for a collimate beam, a new beam shape can be obtained corresponding to identical beam preparation incorporating the addition of a converging lens of focal length f. Mathematically, this process is carried out by applying Equation 100 to the propagation coordinate of any previously evaluated non-diffracting beam.

3.9 Numerical Modeling of Helical Beams

A Fresnel diffraction solver was written in MATLAB (R2008a version 7.6.0.324) to generate two-dimensional irradiance plots of diffracted light fields. This solver was used both as a model to compare against experiments, and as a means to devise efficiently manufactured phase elements for the generation of diffraction free beams. Through a numerical implementation of the Fresnel diffraction integral, the solver was able to calculate a diffracted irradiance distribution an arbitrary distance from an incident wavefront, assuming the Fresnel criteria are satisfied.

The Fresnel diffraction integral was implemented using a fast-Fourier transform. Starting with the Fresnel diffraction integral

$$E_2(x_2, y_2, z) = \frac{e^{ikz}}{i\lambda z} \iint_{-\infty}^{\infty} E_1(x_1, y_1, 0) \exp\left[\frac{ik}{2z}\left((x_2 - x_1)^2 + (y_2 - y_1)^2\right)\right] dx_1 dy_1 \tag{101}$$

defining $K = \frac{k}{2z}$ and rearranging gives

$$E(x_2, y_2, z) = \frac{e^{ikz}}{i\lambda z} \exp[iK(x_2^2 + y_2^2)] \cdot \iint_{-\infty}^{\infty} E_1(x_1, y_1, 0) \exp[iK(x_1^2 + y_1^2)] \exp[-i2K(x_1 x_2 + y_1 y_2)]\, dx_1 dy_1 \tag{102}$$

Making the change of variables

$$u = 2Kx_2 \tag{103}$$

$$v = 2Ky_2 \tag{104}$$

$$E_2(u, v, z) = \frac{e^{ikz}}{i\lambda z} \cdot \tag{105}$$

$$\exp\left[\frac{i}{4K}(u^2+v^2)\right]\iint_{-\infty}^{\infty}E_1(x_1,y_1,0)\exp[iK(x_1^2+y_1^2)]\exp[-i(ux_1+vy_1)]\,dx_1dy_1$$

and applying the definition of the Fourier transform gives

$$E_2(u,v,z)=\frac{e^{ikz}}{i\lambda z}\exp\left[\frac{i}{4K}(u^2+v^2)\right]\mathcal{F}[E_1(x_1,y_1,0)\exp[iK(x_1^2+y_1^2)]] \tag{106}$$

The Fresnel diffraction code was implemented by applying Equation 106 to a numerical representation of a spatially resolved electromagnetic wavefront. The Fourier transform in Equation 106 was implemented using a two-dimensional fast-Fourier transform algorithm, which was provided as a standard functional routine in MATLAB. The change of variables in the plane of the diffracted field was accounted for by rescaling the *x* and *y* axes of the diffracted field.

The model flow chart is provided in Figure 16. The model uses a two-dimensional fast-Fourier transform to implement a discretized Fresnel diffraction integral as described above. Optical elements were simulated using spatially resolved phase delays that were applied to two-dimensional representations of an incident collimated Gaussian beam before the diffraction integral is evaluated. The distance between the incident beam and the diffracted field is incorporated as a numerical argument within the Fresnel diffraction integral.

Numerical simulations were used to evaluate optical setups used in the synthesis of a variety of Bessel beams and helical beams, and used to evaluate individual components used within these optical setups, such as vortex plates. For each optical configuration of interest, the simulation was run for a range of propagation distance.

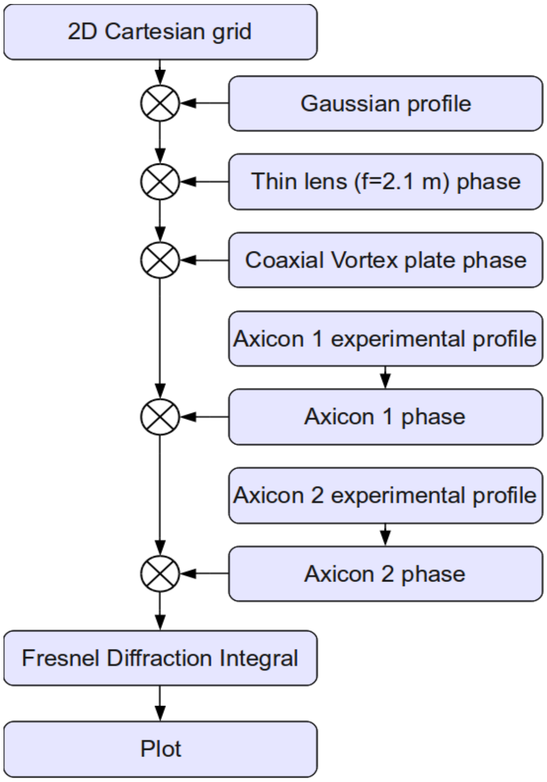

Figure 16: Fresnel diffraction simulation flowchart.

The simulation was also used to reproduce all non-diffracting beams experiments carried out and used as a benchmark for comparison. For these cases, the simulated optical setup was configured to provide the best possible approximation of experiment. To better represent optical elements used within the experiment, a Zygo microscope was used to characterize the surfaces of both axicons used in the experiments. The phase lag used to simulate these elements was then calculated directly from the surface data obtained using the microscope.

The simulation was also employed in the design of many of the optical elements used in experiments. To obtain arbitrary phase profiles, such as those used in the vortex plates, additive phase lithography was employed to fabricate specialized phase plates to match the phase profiles required by experiment [81]. The phase lag variations obtained from the phase plates result from changes in phase plate thickness, so that thickness profile of the plates correspond to the phase profile modification of beams transmitted through the plates.

As a consequence of the fabrication method, phase plate thickness cannot be varied continuously. Rather, the thickness profile is obtained from a series of discrete steps used to approximate a continuous profile. The greater number of discrete steps required, the better the approximation to the continuous profile. However, additional steps require additional fabrication mask, which increase the cost of fabrication. To avoid incurring excessive fabrication cost, the Fresnel diffraction code was used to simulate phase plates fabricated using a varying number of discretized steps, to determine the minimum number of steps required to obtain the desired refraction pattern from the device.

3.10 Helical Beam Experimental Setup

Helical beams were generated using both continuous and pulsed laser light [6]. For both experiments, the MTFL laser was used as the light source. To produce the wavefront necessary to generate helical beams, the configuration shown in Figure 14 had to be implemented in an experimental setting. The resulting setup is shown in Figure 17.

Like its conceptual counterpart, the experimental setup employed a pair of 5 mm diameter vortex plates in series with a pair of 1” diameter axicons. Unlike the conceptual layout, the radius separating the azimuthal phases, 1.25 mm, and that separating the refractive angles, 6.35 mm, were not equal. Thus telescoping optics were implemented to enlarged the collimated the incident Gaussian beam after transmission through the phase plate, so the virtual separation radius of the plates in the magnified beam matched that of the axicons.

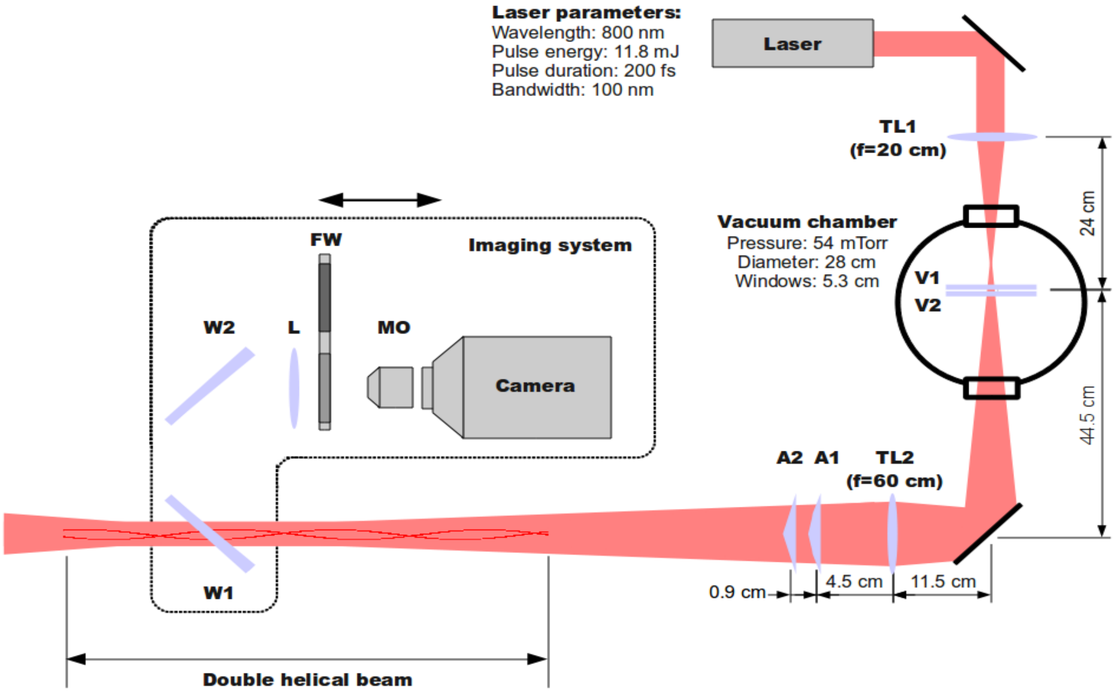

Figure 17: Optical setup used to generated and characterize continuous and pulsed helical beams. TL1 and TL2 form a telescope which increases the beam diameter by a factor of 3.

The setup in Figure 17 consists of the MTFL laser, a telescope, the vortex plates, and the axicon pair. The focal spot of the telescope is placed within a 28 cm diameter cylindrical vacuum chamber kept at 54 mTorr to prevent plasma formation when using pulsed laser light. Collimated light from MTFL is transmitted through a telescope composed of a 20 cm(TL1) and a 60 cm (TL2) converging lens separated by 80 cm. The vortex plates (V1, V2) were located 4 cm beyond the internal focus of the telescope, also within the vacuum chamber. The axicons (A1, A2) were placed 4.5 cm beyond the telescope and aligned with the optical axis.

The vortex plate pair, depicted in Figure 18, consisted of two 5 mm diameter phase plates. One plate induced an azimuthal charge of $\exp(i\phi)$ on the beam lying outside a radius of 1.25 mm, while a second plate induces an azimuthal charge $\exp(-i\phi)$ for the beam lying within the 1.25 mm radius. The vortex plates were fabricated using an additive micro-lithographic technique from fused silica [81]. The vortex plates consisted of 16 azimuthal segments of constant thickness arranged to form a unit topological vortex at 800 nm. Discrete levels were first created in photoresist and then transferred to fused silica using CHF_3:O_2 inductively coupled plasma etching.

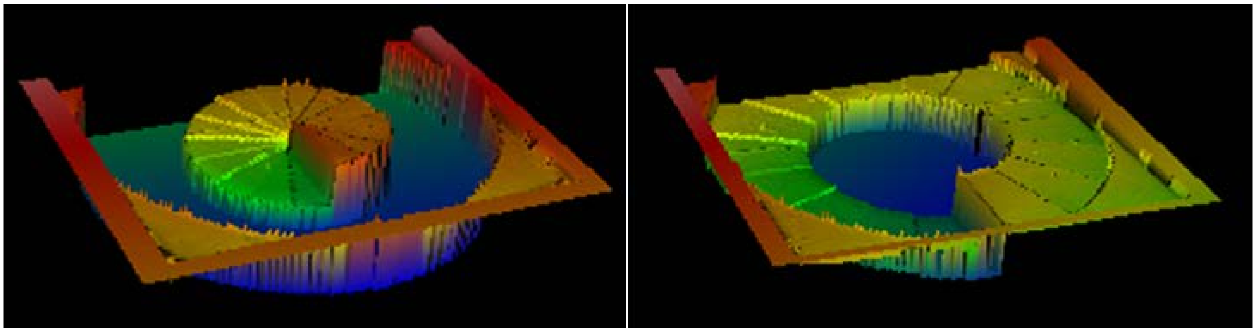

Figure 18: Three-dimensional color map renderings of the surface of the two vortex plates used in experiments. The sign azimuthal charge associated with each plates can be switched by inverting the plate orientation.

Two 1” diameter axicons were placed in series at the output of the telescope. The first of the pair was a specialized axicon which provided two refraction angles: an angle of $\beta_o = 0.28°$ for $r > 6.35\,mm$ and refraction angle of $\beta_i = 0.10°$ for $r < 6.35\,mm$. A conventional axicon, which provided a fixed refraction angle of $\beta = 0.15°$, was placed immediately after this element.

Collectively, the series arrangement of axicons resulted in refraction angles of $\beta_o = 0.43^o$ and $\beta_i = 0.25^o$.

MFTL was used to generate both continuous and pulsed light. Measured power output was 290 mW. The laser center wavelength was measured to be 785 nm. Spectral bandwidth was measured to be 75 nm FWHM during modelocked operation, and 1 nm FWHM during continuous operation. Laser chirp was uncompensated, resulting in 100 fs pulses during modelocked operation. The modelocked repetition rate was 75 MHz.

Through the use of the telescope configuration, the vortex plate phase was expanded and projected onto the axicon pair such that the separation radius of the projected phase and the first axicon matched (Figure 17). The Gaussian beam waist was 33.5 mm of immediately after the telescope, overfilling the axicons. Beam clipping on the 25 mm diameter axicons resulted in a 76% power loss. The filament imaging system was used to evaluate the transverse irradiance profiles of both the continuous and pulsed helical beams.

By substituting the parameters of the experimental setup into the expression provided in the theory sections of the chapter, helical beam characteristics can be predicted. Incorporating the 2.1 *m* effective focal length of the telescope and using equations 73 and 74 in conjunction with the transformation given by Equation 100, the helical beam was expected to propagate from 54 *cm* to 85 *cm*. Substituting the experimental refraction angles into Equation 87 and again applying Equation 100, the helical beam should rotate at a rate of one cycle every 4.7 cm at 54 cm, accelerating to a rotation rate of one cycle every 3.0 cm at 85 cm. Evaluating Equation 88 at 54 *cm*, the maximum spot size of each irradiance peak should not exceed 54 μm.

3.11 Helical Beam Experimental Results

Helical beams were initially generated using a 785 nm continuous laser beam. Transverse beam profile images were recorded in 5 mm intervals along the optical axis. The helical beam was found to propagate from $60 \pm 0.5\ cm$ from the experimental setup to $80 \pm 0.5\ cm$, which falls within the propagation range predicted by theory.

The helical beams obtained using the continuous light are shown in the second row of Figure 19. The helical beams were composed of two $50\ \mu m$ diameter irradiance peaks, falling within the $54\ \mu m$ maximum spot size predicted from Equation 88, separated by a $25\ \mu m$ null. The beam structure as a whole measured $125\ \mu m$ across. At each point along the optical axis within the beam propagation range, a helical beam irradiance profile is observed. Sideband flares resulting from irradiance peaks present in the second ring associated with $J_1^2(r)$ are also present in many of the observed irradiance profiles.

The results were compared against a simulation of the experimental setup in Figure 17 carried out using the numerical model described in the previous section. A comparison between numerical and experimental results is provided in Figure 19 along one full rotation of the helical beam. Irradiance profiles obtain from experiment and simulation share three important features. All experimental profiles contain two identifiable irradiance peaks, although almost equally intense sidebands are present in many of the profiles. A clear null is also always present at the center of the beam structure. Finally, experimentally rates of rotation agree with those found within the simulation.

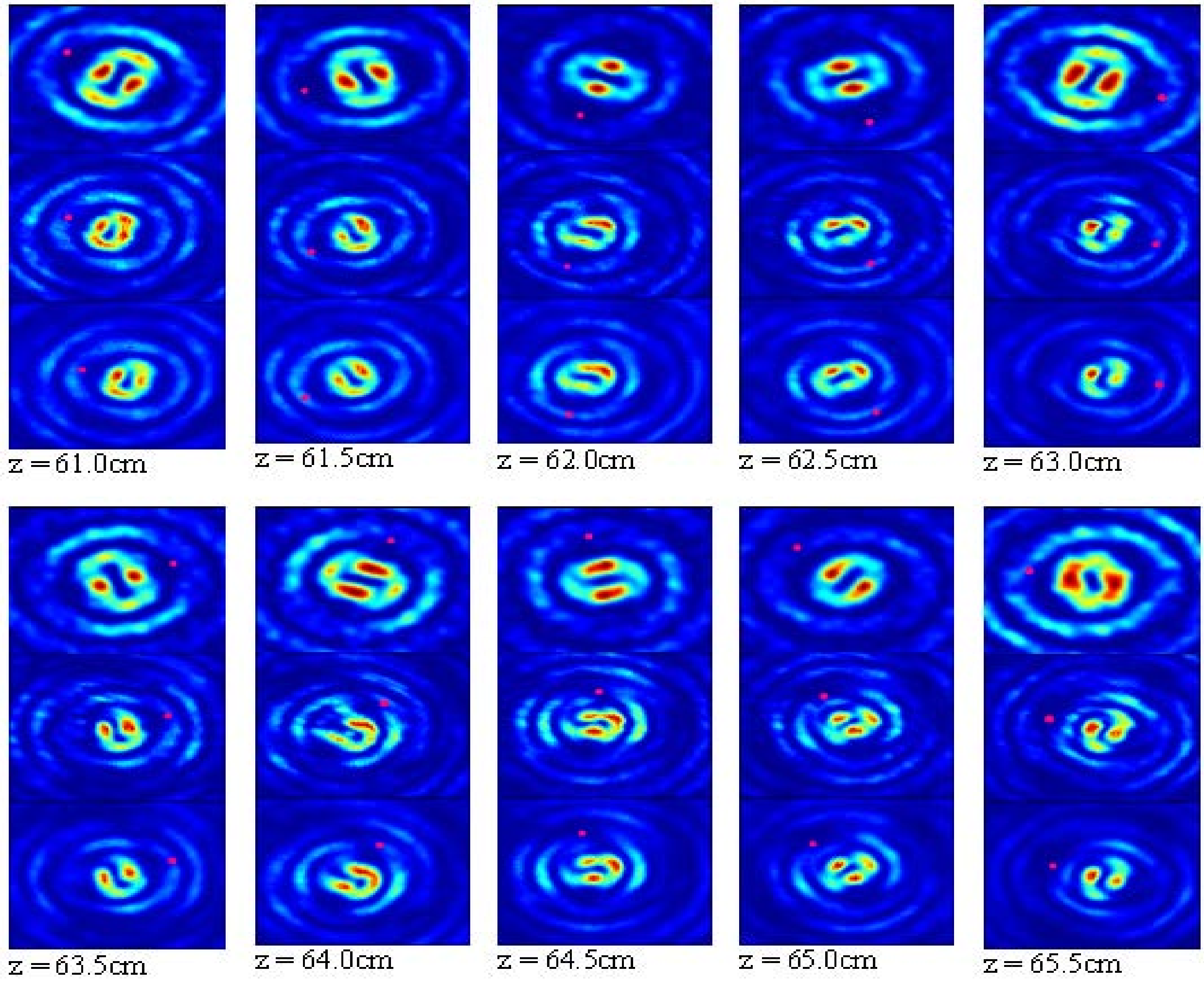
z = 61.0cm
z = 61.5cm
z = 62.0cm
z = 62.5cm
z = 63.0cm
z = 63.5cm
z = 64.0cm
z = 64.5cm
z = 65.0cm
z = 65.5cm

Figure 19: Transverse helical beam profiles as a function of propagation distance obtained using the setup shown in Figure 17 from both simulation and experiment. Upper Row: Simulation, Middle Row: Continuous Beam, Bottom Row: Pulsed Beam

The rotation angle for both simulation and experiment were obtained from their irradiance profiles and are plotted in Figure 20 as a function of propagation distance. Agreement between experiment and simulation can be observed directly from the plot. From the plot, the helical beam can be observed to make a complete rotation approximately every 4 *cm*. The same conclusion can be made by analyzing Figure 19. This rotation rate is also predicted by Equation 87 for a distance of 65 *cm*. However, variations in the rate of rotation due to the 2.1 *m* effective focal length of the telescope as a consequence of the transformation given in Equation 100 are not observed.

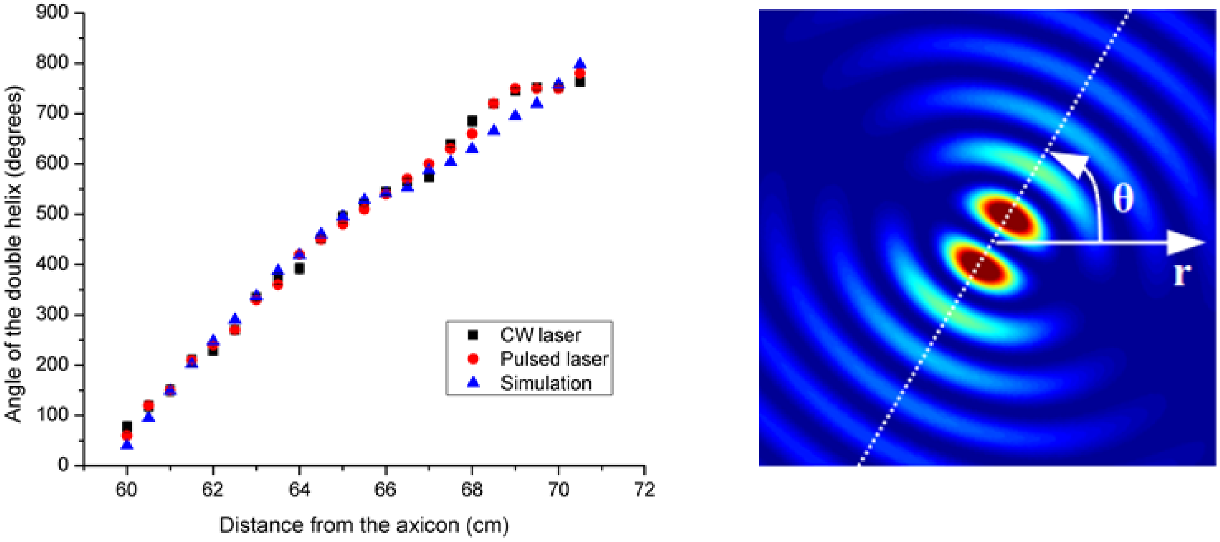

Figure 20: Cumulative rotation angle as a function of propagation distance. The way in which the rotation angle is defined is show on the right figure, while the data is plotted in the left figure.

The experiment was repeated using ultrafast pulses. As in the continuous case, the helical beam was observed to propagate from 60 to 80 *cm*. The transverse profiles recorded for pulsed helical beams were nearly identical to those obtained for the continuous case, as shown in Figure 19, and exhibit the same rotation angle and rate, as can be seen in Figure 20. Pulsed helical beams were found to exhibit a clearer irradiance structure than their continuous counterparts. It is hypothesized that this is a consequence of MTFL’s optimization for pulsed operation.

3.12 Conclusion

A serial arrangement for generating double helical beams through the interference of two first order Bessel beams has been successfully demonstrated. Although this arrangement was devised through the application of linear diffraction theory to a continuous Gaussian beam, the configuration has also been demonstrated to operate with ultrafast pulses. A diffraction model was able to provide an adequate description of the double helical beam dimensions and rotation rate. The transverse beam profiles obtained through the simulation reproduced the basic structural features of the helical beam profiles obtained in the laboratory. These models can be extended to pulsed beams on a limited basis.

Experimentally obtained double helical beams produced rapid, consistent and controlled rotations dictated by the optical setup in a manner consistent with analytical and numerical models. Double helical beam dimensions, rotation rate and propagation distance can be readily altered by appropriate selection of optical elements, demonstrating the extensive control that can be obtained over beam propagation through the understanding and application of diffraction theory.

CHAPTER 4: LASER FILAMENTATION IN AIR

Ultrafast laser pulses above critical power (typically 3 GW in normal air) undergo filamentation during propagation through transparent media [82]. The irradiance of such light filaments is of the order 10-100 TW/cm^2, which is sufficient to ionize oxygen and nitrogen through a combination of multi-photon and tunneling ionization [82] [7] [83]. This results in a plasma channel at the core of the light filament. The collective nonlinear effects involved in the propagation of a laser filament, including self-focusing through the Kerr effect and defocusing due to the free electrons present in the plasma core, enable the propagation of a limited beam diameter laser pulse well beyond the Rayleigh range predicted through diffraction theory, leading to a behavior described as self-channeling [84]. Because of these properties, filamentation provides a unique means to deliver confined radiation over extended propagation distances, and to generate unique plasma structures in air.

4.1 Filament Characteristics

The interplay between the nonlinear effects and plasma formation responsible for the formation of laser plasma filaments enable laser filaments to adopt a number of physical characteristics that are independent of the laser used to generate the filament. Filaments form when the instantaneous power of an ultrafast pulse is sufficient to overcome linear diffraction through Kerr self-focusing [85] [82]. This limit is defined as the critical power, which for Gaussian beams is given as:

$$P_{cr} = \frac{3.77\lambda^2}{8\pi n_2 n_0} \tag{107}$$

In air, this limit is 5-10 GW for pulses less than 100 fs in duration [86] (for pulses exceeding 100 fs, the molecular response contributions increase the Kerr index, altering this value). Because of the large instantaneous powers required for filament formation, in practice filaments are generated using high energy ultrafast pulses.

Laser filaments are composed of a high irradiance core surrounded by a lower irradiance peripheral field. Light in the core takes on a Townesian profile [87] [88] and measures 50 to 120 μm in diameter [7] [89] [82]. Irradiance in the core is between 10 and 100 TW/cm^2, which is sufficient to generate a plasma density of at least $10^{16}\ cm^{-3}$ [85] [82] [90]. Plasma formation limits core peak irradiance to 100 TW/cm^2, regardless of the pulse energy used to form the filament [91] [28]. Increasing laser pulse energy beyond that necessary to achieve filamentation will instead resulting in the formation of multiple filaments, with each additional filament sharing the same approximate physical properties and dimensions with those of a single filament core [92] [93].

Surrounding the filament core is the peripheral field. The peripheral field is a region of coherent ultrafast light extending from the filament core to a radial distance comparable to the initial diameter of the beam responsible for generation of the filament. Peripheral field irradiance is approximately a hundredth of that found within the filament core, in the range 0.1 TW/cm^2 to 1 TW/cm^2. The peripheral field serves as an energy reservoir which replenishes energy lost to plasma absorption in the core, enabling extended propagation of the filament [94] [95]. It can also provide energy to replenish the filament core should the core be truncated by an obstruction during propagation, resulting in the “regeneration” of the filament [96] [97].

4.2 Filamentation Physics

Filamentation begins with laser self-focusing, which is driven by the Kerr effect. The Kerr effect is an increase in the refractive of a dielectric that is proportional to the field irradiance. Mathematically, the Kerr effect can be expressed as [82]

$$n = n_0 + n_2 I \tag{108}$$

where n_0 is the linear diffractive index, and n_2 is the Kerr index, both of which are properties of the optical medium. When the optical field is spatially inhomogeneous, the Kerr effect will modify the wavefront of a propagating electromagnetic wave due to changes in the irradiance based refractive index along the wavefront.

In the special case where a Gaussian beam, a typical and reasonably accurate approximation of most laser beams, is responsible for the spatial inhomogeneity, the Kerr effect can be shown to act as a spherical lens in the $\lim r \to 0$. Starting with a Gaussian beam of beamwaist *w* described by

$$I(r) = I_0 \exp\left(-\frac{r^2}{w^2}\right) \tag{109}$$

and substituting the irradiance into Equation 108 gives

$$n(r) = n_0 + n_2 I_0 \exp\left(-\frac{r^2}{w^2}\right) \quad \textbf{(110)}$$

Applying the Maclaurin series expansion [98] to the refractive index results in the power series

$$n(r) = n_0 + n_2 I_0 - \frac{n_2 I_0}{w^2} r^2 + \frac{n_2 I_0}{2w^4} r^4 + O(r^6) \quad \textbf{(111)}$$

The corresponding modification to the wavefront phase is

$$\exp[ikn(r)z] = \exp(ikn_0 z)\exp(ikn_2 I_0 z)\exp\left(-i\frac{kn_2 I_0 z}{w^2} r^2\right)\exp\left(i\frac{kn_2 I_0 z}{2w^4} r^4\right) \quad \textbf{(112)}$$

In the lim $r \to 0$ and over a length δz this expression reduces to

$$\exp[ikn(r)\delta z] = \exp(ik'\delta z)\exp\left(-i\frac{kn_2 I_0 \delta z}{w^2} r^2\right) \quad \textbf{(113)}$$

Comparing this approximate wavefront to that for a spherical lens

$$\exp\left(-i\frac{k}{2f} r^2\right) = \exp\left(-i\frac{kn_2 I_0 \delta z}{w^2} r^2\right) \quad \textbf{(114)}$$

gives an equivalent focal length for the Kerr effect resulting from propagating a finite distance δz through a Kerr media

$$f_{kerr} = \frac{w^2}{2n_2 I_0 \delta z} \quad \textbf{(115)}$$

Thus, in this limit the Kerr effects modifies the wavefront of the Gaussian beam in a manner identical to that of a lens of focal length f_{kerr}.

However, for large *r*, this approximation ceases to be valid. In particular, at

$$r(z) = \sqrt{2}w(z) \quad \textbf{(116)}$$

the quadratic correction in the Maclaurin series overtakes to linear correction and the analogy to a lens ceases to be valid.

While a spherical lens will refract the entirety of the incident field such that all radiated will be confined to a diffraction limited spot within the focal plane of the lens, the optical Kerr effect will only refract light sufficiently close to the optical axis, where the approximation in Equation 113 remains valid, into a diffraction limited spot. Because the beam waist continually contracts under the effect of propagation, the radius for which the Kerr lens approximation will be valid decreases during propagation, approaching zero in the limit. This results in the presence of beam energy at all distances from the optical axis within the diameter of the original beam that has not been refracted into the core of the filament, which form the peripheral field.

4.3 Nonlinear Schrodinger Equation

The nonlinear Schrodinger equation can be derived from Maxwell's equations in a media with a nonlinear polarization response. This equation is obtained by making a slowly varying envelope approximation along the propagation axis [99].

Starting with the wave equation

$$\vec{\nabla} \times \left(\vec{\nabla} \times \vec{E}\right) + \frac{1}{c^2}\frac{\partial^2 \vec{E}}{\partial t^2} = -\frac{1}{\epsilon_0 c^2}\frac{\partial^2 \vec{P}}{\partial t^2} \tag{117}$$

$$\vec{\nabla}^2 \vec{E} - \frac{1}{c^2}\frac{\partial^2 \vec{E}}{\partial t^2} = \frac{1}{\epsilon_0 c^2}\frac{\partial^2 \vec{P}}{\partial t^2} + \vec{\nabla}\left(\vec{\nabla} \cdot \vec{E}\right) \tag{118}$$

The nonlinear Schrodinger equation is obtained by making the envelope approximation

$$\vec{E} = A(x,y,z)\exp[i(kz-\omega t)]\,\hat{e} + A(x,y,z)\exp[-i(kz-\omega t)]\,\hat{e} \tag{119}$$

This approximation is valid for

$$\left|\frac{\partial^2 A}{\partial z^2}\right| \ll \left|2k\frac{\partial A}{\partial z}\right| \tag{120}$$

Assuming a Gaussian envelope of the form

$$A(x,y,z) = A_0(x,y)\exp\left[-\frac{z^2}{(c\tau)^2}\right] \tag{121}$$

Substituting this expression back into Equation 120 gives

$$\left|\frac{z^2}{(c\tau)^2} - 1\right| \ll \frac{4\pi z}{\lambda} \tag{122}$$

Limiting z to $|z| < 2c\tau$ reduces Equation 122 to

$$\tau \gg \frac{3\lambda}{8\pi c} \tag{123}$$

At 800 nm, Equation 123 reduces to

$$\tau \gg 0.32\,fs \tag{124}$$

Thus pulses several femtoseconds in duration should satisfy the slowly varying envelope approximation. Substituting the envelope expansion into Equation 118 (see Appendix E) yields the nonlinear Schrodinger equation:

$$2ik\frac{\partial A}{\partial z} + \nabla_\perp^2 A + 3k^2\frac{\hat{\chi}_3(\omega,-\omega,\omega)}{1+\hat{\chi}_1(\omega)}|A|^2 A = 0 \tag{125}$$

The nonlinear Schrodinger equation describes the nonlinear propagation of an electromagnetic wave through a Kerr media when the envelope approximation is valid [100].

4.4 Ionization within a Filament

Due to their high instantaneous irradiance, filaments are able to ionize the air through a combination of multiphoton and tunneling ionization [82]. This results in a plasma which persist for $\cong 1\, ns$ and decays over the course of $\cong 200\, ns$ [101]. The plasma in the filament core is a weakly ionized air plasma possessing a density of approximately 10^{16} electrons/cm^3, or a 0.1% ionization of the air. The air plasma present in the filament core is essential to stabilizing the filament during propagation, as it reduces the core refractive index, counteracting the optical Kerr effect and preventing the formation of an optical singularity.

The dynamics of filament ionization in air are given by [82]

$$\frac{\partial \rho}{\partial t} = W(I)(\rho_{at} - \rho) + \frac{\sigma}{U_i}\rho I \tag{126}$$

where $W(I)$ is the photoionization rate, ρ is the plasma density and ρ_{at} is the atmospheric density. The photoionization rate is then broken down into the multiphoton ionization rate [102] [82]

$$W(\omega_0, I) = \sigma_k I^k \tag{127}$$

where σ_k is the mutliphoton ionization cross-section for a k photon process, and the tunneling ionization rate is given by [82]

$$W(E) = \omega_{a.u.} \left| C_{n*,l*} \right|^2 \frac{U_0}{2U_{it}} \sqrt{\frac{6}{\pi}} \left(\frac{2E_0}{E} \right)^{2n* - \frac{3}{2}} \exp\left(-\frac{2E_0}{E} \right) \quad \textbf{(128)}$$

By considering the multiphoton effects in isolation and assuming the irradiance is given a priori, the ionization dynamics can be reduced to

$$\frac{\partial \rho}{\partial t} = \sigma_k I^k (\rho_{at} - \rho) \quad \textbf{(129)}$$

Rearranging Equation 129 yields a first order inhomogeneous differential equation

$$\frac{\partial \rho}{\partial t} + \sigma_k I^k \rho = \sigma_k I^k \rho_{at} \quad \textbf{(130)}$$

For a constant irradiance, Equation 130 has the general solution

$$\rho(t) = A \exp(-\sigma_k I^k t) + f(t) \quad \textbf{(131)}$$

For the initial condition $\rho = 0$ at $t = 0$, this reduces to

$$\rho(t) = \rho_{at} [1 - \exp(-\sigma_k I^k t)] \quad \textbf{(132)}$$

Thus for a laser pulse of duration τ, the plasma density can be approximated by

$$\rho = \rho_{at} [1 - \exp(-\sigma_k I^k \tau)] \quad \textbf{(133)}$$

Equation 130 can also be solved for a temporal Gaussian pulse to better approximate ultrafast laser pulse. Starting with a Gaussian pulse of temporal duration τ described by

$$I = I_0 \exp\left[-\frac{2t^2}{\left(\frac{\tau}{2}\right)^2} \right] = I_0 \exp\left(-\frac{8t^2}{\tau^2} \right) \quad \textbf{(134)}$$

Substituting the Gaussian irradiance into Equation 130 yields

$$\frac{\partial \rho}{\partial t} = \sigma_k I_0^k \exp\left(-\frac{8kt^2}{\tau^2}\right)(\rho_{at} - \rho) \tag{135}$$

This equation is of the form

$$\frac{\partial x}{\partial t} + \alpha x \exp(-at^2) = \beta \exp(-at^2) \tag{136}$$

Evaluating the homogenous part

$$\frac{\partial x}{\partial t} + \alpha x \exp(-at^2) = 0 \tag{137}$$

and rearranging

$$\frac{\partial x}{x} = -\alpha \exp(-at^2)\, \partial t \tag{138}$$

and integrating

$$\ln(x) = -\alpha \int \exp(-at^2)\, \partial t = -\frac{\alpha}{2}\sqrt{\frac{\pi}{a}}\operatorname{erf}(\sqrt{a}t) \tag{139}$$

gives the general solution

$$x = A \exp\left[-\frac{\alpha}{2}\sqrt{\frac{\pi}{a}}\operatorname{erf}(\sqrt{a}t)\right] + f(t) \tag{140}$$

Solving for the inhomogeneous part and requiring $x = 0$ at $t = 0$ gives

$$x = \frac{\beta}{\alpha}\left[1 - \exp\left(-\frac{\alpha}{2}\sqrt{\frac{\pi}{a}}\operatorname{erf}(\sqrt{a}t)\right)\right] \tag{141}$$

Making the substitutions

$$\alpha = \sigma_k I_0^k \tag{142}$$

$$\beta = \sigma_k I_0^k \rho_{at} \tag{143}$$

$$a = \frac{8k}{\tau^2} \tag{144}$$

And substituting

$$\rho = \rho_{at}\left[1 - \exp\left(-\frac{\sigma_k I_0^k \tau}{4}\sqrt{\frac{\pi}{2k}}\operatorname{erf}\left(\frac{2}{\tau}\sqrt{\frac{2}{k}}t\right)\right)\right] \tag{145}$$

At times well after the laser pulse has passed, but before the plasma has recombined with the air, $t \gg \frac{\tau}{2}\sqrt{\frac{k}{2}}$, for which Equation 145 reduces to

$$\rho = \rho_{at}\left[1 - \exp\left(-\frac{\sigma_k I_0^k \tau}{4}\sqrt{\frac{\pi}{2k}}\right)\right] = \rho_{at}\left[1 - \exp\left(-\kappa\sigma_k I_0^k \tau\right)\right] \tag{146}$$

where

$$\kappa = \frac{1}{4}\sqrt{\frac{\pi}{2k}} \tag{147}$$

Equation 146 can further be evaluated by applying tabulated atmospheric data. Taking the atmospheric density values

$$\rho_{O_{2},n} = 2.4 \cdot 10^{-7}\,\frac{kg}{cm^3}$$

$$\rho_{N_{2},n} = 9.6 \cdot 10^{-7}\,\frac{kg}{cm^3}$$

and taking the multiphoton ionization cross-section for 800 nm from Couairon et al. [82]

$$\sigma_{8,O_2} = 2.81 \cdot 10^{-96}\,\frac{s \cdot cm^{16}}{W^8}$$

$$\sigma_{11,N_2} = 6.31 \cdot 10^{-140} \frac{s \cdot cm^{22}}{W^{11}}$$

and substituting the ionization rate equation yields the ionization value for oxygen and nitrogen as a function of peak irradiance and pulse duration

$$\rho_{O_2,e} = 2.4 \cdot 10^{-7} \frac{kg}{cm^3} \left[1 - \exp\left(-\left(\frac{I_0}{86.6 \frac{TW}{cm^2}} \right)^8 \frac{\tau}{fs} \right) \right] \quad \textbf{(148)}$$

$$\rho_{N_2,e} = 9.6 \cdot 10^{-7} \frac{kg}{cm^3} \left[1 - \exp\left(-\left(\frac{I_0}{119 \frac{TW}{cm^2}} \right)^{11} \frac{\tau}{fs} \right) \right] \quad \textbf{(149)}$$

Equations 148 and 149 provide physical values for the plasma density obtained through a purely multiphoton ultrafast pulse driven ionization process in air.

4.5 Effects of the Plasma on Filament Propagation

The plasma present at the core of a filament is fundamental to the propagation physics of the filament. The core plasma plays two important roles in filament propagation. First, the presence of the plasma reduces the local refractive index in the core of the filament, counteracting the filament and preventing optical collapse [10]. Second, the formation of the plasma requires energy from the ultrafast pulse responsible for filamentation to drive the ionization process. This introduces an energy loss mechanism that slowly depletes the energy present in the filament. Once the energy in the filament is insufficient to maintain the instantaneous power necessary to counteract diffraction through the Kerr effect, the filament will diffract and end.

The reduction in refractive index due to the presence of a plasma can be mathematically represented as [103] [82]

$$n = n_0 - \frac{\rho}{2\rho_c} \tag{150}$$

where ρ is the plasma density of the filament and ρ_c is the plasma critical density.

4.6 Rayleigh-Sommerfeld Model

The Fresnel diffraction integral proved effective and predicting and modeling beam propagation in the previous chapter, where only linear beam propagation needed to be considered. To deal with nonlinearities using diffraction integrals, nonlinearities can be modeled as irradiance dependent phase lags. This approach requires repeated diffraction calculations over short, incremental distances to account for the changes in the nonlinear contributions to the refractive index during beam propagation. Both the Fresnel and Fraunhofer diffraction integrals require a minimum propagation distance to satisfy the underlying assumptions required for the validity of the integrals, and are unsuitable for any approach that requires vanishing propagation distances in the limit.

The Rayleigh-Sommerfeld integral is not subject to any limits on propagation distance and is therefore valid in the limit $dz \to 0$. In cylindrical coordinates, the Rayleigh-Sommerfeld diffraction integral can be expressed as

$$E_2(r_2,\theta_2,z) = \frac{1}{i\lambda}\iint r_1 E_1(r_1,\theta_1)\frac{\exp(ikl)}{l}\cos(\vec{n}\cdot\vec{l}) \tag{151}$$

where

$$l = \sqrt{r_1^2 + r_2^2 - 2r_1 r_2\cos(\theta_2 - \theta_1) + z^2} \tag{152}$$

and $\vec{n}$ is the normal relative to the surface associated with the incident field. When considering incident and diffracted fields on a pair of parallel plane separated by a finite distance, the cosine term reduces to

$$\cos^2(\vec{n}\cdot\vec{l}) = 1 - \sin^2(\vec{n}\cdot\vec{l}) = \frac{z^2}{l^2} \tag{153}$$

$$\cos(\vec{n}\cdot\vec{l}) = \frac{z}{l} \tag{154}$$

Substituting back into the Rayleigh-Sommerfeld integral gives

$$E_2(r_2,\theta_2,z) = \frac{z}{i\lambda}\iint r_1 E_1(r_1,\theta_1)\frac{\exp(ikl)}{l^2}dr_1 d\theta_1 \tag{155}$$

For an azimuthally symmetric field the Rayleigh-Sommerfeld integral reduces to

$$E_2(r_2,z) = \frac{z}{i\lambda}\int dr_1\, r_1 E_1(r_1)\int d\theta\,\frac{\exp(ikl)}{l^2} \tag{156}$$

where

$$l = \sqrt{r_1^2 + r_2^2 - 2r_1 r_2 \cos\theta + z^2} \tag{157}$$

While this integral lacks a simple analytical solution it does possess an elegant numerical solution. Converting the double integral in Equation 156 to a double sum over with infinitesimal propagation distance *dz*

$$E_2(r_2, z) = \frac{dz}{i\lambda} \sum_{r_1} \delta r_1 r_1 E_1(r_1) \sum_{\theta} \delta\theta \frac{\exp(ikl)}{l^2} \tag{158}$$

defining the matrix $\widehat{\boldsymbol{K}}$ using the matrix elements

$$\widehat{\boldsymbol{K}}_{r_1, r_2} = \sum_{\theta} \delta\theta \frac{\exp[ikl(r_1, r_2, dz)]}{l^2(r_1, r_2, dz)} \tag{159}$$

and defining the arrays

$$\boldsymbol{r}_1 = [0{:}\,\delta r_1{:}\,n\delta r_1] \tag{160}$$

$$\boldsymbol{r}_2 = [0{:}\,\delta r_2{:}\,n\delta r_2] \tag{161}$$

$$\boldsymbol{E}_1 = [E_1(0){:}\,E_1(\delta r_1){:}\,E_1(n\delta r_1)] \tag{162}$$

$$\boldsymbol{E}_2 = [E_2(0){:}\,E_2(\delta r_2){:}\,E_2(n\delta r_2)] \tag{163}$$

the above summation reduces to the matrix equation

$$\boldsymbol{E}_2 = \frac{\delta z}{i\lambda} \widehat{\boldsymbol{K}}[\boldsymbol{r}_1 \cdot \boldsymbol{E}_1] \tag{164}$$

Here the matrix $\widehat{\boldsymbol{K}}$ is dependent only on the arrays $\boldsymbol{r}_1$ and $\boldsymbol{r}_2$, the wavenumber k, and the incremental spacing *dz.* It is independent of the envelope and wavefront of the incident electric field. In particular, for $\boldsymbol{r}_1 = \boldsymbol{r}_2$, $\widehat{\boldsymbol{K}}$ will be a square matrix. Thus for a numerical grid of constant size and spacing, the matrix $\widehat{\boldsymbol{K}}$ need only be solved once for a given wavelength. Once $\widehat{\boldsymbol{K}}$ is known, diffraction can be repeatedly evaluated using the Equation 164 with no need to re-evaluate $\widehat{\boldsymbol{K}}$.

A simple Rayleigh-Sommerfeld model of filamentation was implemented as follows. First, the appropriate matrices $\widehat{\boldsymbol{K}}$ where generated by substituting the appropriate grid sizes, the longitudinal spacings *dz*, and the laser center wavelength $\lambda = 800\, nm$ into Equation 159. A Gaussian beam modified by the phase lag of a spherical lens was taken as the input. The diffraction of the incident beam was then evaluated through iterative multiplications of the matrix $\widehat{\boldsymbol{K}}$. Between each iteration, the phase lag resulting from the Kerr effect and plasma defocusing for an interval *dz* was applied to the wavefront.

The Kerr effect was evaluated by calculating the radially resolved irradiance of the beam during each iteration of the diffraction code, and using it along with a value for the Kerr index in air of $n_2 = 3 \cdot 10^{-19}\, cm^2/W = 3\, \mu m^2\, /\, TW$ taken from literature [28] [29] to solve Equation 108. To evaluate plasma defocusing, plasma density was calculated from equations 148 and 149. The resulting values were then used in Equation 150 to calculate the resulting refractive index reduction.

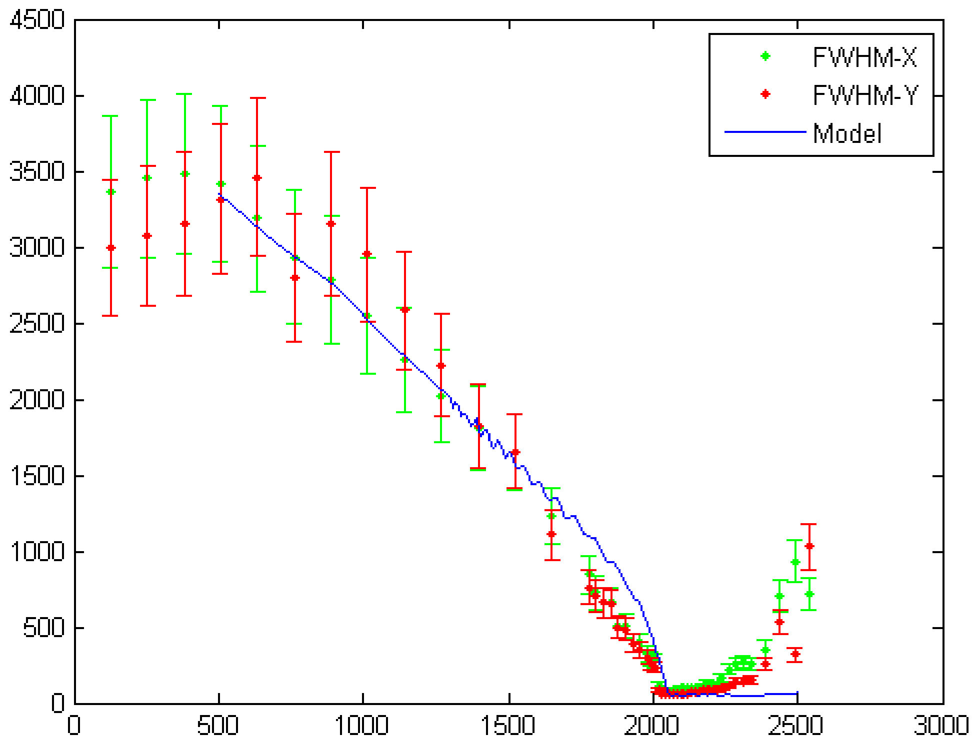

Figure 21: Filament beam waist as a function of propagation distance, as obtain from the Rayleigh-Sommerfeld model and experiment.

To evaluate the effectiveness of the model, it was compared against experimental measurements carried out by Khan Lim. A laser filament was obtained by focusing a 5.3 *mJ*, 50 *fs*, 800 *nm* ultrafast pulses through a 2 *m* lens. Similar settings were used within the simulation. The beam waist as a function of propagation distance for experiment and simulation is shown in Figure 21. For the experiment, the beam waist is evaluated along the two orthogonal axis of the camera used to record the image of the filament.

For the first 150 *cm* propagation, the beam waist obtained from simulation matches that obtained from the y-axis camera measurements. The simulation does overestimate the beam waist between 150 and 200 *cm* of propagation, but accurately predicts the point of optical collapse at 2 *m*. The simulation also predicts stable propagation of the filament over 1 *m*, but without incorporating a mechanism of energy loss, it currently cannot predict the end of the filament.

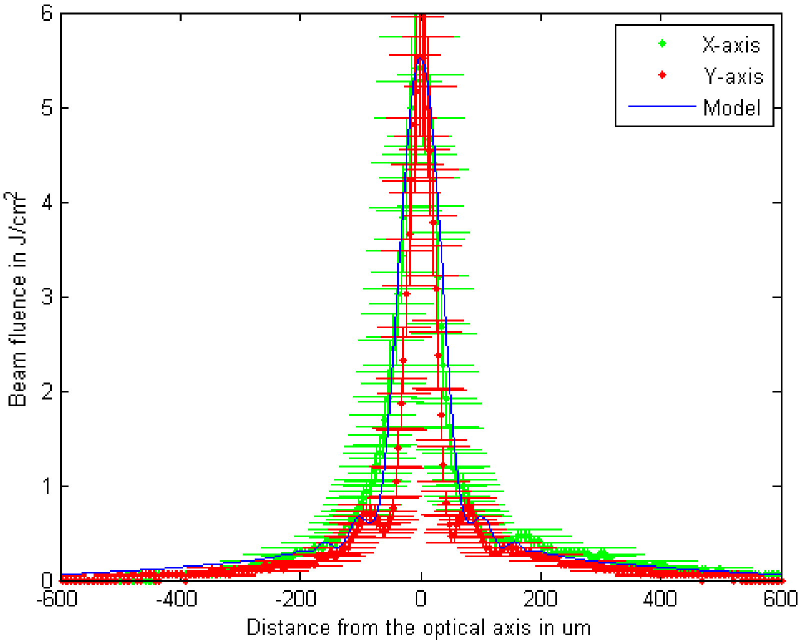

Figure 22: Transverse beam profiles obtained from simulation and experiment at the beginning of the filament.

The beam transverse profile obtained from simulation was also compared to experiment. Experimental beam profiles were recorded 2 *m* from the lens. The results along with the profile obtained from the model are shown in Figure 22. An excellent agreement is obtained between the simulated and experimental pulse envelope, particularly between the simulation and camera x-axis.

This original approach to simulation, while limited because of the relatively simplistic underlying modeling assumptions, is able to accurately model the early stages of filamentation. It illustrates the application of a Bessel beam basis to evaluate laser filamentation.

4.7 Helical Filaments

To improve both the experimental and practical implementations of laser filamentation in air, improved control of filamentation in general and multiple filamentation in particular is required. A simple and frequently employed means of controlling filaments is the use of converging lenses, which are used both to control the location and distance at which filamentation occurs. However, lenses offer limited control once pulse energy is sufficient to induce multiple filamentation, where the relative orientation of the filaments and in many cases even the number of filaments are no longer under the experimenter's control.

The synthesis of helical beams in Chapter 3 illustrated that in the linear case, the position, size and orientation of multiple irradiance spots can be controlled over extended propagation distance through the application of non-diffracting beams. Furthermore, the beam synthesis techniques were suitable for both continuous and pulsed beams, so the optical setup used in helical beam synthesis can readily be adapted to pulsed beams of instantaneous power in excess of the critical power required for filamentation.

Ionizing Bessel channels have already been experimentally produced in several recent experiments by illuminating an axicon with laser pulses possessing peak powers in excess of the critical power for filamentation in air [104] [105] [106] [107]. Filaments have also been obtained using ultrafast Airy pulses, where the transverse acceleration obtained with ordinary Airy beams was also observed for the filamenting structure and plasma channel present at the filament core [108] [109]. Generating ionizing helical channels using pulses of sufficient energy in conjunction with helical beam synthesis optics is a logical extension of these results, and has been carried out with some degree of success.

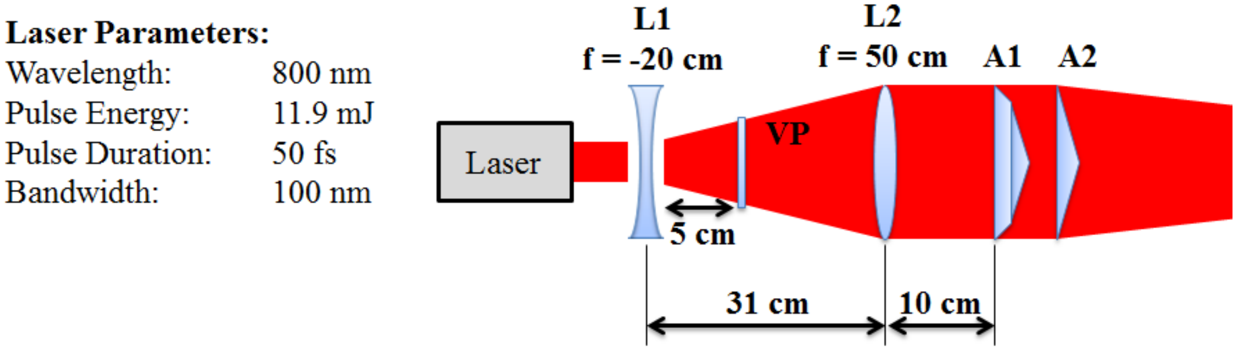

Figure 23: Experimental Setup

To generate helical filaments, pulsed helical beams were produced using $12.9 \pm 0.3\ mJ$, $50\ fs$ laser pulses from MTFL. Helical beams were synthesized from these pulses using the optical setup depicted in Figure 23, consisting of a vortex plate, a double angle axicon, and a conventional axicon placed in series along the laser propagation axis. The coaxial vortex plate was composed of an inner vortex plate $5\ mm$ in diameter that induced a unit azimuthal charge onto an $800\ nm$ beam, and a surrounding $10\ mm$ diameter phase plate the induced that the opposite azimuthal charge on the beam. The custom axicon featured two separate cone angles. Within the inner diameter of $12.7\ mm$, the axicon refracted light at an angle of $0.10°$, while light outside this diameter was refracted at 0.28°. The conventional axicon had an apex angle of 179.4° corresponding to a refraction angle of approximately 0.15°.

A telescope was used to match the transverse scales of the laser beam, axicons and vortex plate in a manner suitable for helical beam generation. The telescope was composed of a -200 *mm* and 500 *mm* focal length lens separated 310 *mm* apart to expand the incident laser pulse by a factor of 2.5. The coaxial vortex plate was located 50 *mm* behind the -200 *mm* lens, which resulted in the radial expansion of its phase pattern within the telescope. The custom axicon was placed 100 *mm* behind the telescope, and the conventional axicon 70 *mm* behind the custom axicon. Both the coaxial vortex plates and the custom axicon were mounted on 2-axis translation stages, enabling precise transverse alignment between both axicons and the phase plates.

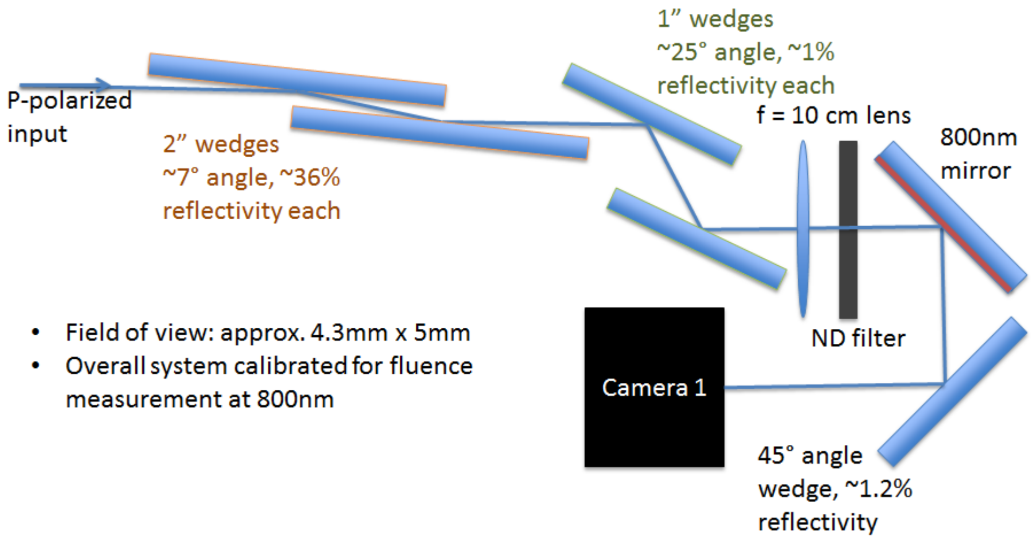

Figure 24: Optical setup used to record transverse images of high peak power and filamenting ultrafast pulses.

Transverse images were recorded with a calibrated optical apparatus designed by Khan Lim which is depicted in Figure 23 and Figure 24. This system was designed to record the beam profiles of high energy ultrafast pulses and laser filaments. The imaging apparatus employed four grazing incident wedges aligned in series for pulse energy reduction. A set of calibrated, interchangeable neutral density filters was located behind the wedges. A spherical lens located in front of the neutral density filters was placed to image the surface of the first wedge onto a CCD camera, which was used to record the image.

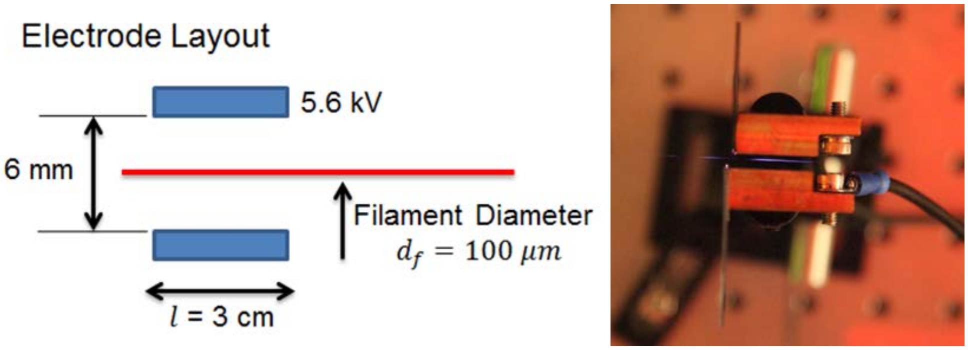

Figure 25: Layout and dimensions of the electrodes used to evaluate filament plasma density.

Ionization resulting from the helical beam was measured using a pair of 20 mm x 25 mm copper electrodes shown in Figure 25. The electrodes were spaced 6 mm apart, and raised to a potential of 5.6 kV $\pm$ 0.2 kV using the driver circuit shown in Figure 26. An oscilloscope, buffered using protective circuitry shown in Figure 27, monitored the voltage drop across a 6 $M\Omega$ resistor placed in series with the cathode.

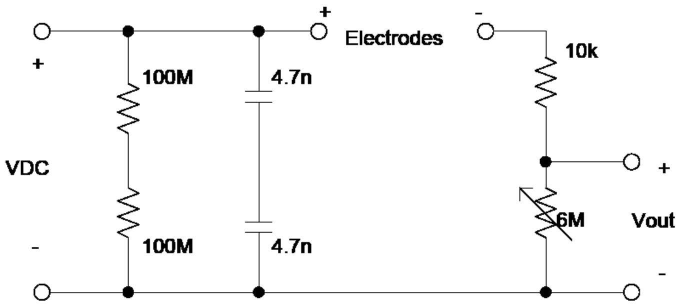

Figure 26: Electrode driving circuit. High-voltage is applied across VDC. Signal is measured by monitoring the voltage drop across the variable resistor.

Two experiments were carried out using the aforementioned experimental setup. Helical beams were first generated with 133 $\mu J \pm 4\ \mu J$ pulses to evaluate the performance of the synthesis optics in the absence of nonlinear effects, and to eliminate the optical setup as a cause of failure in the event that ionizing helical beams could not be obtained. Using the imaging apparatus, the transverse profile of the beams were recorded at incremental distances from the helical beam synthesizer, providing both beam rotation and beam fluence measurements as a function of distance.

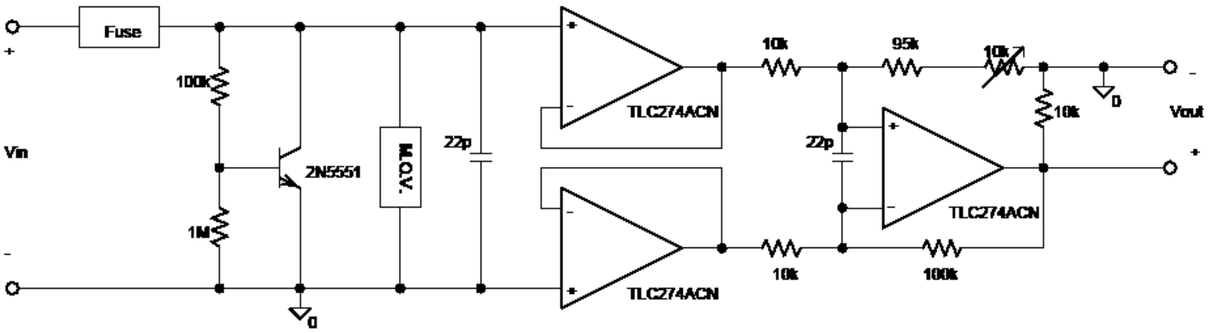

Figure 27: Protection and amplification circuit used to evaluate the voltage drop obtained from the electrode driver circuit.

Once helical beam synthesis was verified at 133 μJ, the experiment was repeated using pulse energies of $11.9 \pm 0.3\ mJ$, which possess ten times the critical power for filamentation in air. Transverse images were again recorded as a function of propagation distance. In addition, ionization measurements were carried out by evaluating the current passing through the copper electrode pair at incremental distances along the optical axis, with ten discharge current measurements recorded at each point.

For both experiments, helical beams were obtained. The helical beams extended from 883 *mm* to 1148 *mm* as measured from the end of the helical beam synthesizer. The helical beams underwent an approximately constant rate of rotation during propagation between these points of observation.

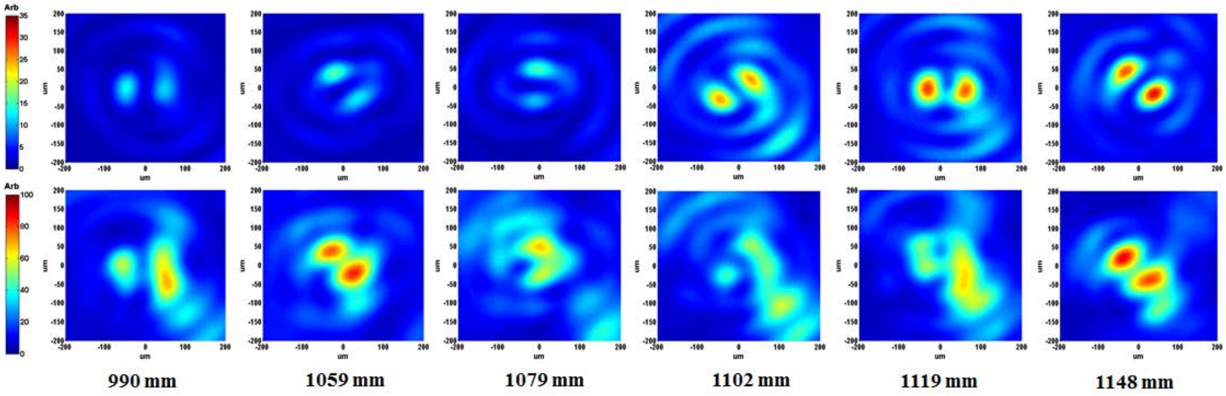

Figure 28: Helical beam transverse profiles as a function of propagation distance. Helical beams generated using 133 uJ pulses are shown in the upper figure associated with each distance, those obtained using 11.9 mJ pulses are shown in the lower figures.

The helical beam transverse profiles taken over the interval of observation are shown in Figure 28. For 133 μJ pulses, a helical beam composed of two isolated, rotating, elliptical spots is obtained in every recorded transverse image. When pulse energy is increased, a considerably greater fluence relative to the peak fluence is found between the irradiance peaks. In addition, for many of the transverse images taken of 11.9 *mJ* helical pulses, one or both of the irradiance peaks undergoes geometric distortions, losing the elliptical shaped observed for 133 μJ.

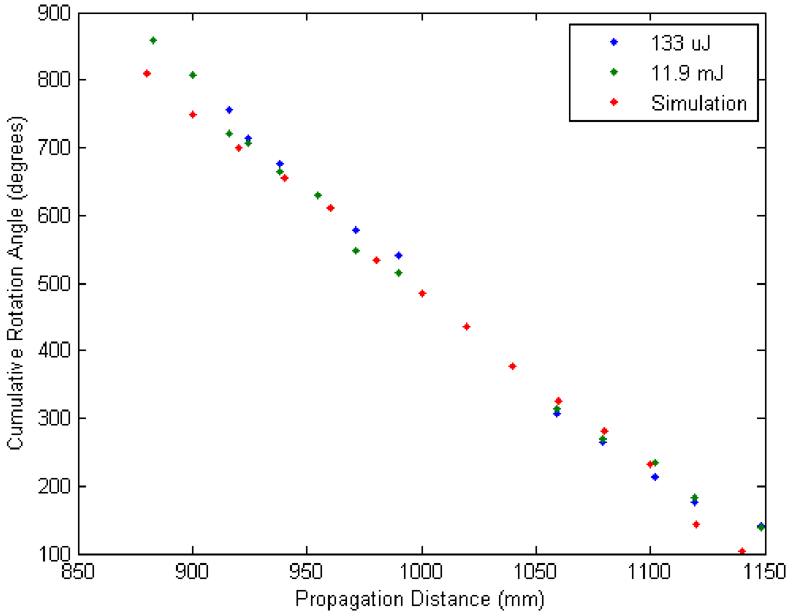

Figure 29: Helical beam cumulative rotation angle as a function of propagation distance.

The angles of both helical beams were recorded as a function propagation distance and compared with simulation, using the description of the rotation angle as illustrated in Figure 20. To better model the axicons in the simulation, thickness measurements were taken using a Zygo microscope, and the resulting data used to calculate the phase lag in the simulation. The beam rotation angle calculated from experiment and from simulation is shown in Figure 29. The values found for each of the cases fell within 60° relative to each other over the distance for which the helical beam was observed. The angles in all three datasets were also found to vary linearly with propagation distance, consistent with the description developed in Chapter 3.

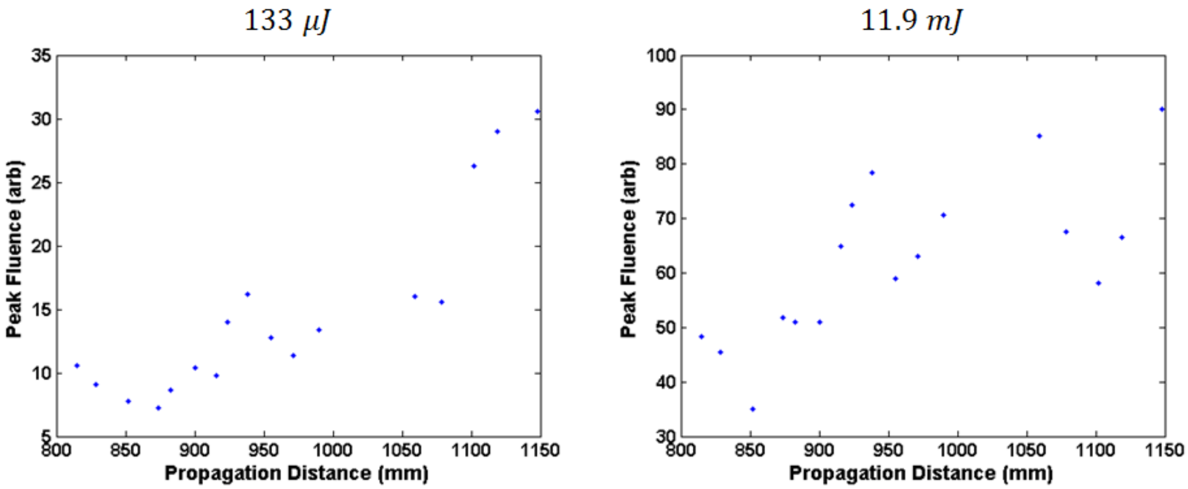

$133\ \mu J$

$11.9\ mJ$

Figure 30: Fluence as a function of propagation distance, both both 133 uJ pulses (left) and 11.9 mJ pulses (right). Both plots share the same scale.

Beam peak fluence was obtained from the transverse beam profiles, and is plotted as a function of propagation distance for both 133 μJ and 11.9 mJ as shown in Figure 30. Beam peak fluence obtained at 11.9 mJ was on average five times greater than that obtained at 133 μJ, despite the two order of magnitude difference between the two pulse energies used. This suggests the energy clamping mechanism well known in filamentation is in effect [85].

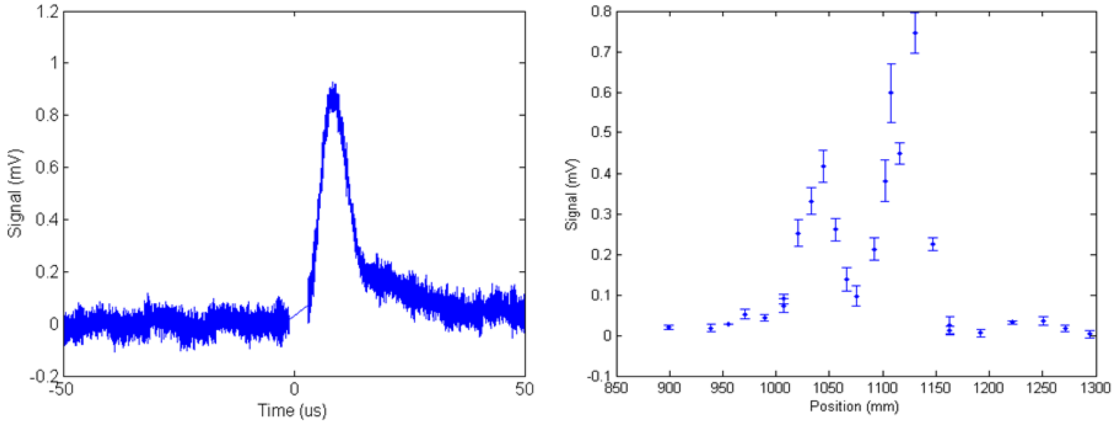

Figure 31: Ionization signal strength as a function of beam propagation distance. A typical ionization signal is shown on the left, while aggregate data is shown on the right.

Ionization caused by the pulsed helical beams was observed on the oscilloscope as millivolt level, 17 μs pulses which occurred a few microseconds after the laser trigger pulse. The recorded pulses were filtered using a 1-2-4-2-1 algorithm and the resulting signal averaged over 17 μs to obtain an amplitude representation of each measurements. These results were then averaged over the 10 samples recorded at each point, and the standard deviation was taken as the error. The results are plotted in Figure 31.

From Figure 31, the laser pulses are observed to undergo ionization between 1000 and 1150 *mm* from the helical beam synthesizer. This ionization coincides with the second half of the observed helical beam, indicating that the helical beam underwent ionization, but only after propagating 120 *mm*. The greatest distortions in the helical beam that occur when pulse energy is increased from 133 μJ to 11.9 *mJ* are observed at 1102 *mm* and 1119 *mm*, within the largest peak of the ionization signal, indicating that the resulting air plasma may be responsible for observed distortions in the helical beam.

Figure 32: Nitrogen fluorescence obtained when a telescope with a 40 cm equivalent focal length was used in conjunction with the helical beam synthesizer. Two longitudinally separate ionization peaks can clearly be observed.

The data in Figure 31 features two longitudinally separated ionization peaks. These features were also be observed as nitrogen fluorescence when the telescope used in the experimental setup was replaced with a telescope with a 40 *cm* equivalent focal length, which enabled peak irradiances sufficient for the observation of visible fluorescence, as shown in Figure 32. Two clear, isolated visible fluorescence peaks can be observed in Figure 32, consistent with the peak observed in the ionization data.

Helical filaments were successfully generated, as can be confirmed from the observation of both beam ionization and irradiance clamping when the helical beam was driven by a 13 *mJ*, 50 *fs* pulse. The beam profile of the helical beam was significantly distorted when undergoing filamentation, which may be a consequence of synthesizing a beam spot which is smaller than that which would have been obtained from filamentation without preparation. The use of a helical beam with a larger transverse scale may avert the problem of beam distortion during filamentation. Despite the beam distortion, the experiment demonstrates filaments can be guided along a helical path using a non-diffracting beam.

CHAPTER 5: REMOTE GENERATION OF RF RADIATION USING FILAMENTS

The remote generation of radiation represents a new paradigm for the delivery of electromagnetic radiation. In contrast to conventional means of delivering radiant energy, where energy is required to propagate over extended distances before use, remote generation uses a laser driven transient source of radiation, typically a plasma, to generate radiant energy in the precise point in space where it is required.

Such remote sources of radiation have a range of applications, including the generation of remote white light sources of radiation for remote spectroscopy and the generation of remote radio frequency sources for use in remote sensing and ground penetrating radar [110] [17]. Due to the nature of the laser plasma typically used, such remote radiation sources are often suitable for the generation of electromagnetic radiation ranging in frequency from the RF spectrum to the ultraviolet spectrum [16] [111]. In the work presented here, investigation of such remote sources will be confined to the radio frequency spectrum.

The creation of a remote RF radiation source requires a means to generate and drive the transient radiation source. An ideal means of driving the source is to employ the laser filaments discussed in Chapter 4, which enable the delivery of confined ultrafast pulses over extended distances. Because of the presence of transient currents driven by the ponderomotive force and other effects within the plasma found in the filament core, the laser filament provides a source of remotely generated RF radiation as it propagates through the atmosphere [112] [113]. However, the laser filaments themself prove to be highly inefficient sources of RF radiation, having conversion efficiencies on the order of 10^{-9} [114], unless additional methods are employed to enhance the resulting RF radiation [115]. If considerable RF power is required from the laser filament, a means other than the filamentation process in air is required to extract radio frequency radiation from laser filaments.

Alternatively, filaments can be used to irradiate solid matter. The irradiation of solid matter with ultrafast pulses has been shown to generate RF radiation both in vacuum [116] [117] and in air [111]. When matter is irradiated with low irradiance pulses, the irradiated surface will undergo melting and vaporization consistent with conventional heating. However, for femtosecond pulses with field strengths in excess of 10^8 V/cm, dielectric breakdown is expected [118] based on extrapolation from 10 ps dielectric breakdown experiments.

For filaments possessing an irradiance $10^{13} - 10^{14}$ W/cm^2, the associated electric field is $(0.9 - 2.7) \cdot 10^8$ V/m, which falls along the predicted threshold of dielectric breakdown. Any successful effort to increase the on-axis irradiance beyond that obtained for an unaugmented filament will yield an irradiance in excess of the breakdown threshold. Should the breakdown threshold be exceeded, the high irradiance present in the core of the filament will convert the material surface directly from a solid to a plasma on a sub-picosecond timescale [119]. The plasma and electron density resulting from this process is far in excess of the 10^{16} W/cm^2 electron density obtained within the filament core, enabling the generation of transient currents far greater than those found within the filament core and consequently a far stronger radio frequency emissions.

RF radiation from filament-matter interaction can be further enhanced by using a lens to prepare the laser filament. In addition to improving shot to shot stability, a spherical lens will refract the peripheral field of a filament onto the optical axis at the lens focal plane, temporarily enhancing on-axis beam irradiances along with electron emission responsible for RF radiation. This can be used to ensure the peak electric field of the filament exceeds the breakdown threshold of irradiated solids.

5.1 RF Generation Model

The generation of RF radiation from laser solid interactions was modeled numerically using MATLAB. In the model, which is illustrated in Figure 33, incident laser radiation is assumed to ionize the surface of irradiated matter through a combination of multi-photon ionization and avalanche ionization, resulting in the generation of free electrons. The electrons were then assumed to stream directly away from the surface at the electron thermal velocity, until their momentum was arrested by collisions with neutral air molecules. This results in a short distance, transient current which acts as a broadband dipole radiator.

The electron dynamics resulting from laser-matter interaction can be expressed as a series of differential equations, which can be numerically solved using the Euler method. Before evaluating electron dynamics, the time and space resolved incident irradiance was determined. To obtain the irradiance, the incident laser pulse was assumed to be Gaussian in both space and time, and the pulse was assumed to be cylindrically symmetric. Departures from Gaussian behavior in space were accounted for using an above unity M^2 factor. Departures from Gaussian behavior in time, usually resulting from chirp, were accounted for by increasing the beam temporal pulse duration to match the temporal pulse broadening associated with the pulse chirp.

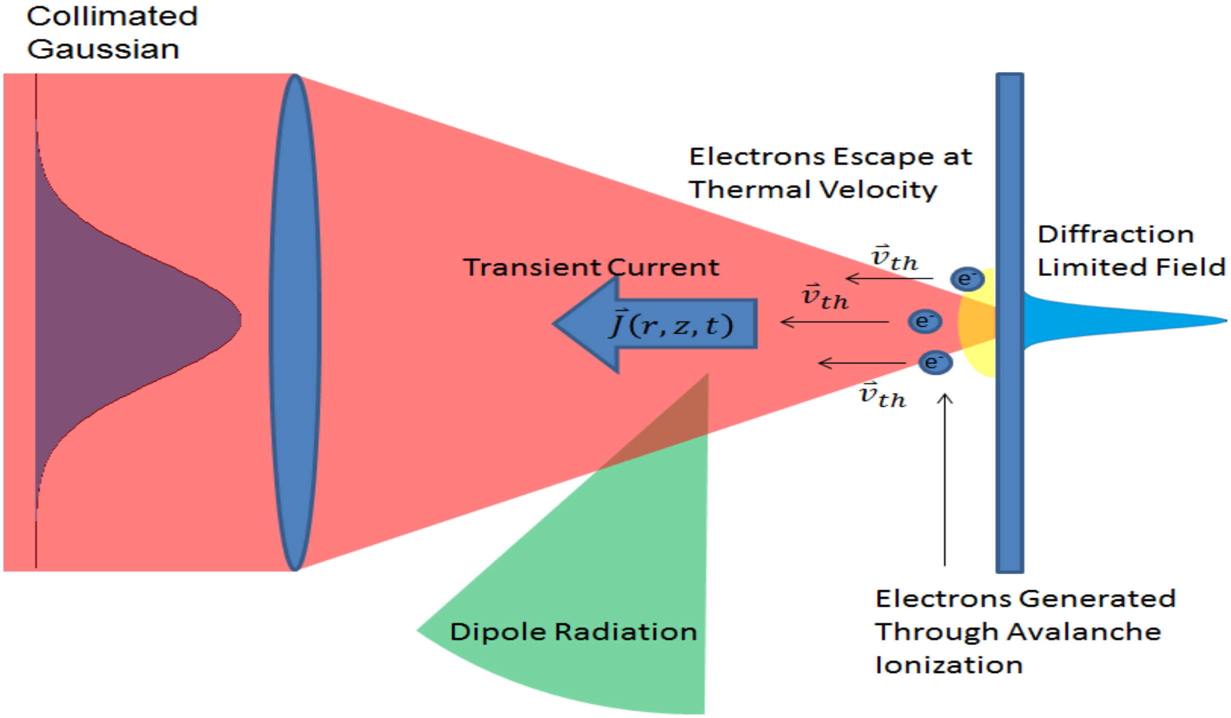

Figure 33: Illustrated summary of the model used to evaluate filament-matter induced RF radiation.

Laser pulses are experimentally characterized by the temporal pulse width, the spatial pulse width, and the pulse energy. To obtain the pulse irradiance, first instantaneous pulse power was obtained by integrating over the temporal pulse envelope and rearranging the result.

$$E_p = P_0 \int dt \exp\left(-\frac{t^2}{\tau^2}\right) = P_0 \tau \sqrt{\pi} \tag{165}$$

$$P_0 = \frac{E}{\tau\sqrt{\pi}} \tag{166}$$

$$P(t) = P_0 \exp\left(-\frac{t^2}{\tau^2}\right) \tag{167}$$

Here, E_p is the pulse energy, $P(t)$ is the instantaneous pulse power, P_0 is the peak instantaneous pulse power, and τ is the pulse duration. For the experiment being modeled, $E_p = 8\,mJ$, $\tau = 50\,fs$ and $M^2 = 1.7$.

Pulse irradiance is obtained from the time resolved pulse power, under the assumption that material surface lies in the focal plane of the lens used to focus the pulse energy onto the surface. Under these assumptions, the irradiance is described by an Airy disk

$$I(r,t) = I(t)\left[\frac{2J_1\left(\frac{\pi d r}{\lambda f}\right)}{\frac{\pi d r}{\lambda f}}\right]^2 \tag{168}$$

This irradiance profile can be approximated using the Gaussian

$$I(r,t) = I(t)\exp\left(-\frac{r^2}{2w^2}\right) \tag{169}$$

where

$$w = \frac{0.42\lambda f}{d} \tag{170}$$

To account for an above unit M^2 this expression is modified to

$$w = \frac{0.42\lambda f}{d} M^2 \tag{171}$$

Irradiance is then related to power through the integral

$$P(t) = 2\pi I(t) \int dr\, r \exp\left(-\frac{r^2}{2w^2}\right) = 2\pi w^2 I(t) \quad \textbf{(172)}$$

$$I(t) = \frac{P(t)}{2\pi w^2} \quad \textbf{(173)}$$

Combining this with the time domain expression from Equation 169 gives

$$I(r,t) = I_0 \exp\left(-\frac{r^2}{2w^2}\right) \exp\left(-\frac{t^2}{\tau^2}\right) \quad \textbf{(174)}$$

$$I_0 = \frac{E_p}{2\pi\tau w^2\sqrt{\pi}} \quad \textbf{(175)}$$

For laser pulses above the critical power of 3 GW, the pulse will undergo Kerr self-focusing even in the absence of a lens, resulting in a laser plasma filament. While the true transverse profile of a filament is Townesian, filaments can also be approximated using a Gaussian profile, using the same functional formed as listed above. However, unlike the above case, the beam waist and peak irradiance will be fixed by those parameters experimentally obtained for laser filaments from literature, namely

$$w = 50\ \mu m - 100\ \mu m \quad \textbf{(176)}$$

$$I_0 = 10^{13} - 10^{14}\ W/cm^2 \quad \textbf{(177)}$$

Filamentation is simulated by taking the maximum of the focused pulse profile and the filament profile and each point in space and time, essentially preventing the incident irradiance from falling below that defined for a filament.

Once the incident irradiance has been determined, electron temperature is calculated using the incident irradiance and electronic specific heat for the material in question. Because the physics under investigation takes place on a sub picosecond time scale, it is assumed there is insufficient time for energy transfer between the electrons and the material lattice. Therefore, the thermal dynamics of the electrons may be dealt with in isolation. To further simplify the problem, it is assumed that the conduction of heat away from the surface can be neglected on the femtosecond time scale, and that the laser power is all deposited within a single skin depth of the material. It is also assumed that no light is reflected from the material surface prior to the formation of plasma.

The surface electron temperature evolves according to [120]

$$\gamma T \frac{dT(r,t)}{dt} = \frac{I(r,t)}{d_s} \tag{178}$$

where γ is the electronic specific heat and d_s is the skin depth. For copper, $\gamma = 420 \frac{J}{kg \cdot K}$ [121] and $\gamma = 97.0\ \frac{J}{m^3 K^2}$ [122]. The skin depth can be obtained using

$$d_s = \frac{\lambda}{2\pi\kappa} \tag{179}$$

where κ is the extinction coefficient. For copper, $\kappa = 5.26$ [123], yielding a skin depth of $d_s = 24\ nm$.

The temperature is calculated by applying the Euler algorithm to the above differential equation using the irradiance profile given in Equation 174. The resulting temperature is resolved in both the radial and temporal dimensions. Specific temperature varies depending on time, focal length and radially location, but the peak temperature obtained for a 1 *m* focal length lens in the simulation was 250,000 *K* or 22 *eV*.

The electron thermal velocity is obtained from the electron temperature using

$$v_{th} = \sqrt{\frac{8k_B T}{\pi m_e}} \tag{180}$$

as provided by [123], which is assumed to be the velocity at which the electrons travel away from the material surface after ionization. Here k_B is Boltzmann's constant and m_e is the electron mass. As dictated by Equation 180, the thermal velocity corresponding to 250,000 K is $v_{th} = 3.1 \cdot 10^6 \frac{m}{s}$.

Most of the materials used in the generation of remote radio frequency radiation during experiments were metals. For metals, it is assumed that the material is initially in the ground state, and that the electrons are separated from their ionization state by an empty conduction band, and that the energy spacing between the electrons in their ground state and the top of the conduction band is the work function of the metal in question. For copper, a work function of 4.65 *eV*, taken from Eastman et al., is chosen [124] [125] [126] [122].

Incident laser radiation is assumed to ionize the metal through a combination of multiphoton and avalanche ionization, which move the electrons from the ground state to the ionization state. The time evolution on the free electron density due to these two processes is then described by [127]

$$\frac{dN}{dt} = \alpha I N + \sigma_k I^k \tag{181}$$

where α is the avalanche ionization coefficient and σ_k is the multiphoton ionization coefficient for k photon ionization.

For copper, values for the avalanche and multiphoton ionization coefficients could not be obtained. For 800 *nm* light, three photons of 1.55 *eV* are required to overcome the copper work function of 4.65 eV. This property was used to find another material with a similar bandgap to be used as a surrogate. Lenzer et al. provides the required coefficients for BBS glass, which has a bandgap requiring 3 photons to cross at 780 nm. These coefficients are $\alpha = 1.2\ \frac{cm^2}{J}$ and $\sigma_3 = 7 \cdot 10^{17}\ \frac{1}{ps \cdot cm^3}\left(\frac{cm^2}{TW}\right)^3$ [127], and were used in to simulate copper in the absence of copper specific data.

The total electron density that can be obtained through ionization is assumed to be limited by the critical electron density associated with the incident laser radiation. Once this value is exceeded, the plasma frequency of the free electrons exceeds that of the incident laser pulse, preventing additional radiation for reaching the material surface and acting as a clamping mechanism [118].

The electron plasma frequency is defined as

$$\omega_p = \sqrt{\frac{Ne^2}{\epsilon_0 m_e}} \tag{182}$$

From which the critical density can be obtained by setting the plasma frequency to the laser pulse center frequency and solving for the electron number density

$$N_c = \frac{\epsilon_0 m_e \omega^2}{e^2} = \frac{4\pi^2 m_e \epsilon_0 c^2}{\lambda^2 e^2} \tag{183}$$

For 800 *nm* light, the resulting critical density is $N_c = 1.75 \cdot 10^{21}\ cm^{-3}$.

The electron density solved using the ionization equations above are taken as a boundary condition, with the additional restriction that the resulting electron density may never exceed the critical electron density. During each logic cycle of the numerical simulation, ionized electrons are permitted to stream away from the material surface at the thermal velocity, to be replaced by electrons generated through ionization during the next cycle in the code. However, electrons generated during the previous cycle are still used to seed electrons in the following logic cycle.

Once electrons have escaped the material surface, they are assumed to travel at a velocity of v_{th} until they collide with an air molecule. At this point it is assumed all forward velocity is lost, so that electrons that have collided are no longer factored into the current that will be responsible for the dipole radiation predicted by the simulation. The dynamics for the collisional depopulation process are dictated by

$$\frac{dN}{dt} = -\nu N \tag{184}$$

where ν is the electron-neutral collision frequency in air defined by

$$\nu = \frac{v_{th}}{u} \tag{185}$$

and u is the electron mean-free path. For air at standard temperature and pressure, $u = 69\ nm$ [123].

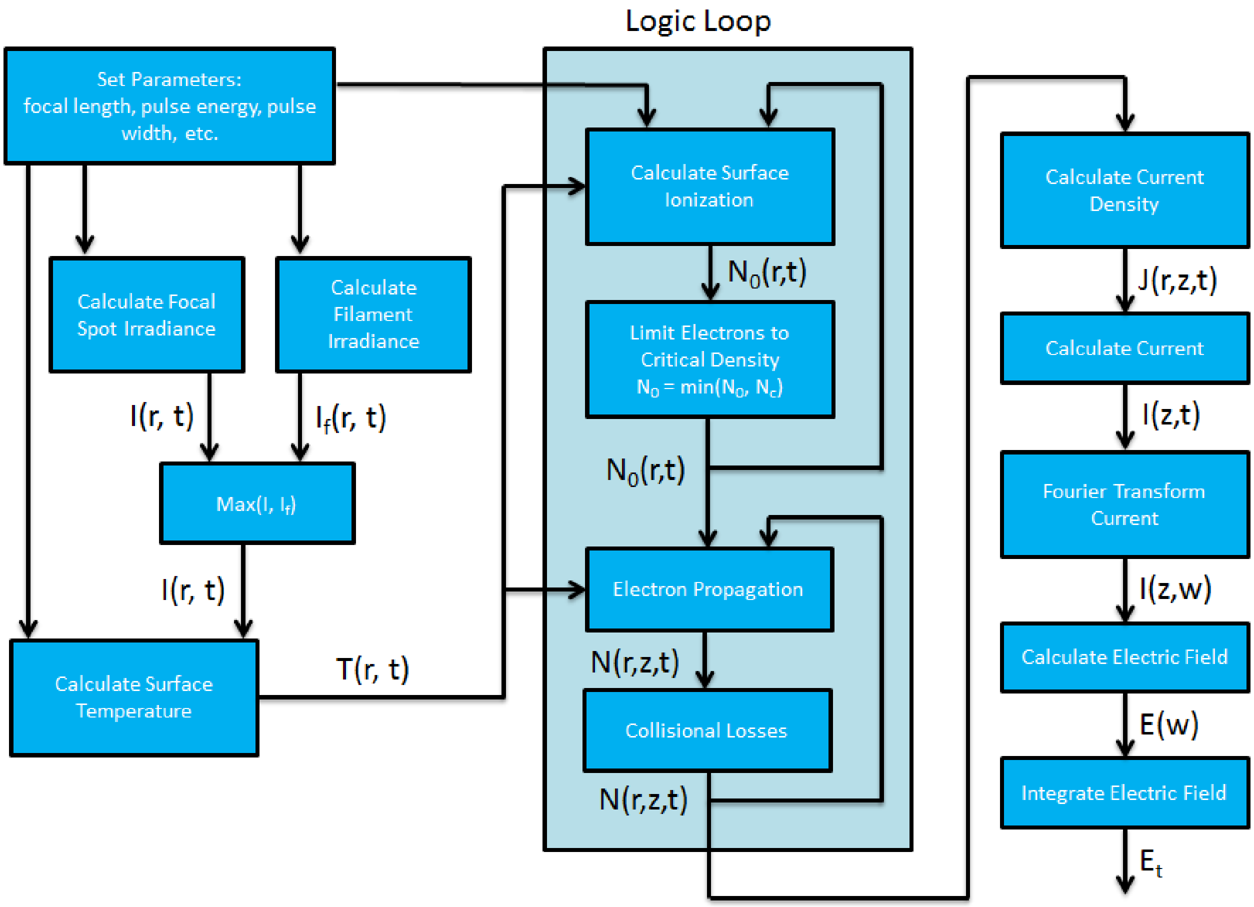

Figure 34: Code flow chart describing the filament matter induced RF radiation simulation.

The time and spaced resolved number density resulting from surface ionization, critical density saturation, electron propagation from the surface, and electron loss due to collisions is numerically calculated as part of a single, self-contained process, with the time and radially resolved incident irradiance and surface temperature treated as fixed constants for these calculations, as these values are obtained by the code prior to carrying out ionization calculations. Once the computations for the electron density values for all points in time and space are complete, the current density resulting from electron motion is obtained from

$$J(r,z,t) = ev_{th}N(r,z,t) \tag{186}$$

The total current can then be obtained by radially integrating over the current density

$$I(z,t) = \int dr\, r\, J(r,z,t) \tag{187}$$

As this current is directed away for the material surface and extends only a short distance, it can be treated as an infinitesimal dipole radiator. To treat the current using antenna theory formalism, it is taken to the Fourier domain

$$I(z,\omega) = \mathcal{F}[I(z,t)] \tag{188}$$

The radiated electric field spectrum is then calculated using the expression for an infinitesimal dipole

$$E(\omega,R,\theta) = \int dz \frac{\omega I(z,\omega)}{4\pi c\epsilon_0 R} \sin\theta \tag{189}$$

where R is the distance between the laser-matter interaction and the field point and θ is the angle between the field point and the surface normal. From the electric field spectrum, the integrated field strength is then obtained using Parseval's theorem

$$E_{tot}(R,\theta) = \sqrt{\int E^2(w,R,\theta)d\omega} \tag{190}$$

The integrated field strength is then evaluated as a function of lens focal length given in equations 170 and 171, by evaluating the entire series of equation listed in this section for each focal length of interest. These lens resolved RF field measurements can then be used as a benchmark for comparison against experiment.

5.2 RF Detection and Measurement

Given the duration of the laser pulses used to drive the plasma responsible for RF radiation, and the temporary duration of the resulting plasma, resulting RF radiation is expected to be short lived and broadband. For these reasons, single-shot, broadband measurements are required to evaluate the RF radiation. To carry out such measurements, a Tektronix CSA7404 was used, which is a single-shot oscilloscope with a 4 *GHz* bandwidth and 20 *GS/s* sample rate.

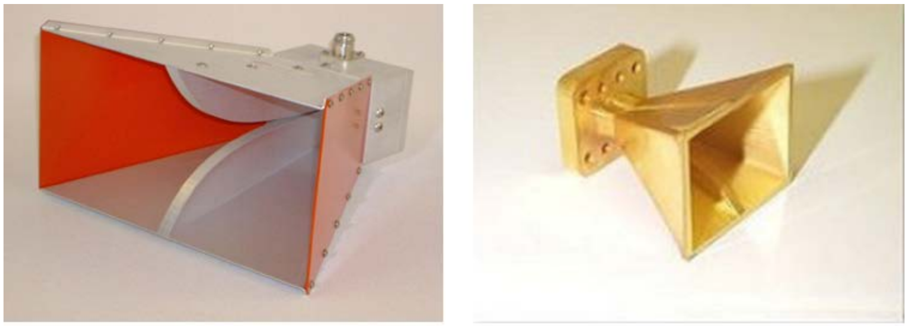
1-18 GHz

18-40 GHz

Figure 35: Horn antennas used in all RF experiments.

To extend the measurement range of the CSA7404, a custom built heterodyne receiver was used. The heterodyne receiver has a 4 *GHz* channel bandwidth to match both the bandwidth and time response of the oscilloscope, and a 1-40 *GHz* spectral range, providing the oscilloscope access to a spectral bandwidth 10 times that available unaided. A pair of polarization sensitive, broadband horn antennas, the 1-18 *GHz* Sunol Sciences DRH-118 and the 18-40 *GHz* Q-Par Angus QPS180K, were used to couple RF radiation from free space into the instrumentation.

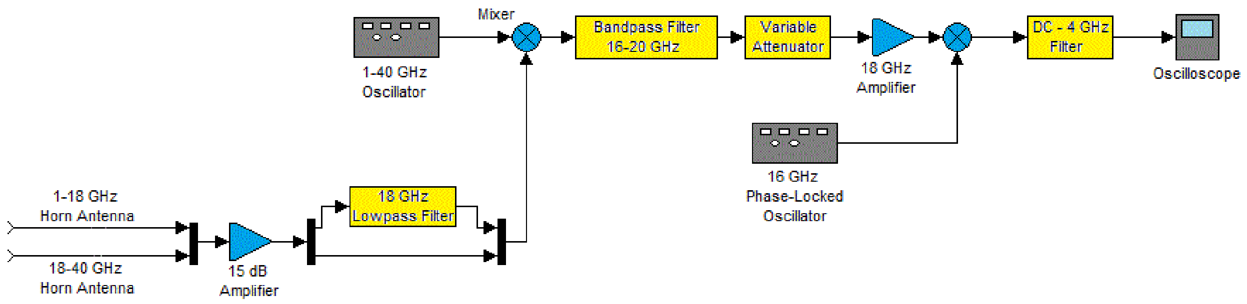

Figure 36: Heterodyne signal processing system used to evaluate RF radiation.

The heterodyne system layout is shown in Figure 36. The heterodyne receiver downconverts a continuous band of 4 *GHz* lying within the 1-40 *GHz* spectrum while simultaneously filtering frequencies lying outside the spectral range of interest. This is accomplished by first mixing the incoming signal with a 1-20 *GHz* carrier to shift the desired spectrum to 16-20 *GHz*. A bandpass filter is then used to reject frequencies lying outside this spectral range. The filtered signal is then amplified and mixed with a fixed 16 *GHz* carrier which shifts the remaining signal to 0-4 *GHz*, which is then analyzed using the CSA7404. A pre-amplifier is placed immediately after the horn antennas to increase system sensitivity and reduce the system noise figure.

The signal processing system was calibrated by performing spectrally resolved gain measurements with a known, tunable frequency source. Subsequent RF measurements were carried out in the time domain. To correct for the frequency response of the heterodyne receiver and the antennas, the measured RF signal is first converted to the frequency domain. This was done using either an internal Fourier transform function on the oscilloscope, or by carrying a fast-Fourier transform within MATLAB. Signals obtained from the system were then corrected using the resulting gain spectrum, by subtracting the gain spectrum from the signal spectrum using MATLAB code.

The spectrum of the incident field is obtained from the measured spectrum using antenna theory. The irradiance of the electromagnetic field is related to the measured power through

$$I(\omega) = \frac{P(\omega)}{A_e(\omega)} \tag{191}$$

where I is the spectrally resolved irradiance, P is the spectrally resolved cable power, and A_e is the antenna effective area given by

$$A_e(\omega) = \frac{\lambda^2}{4\pi} G(\omega) \tag{192}$$

provided the antenna is properly aligned [128]. Here G is the antenna gain, which is a function of frequency. Manufacturer provided values of the gain were used to obtain the antenna effective area. The incident electric field is then obtained from the measured irradiance using the Poynting relation

$$\left|\vec{E}\right| = \sqrt{\frac{2I}{c\epsilon_0}} \tag{193}$$

To evaluate the total energy associated with a given RF pulse, Parseval's theorem was used to evaluate the total irradiance contained within the spectrum [129]. The above equation was also applied to obtain the integrated electric field, which is the peak electric field of a time-bandwidth limited pulse possessing the irradiance and bandwidth of the measured field.

5.3 Terawatt Filament Experiments

The first set of experiments was conducted using the TW laser system. These were performed jointly by the present author and Dr. Robert Bernath. Pulses with energy of 8 *mJ* generated from TW were used to irradiate planar targets composed of copper, aluminum, polyformaldehyde, fused silica and sapphire. Pulses from TW were turned into the 50 *m* laser range, and permitted to propagate 30 *m* before reaching a spherical lens. The targets under investigation were placed within the focal plane of the lens and their surfaces aligned to be normal relative to the laser propagation axis. Laser self-filamentation was observed during beam propagation, and was found to prevent diffraction from increasing the laser spot size before the lens was reached.

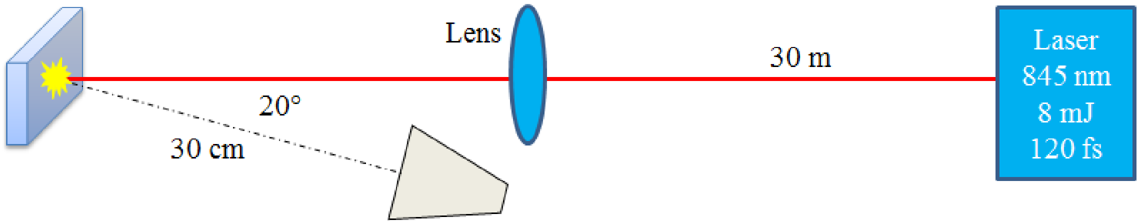

Figure 37: Experimental setup used to evaluate filament induced RF radiation in the Terawatt experiments.

The 1-18 *GHz* horn antenna was placed 30 cm from the target, at an angle 20° relative to the target surface normal, as shown in Figure 37. The antenna was oriented for both horizontal and vertical polarization measurements. Data was collected by firing a single laser pulse onto the target through the setup while the CSA7404 monitored data using a trigger synchronized to the laser. For each material, the experiment was repeated using several different mixing configurations on the heterodyne receiver, until sufficient data was obtained to reconstruct a 1-18 GHz spectrum.

For all the materials investigated, the interaction of laser filaments with the material surface resulted in short RF pulses, as shown Figure 38. These pulses possessed subnanosecond rise times and 2-20 *ns* fall times. The large disparity between the observed rise and fall times may be due to cable ring or similar parasitic oscillations in the detection system extending the pulse trailing edge, suggesting the observed RF pulses are a combination of an RF impulse followed by a tail formed by ringing.

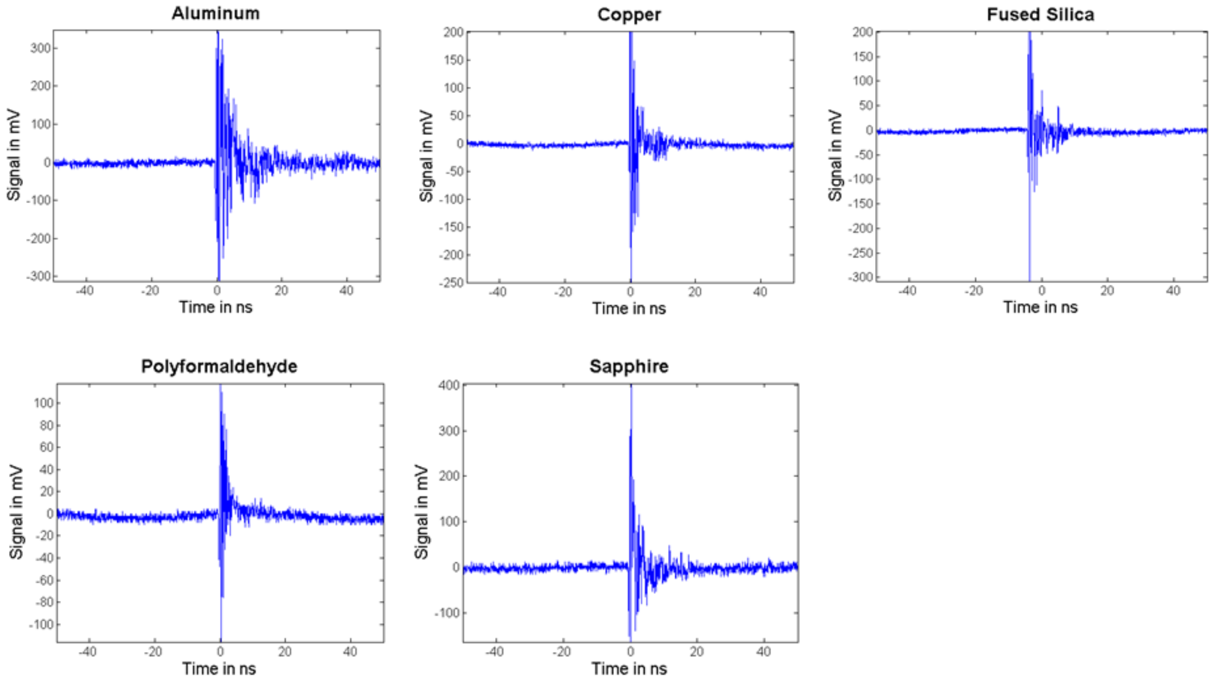

Figure 38: Raw oscilloscope traces.

The spectrum of the measured signals was obtained by carrying out a fast-Fourier transform using internal oscilloscope math functions. The spectra obtained for the five materials investigated are shown in Figure 39 for horizontal polarization and Figure 40 for vertical polarizations. The RF spectra for all materials extended from 4 *GHz* or less to 18 *GHz*, the upper frequency limit of the measurements, for both polarizations. Some materials, such as copper, polyformaldehyde and sapphire have weak spectral components that extend down to 1 *GHz*, filling the whole spectra range under investigation. For all materials, the measured spectrum does not converge to zero at the upper measurement limit of 18 *GHz*, indicating that the actual spectrum extends beyond this frequency.

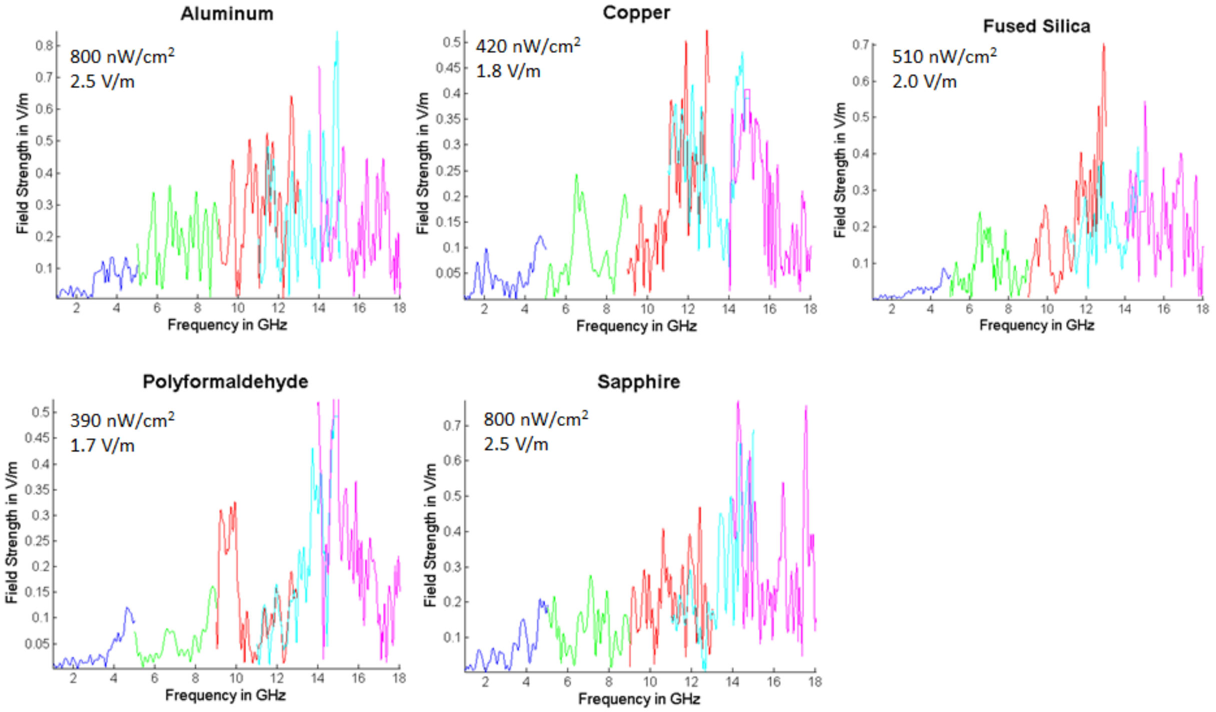

Figure 39: Spectral measurements of laser-matter induced RF radiation, conducted using a horizontally polarized antenna.

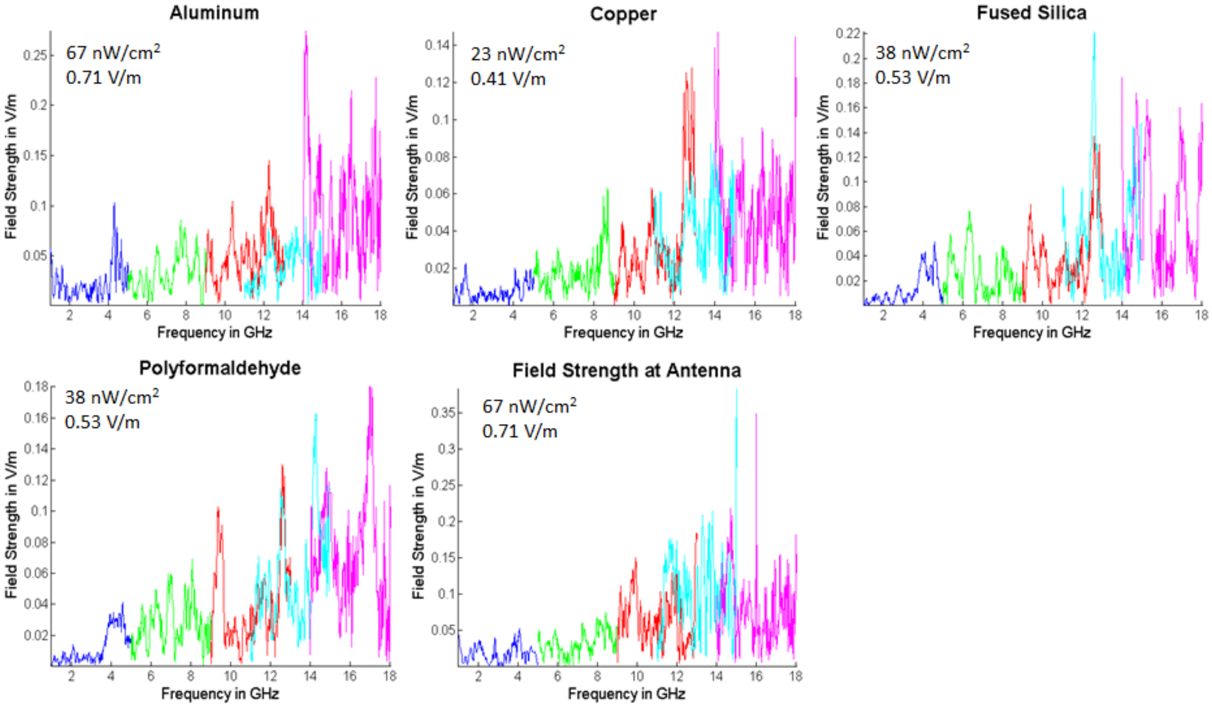

Figure 40: Spectral measurements of laser-matter induced RF radiation, conducted using a vertically polarized antenna.

Strong polarization dependence was observed from the data. On average, signals obtained when the antenna was horizontally aligned possessed irradiances an order of magnitude greater than those obtained for vertical polarizations. This polarization response is consistent with an infinitesimal dipole radiator aligned along the beam propagation axis, for which a horizontally polarized antenna would be polarization matched while a vertically aligned antenna would be cross polarized.

5.4 High Frequency Experiments

RF emissions were also evaluated within the 18-40 *GHz* range. Aluminum, copper and delron were irradiated by reflecting 50 *fs*, $11.8 \pm 0.4\, mJ$ pulses from MTFL off a long focal length concave mirror located 9 *m* from the target. Laser filamentation began 3 *m* from the mirror. The laser pulse propagated over the remaining 6 *m* as a filament before irradiating the target surface. The target surface was always aligned normal to the incident laser pulse.

The experimental setup is shown in Figure 41. RF radiation was measured using the QPS180K horn antenna, which was aligned to and located 10 *cm* from the irradiated surface. The antenna was oriented at angles of 10^o, 45^o, and 90^o relative to the surface normal in the horizontal plane, and also place directly above the target, maintaining its 10 *cm* distance from the irradiated surface, to obtain angularly resolved RF measurements. For each orientation, measurements were taken using both antenna polarizations, obtained by 90^o rotations of the antenna, and for both laser polarizations, obtained using a quarter-wave plate, to determine laser and field polarization dependence of the RF radiation.

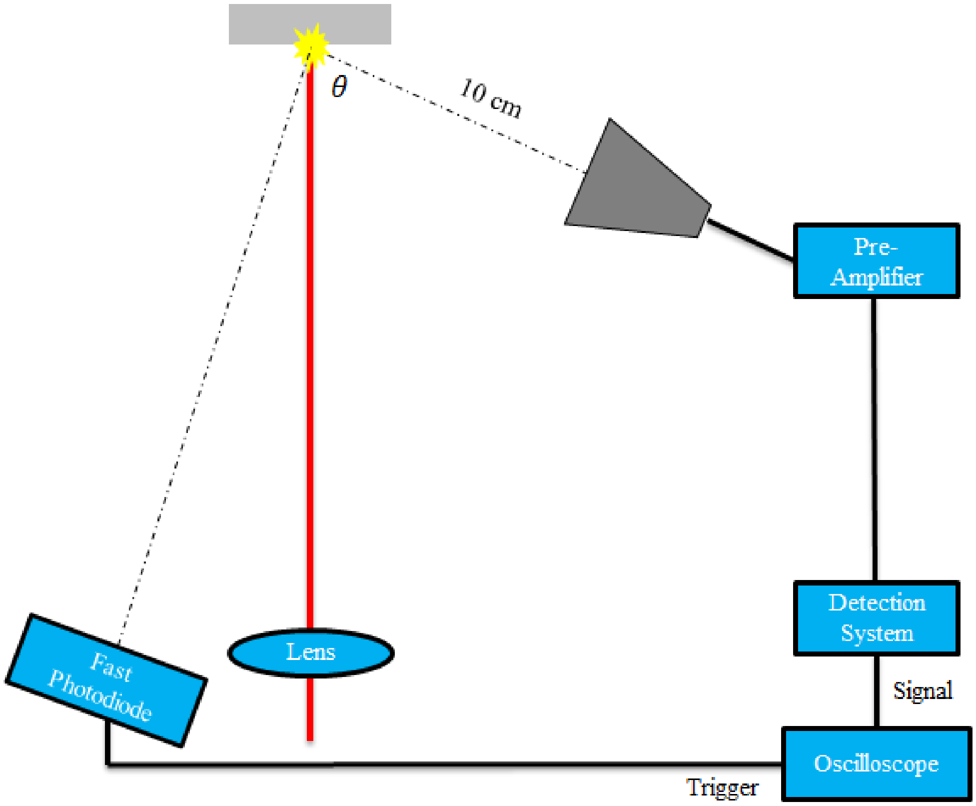

Figure 41: Experimental setup used to evaluate 21-35 GHz laser filament induced RF radiation.

The heterodyne detector and oscilloscope were synchronized to the incident laser pulses by triggering off a fast photodiode monitoring the visible light that resulted from the plasma which formed on the target surface. The oscilloscopes internal math function was used to record the resulting RF spectra. To obtain an RF background, a beam block was used to prevent the filament from reaching the target, and the RF spectra for each experimental configuration were recorded under these conditions.

For the above experimental conditions, RF spectra proved to be weak, with a signal to noise ratio only marginally greater than one. In the case of Delron, no spectra could be observed other than the background, and the resulting RF signal was concluded to be below the detection threshold of the equipment. Spectra were obtained for both aluminum and copper.

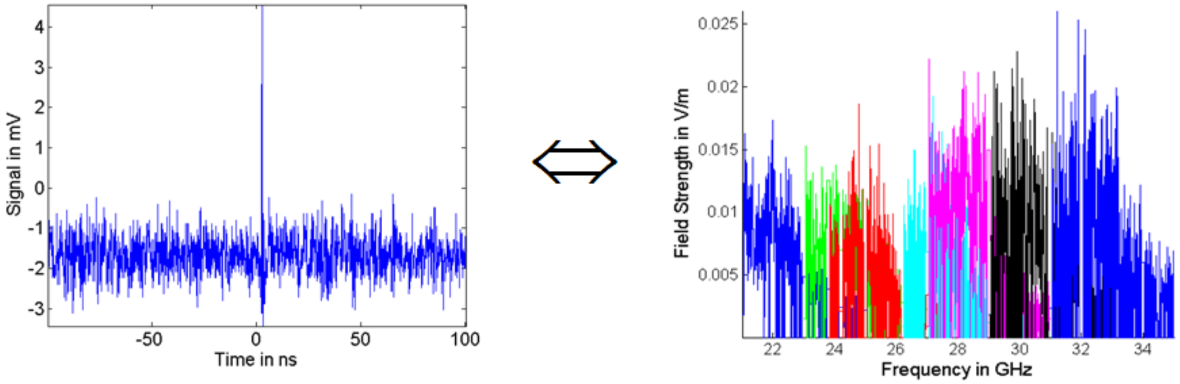

Figure 42: Sample time domain measurement of filament induced RF radiation and corresponding spectra.

A time domain image and corresponding compiled spectrum is shown in Figure 42. The time domain plot is characteristic of all RF signals above the detection threshold of the measurement system. All such pulses were sub-nanosecond in duration and limited to the bandwidth of the instrumentation. This indicates the duration of the measured RF pulses are shorter than the band limited response of the oscilloscope of 250 *ps*, and have a coherent spectrum in excess of 14 *GHz*. The measured spectra corresponding to the RF pulses are relatively uniform and extend across all measured frequencies, suggesting that the true spectrum extends beyond the 21-35 *GHz* frequency range evaluated in this experiment.

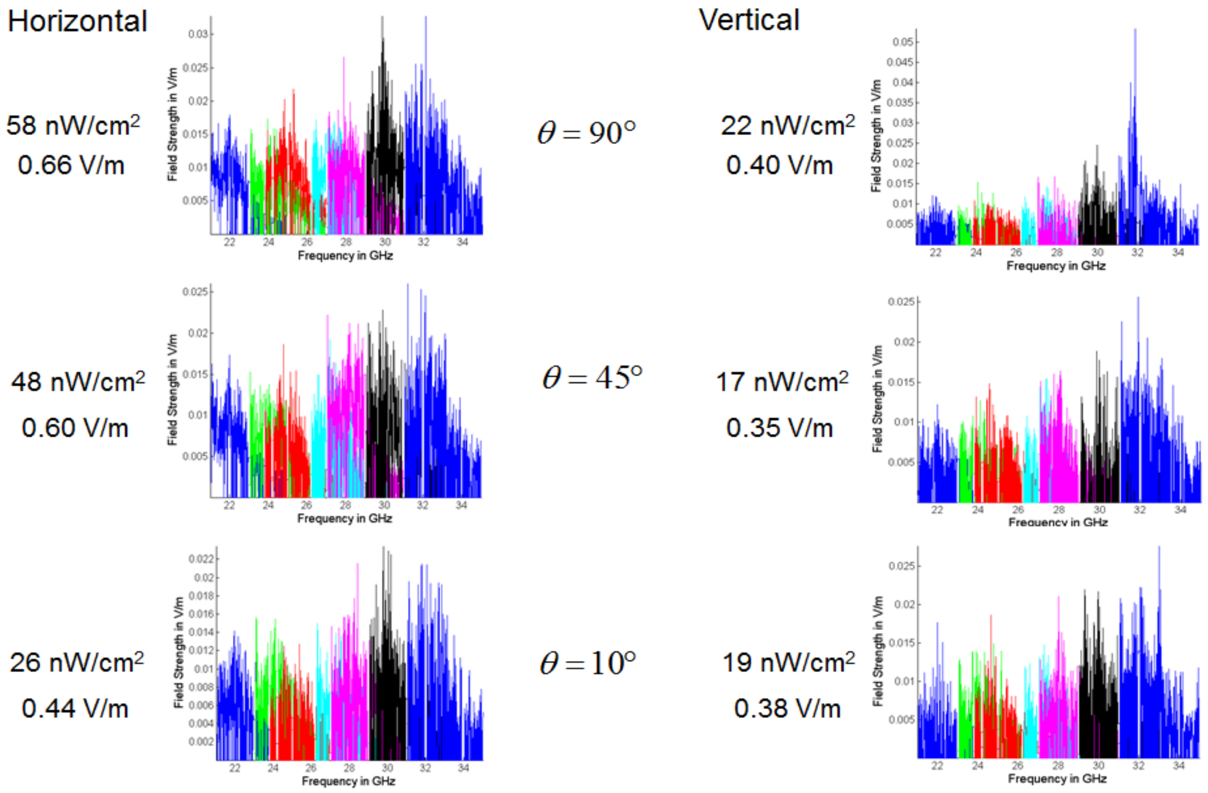

Figure 43: Filament induced RF radiation evaluated at several orientations relative to the surface normal for irradiated copper.

Rudimentary radiation pattern measurements were carried out by evaluating the filament induced RF radiation at three separate angles relative to the surface normal within the horizontal plane. For each angle, measurements were carried out with the antenna both horizontally and vertically aligned, and using both horizontal and vertically polarized laser light. The resulting spectra obtained from these measurements along with total irradiance and field strength obtained from the spectra which are shown in Figure 43. For horizontal polarizations, a clear angular dependence is observed, with maximum radiated power obtained at 90° relative to the surface normal. For vertical polarizations, the total field irradiance was both independent of angle and weaker than the field irradiance obtained for horizontal polarization at any angle. This leads to the conclusion that the FIRF obtained from copper is horizontally polarized, with an antenna pattern which peaks at 90° relative to the surface normal and approaches the background value observed for vertical polarizations as the angle relative to the surface normal approaches zero.

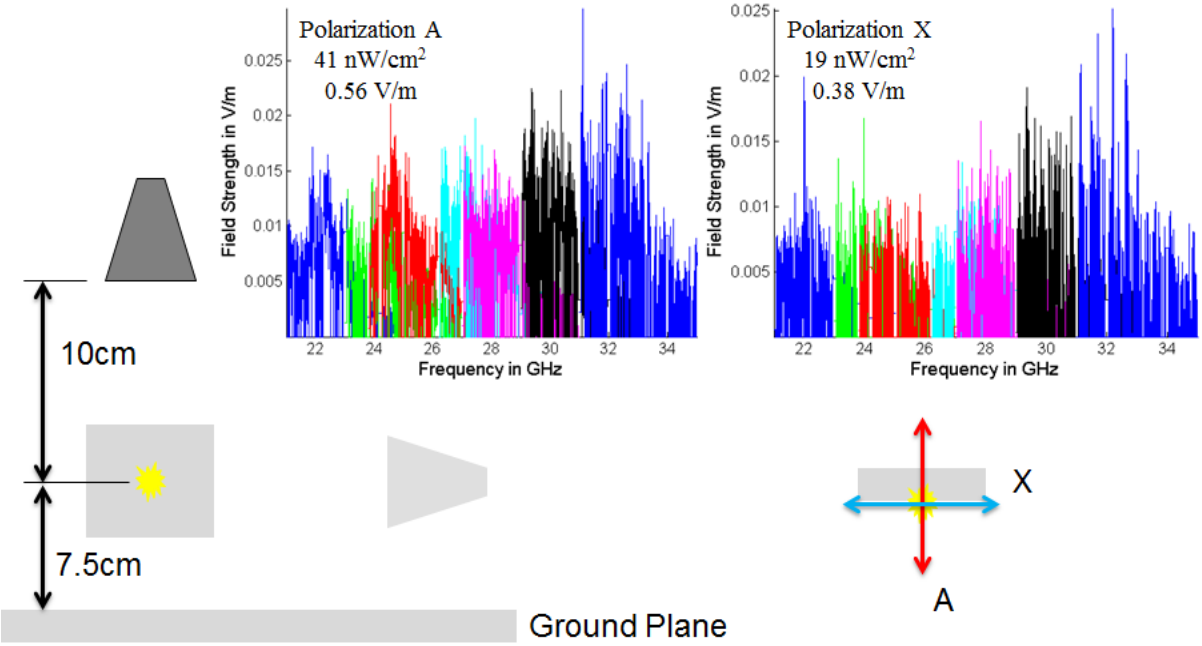

Figure 44: FIRF measurements taken out of the horizontal plane.

To better characterize the polarization of filament induced RF radiation, RF measurements were repeated with the antenna located direct above the target, outside of the horizontal plane. The experimental arrangement, direction of field polarization, and results are shown in Figure 44. Total field irradiance was twice as strong when the antenna polarization was parallel to the surface normal, while irradiance comparable to those obtained from vertically polarized measurements in the horizontal plane was obtained when the antenna was polarized orthogonal to the surface normal. Given the approximate cylindrical symmetry of the arrangement (the setup is cylindrically symmetric in the absence of the ground plane), these results are consistent with those obtained at 90^{o} relative to the surface normal in the horizontal plane.

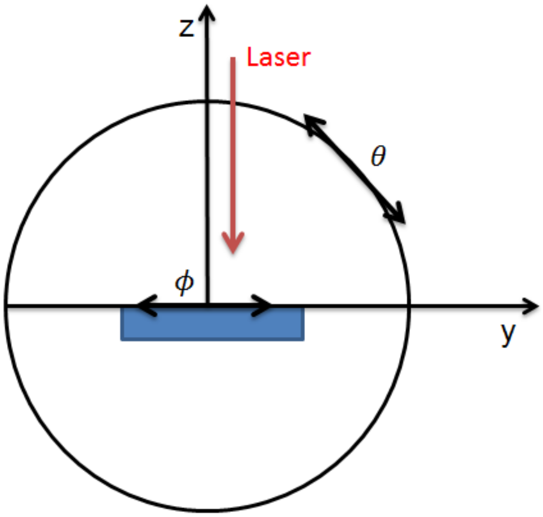

Figure 45: Orientation of RF polarizations in spherical coordinates.

A simple arrangement that describes the polarization response obtained from the angle resolved and out of plane experiments is shown in Figure 45. Here the z-axis of the spherical coordinate system is aligned parallel to the surface normal. If the filament induced RF radiation is taken to be polarized along the zenith within this arrangement, then the experimentally observed polarization dependence is satisfied. This polarization arrangement is consistent with a dipole radiation source aligned to the target normal.

Table 1: Total spectral irradiance as a function of laser polarization and orientation relative to the target for horizontally polarized copper measurements.

Laser Polarization	$\theta = 10^o$	$\theta = 45^o$	$\theta = 90^o$	Above Target
Horizontal	$26\frac{nW}{cm^2}$	$48\frac{nW}{cm^2}$	$58\frac{nW}{cm^2}$	$41\frac{nW}{cm^2}$
Vertical	$27\frac{nW}{cm^2}$	$42\frac{nW}{cm^2}$	$50\frac{nW}{cm^2}$	$25\frac{nW}{cm^2}$

The influence of laser polarization on filament induced RF radiation was also investigated by carrying out all aforementioned measurements for both laser polarizations. The polarization dependence of the previously discussed angle resolved FIRF measurements are summarized in Table 1. Laser polarization had little influence on measurements taken within the horizontal plane, with disparities no greater than 16% observed between the two laser polarizations. FIRF radiation can therefore be concluded to be independent of laser polarization. This further reinforces the concept of a dipole like radiator that explains the previously observed polarization dependence of FIRF.

5.5 Focal Length Resolved FIRF Experiments

Laser filamentation occurs when an ultrafast pulse exceeds the critical power for filamentation. Because of the Kerr effect responsible for filamentation, no additional optical elements are required to achieve filamentation once this threshold is exceeded. However, filaments and their characteristics can be altered by modifying the optical wavefront of the laser pulse responsible for filamentation prior to the onset of filamentation, such as when a conventional converging lens is used to assist and control the filamentation process.

The most obvious effect of using a lens to assist in filamentation is the reduced propagation distance required before the onset of filamentation. Another effect that proves to be important is the wavefront modification to the peripheral field. While the Kerr effect at the center of a Gaussian beam is identical to that of a converging lens in that energy from the refracted wavefront will eventually reach the optical axis, energy lying at the beams periphery will never reach the optical axis due to the departure of the Gaussian refractive index lag from that of a spherical lens, as described in Chapter 4. However, when a spherical lens is used to assist in the filamentation process, the wavefront modification will result in the eventual convergence of all incident light with the optical axis, increasing optical power at or near the optical axis, much like the linear case.

The RF radiation resulting from filament matter interaction using unaided filament formation proved to be particular weak, often below the detection threshold of heterodyne detector, while clear RF signals were obtained from those experiments which used a lens to assist with filament formation. To better understand the effects of using a lens to assist in filament formation on filament-matter induced RF radiation, the dependence of RF radiation on lens focal length was investigated.

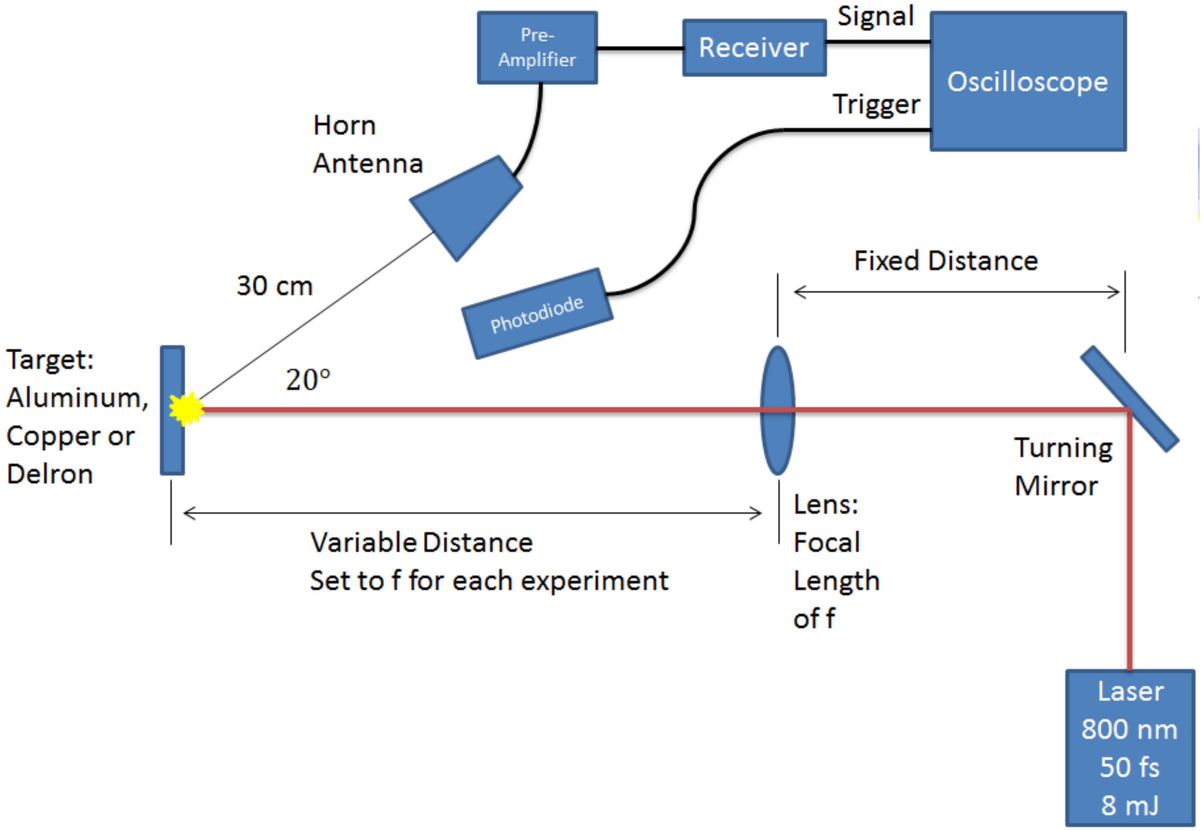

Figure 46: Experimental setup used to evaluate the effect of focality on filament induced RF radiation.

The experimental setup is depicted in Figure 46. An 8 *mJ* laser pulse was turned into the laser range using a plane mirror. The laser pulse was then passed through one of several different lenses, of focal length 20 *cm*, 50 *cm*, 1 *m*, 2 *m*, 3 *m*, 5 *m* or 10 *m*, located at a fixed distance from the turning mirror. A target composed of a solid sheet of aluminum, copper or delron was then placed in the focal plane of the lens. The target was mounted on a two-axis translation stage, so that it could be adjusted in the plane perpendicular to the incident beam. The surface of each material that was exposed to the laser was cleaned with acetone before the experimental was carried out. The exposed surface was oriented normal to the beam propagation path.

The 1-18 *GHz* horn antenna was placed 30 *cm* from the target at an angle of $20°$ relative to the exposed surface normal. The oscilloscope trigger was connected to a fast photodiode, which monitored the visible light emission from the plasma that was generated whenever a laser pulse irradiated the target surface. The receiver was adjusted to filter RF frequencies outside of 9-13 *GHz* and to downconvert 9-13 *GHz* to 0-4 *GHz*.

Each experiment was carried out by selecting a material and lens focal length. The material target was then placed in the focal plane of the lens. The antenna and photodiode were moved with the target whenever the lens was replaced with a lens of different focal length, so that the antenna and photodiode always maintained a fixed distance and orientation with respect to the target.

Each experiment was carried out by irradiating the target with 30 separate laser pulses. Between each pulse, the translation stage on which the target was mounted was used to move the ablated region of the target surface outside the beam path, so each subsequent pulse would strike a surface free from ablation damage caused by previous laser shots. Oscilloscope trigger settings ensured that only a single oscilloscope trace was taken for each laser pulse.

Radiation background characterization was conducted by placing a beam block in the beam path between the antenna and the photodiode. With the beam block in place, the photodiode still registered individual laser pulses while the antenna collected background radiation in the absence of any laser plasma. Thirty background measurements were taken under these conditions for use as a reference.

Raw time domain samples are shown in Figure 47. For all RF pulses, measured pulse duration was less than one nanosecond, typically between 0.5 and 1 *ns*. This is only marginally greater than the 250 *ps* minimum time resolution of the detection setup as dictated by the 4 *GHz* analog bandwidth of the equipment used. Pulses typically exhibited both a positive and negative signal voltage component with a single zero crossing. In most cases, one component is considerably stronger relative to the other. Many pulses possess an oscillatory tail with a signal strength between one-quarter and one-tenth of the peak-to-peak value of the main pulse, which persist for up to 10 *ns* and appear to be composed of oscillations that are too rapid to be temporally resolved.

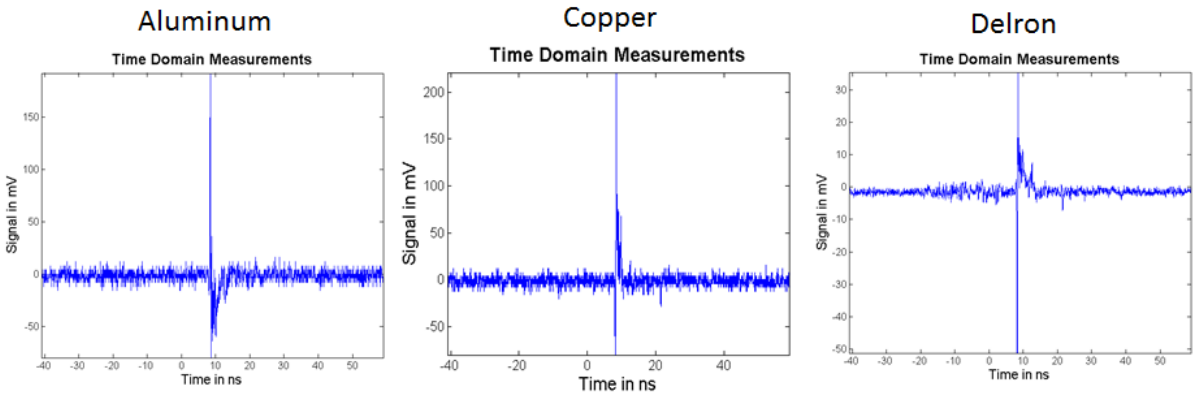

Figure 47: Time domain samples collected for a 50 cm focal length lenses.

The spectrum of the measured signals was obtained by carrying out a fast-Fourier transform on the data in MATLAB. The measured signal spectra were converted to power signal spectra, and then averaged across the 30 pulses used for each of the experimental runs. The resulting spectra for copper are plotted in Figure 48. Each plot contains a frequency spectrum recorded both in the presence (blue) and absence (yellow) of a laser-matter interaction.

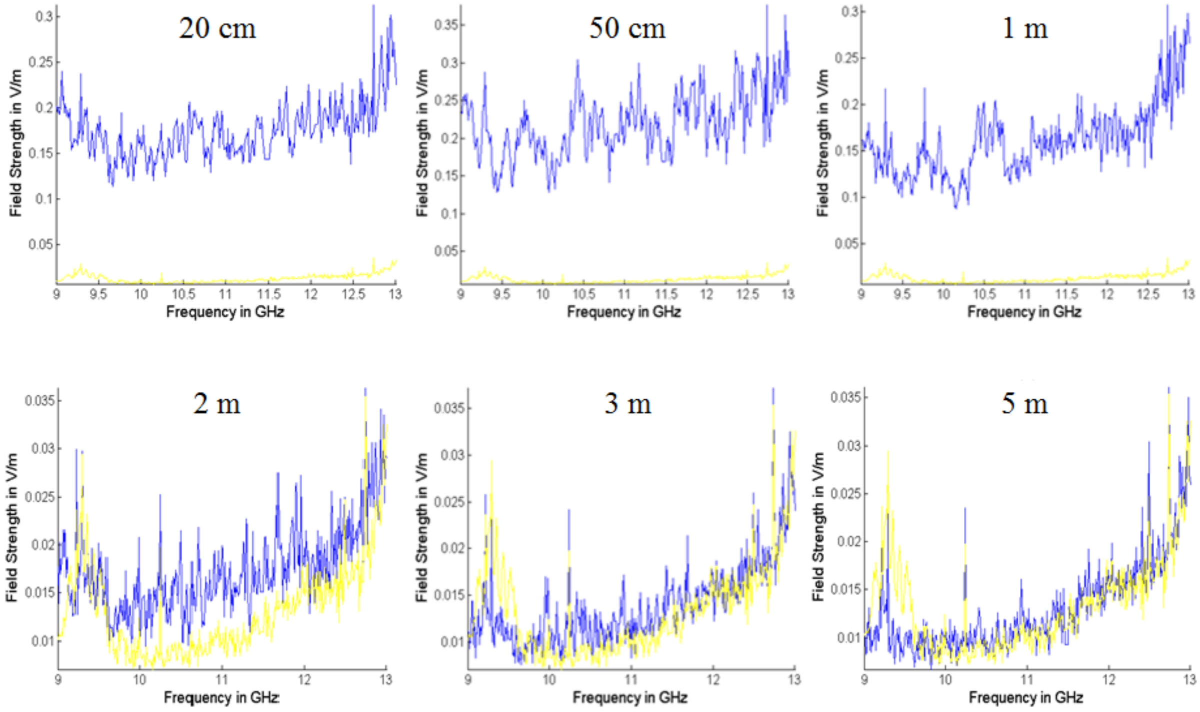

Figure 48: RF spectra generated from laser-matter interaction with copper lying within the focal plane of a spherical lens. For each lens evaluated, 30 spectra where recorded and averaged. RF radiation background measurements are shown in yellow, while RF signal measurements are given in blue.

For a lens focal length of 5 *m*, a signal to noise ratio only marginally greater than one is observed. By shortening the lens focal length, the strength of the measured signal is increased across the entire bandwidth of observation. For a focal length of 1 *m*, the recorded signal field strength is approximately an order of magnitude greater than the background field across the entire spectrum under investigation, indicating an abrupt increase in RF pulse power when transition from a 2 *m* lens to a 1 *m* lens.

The total irradiance and field strength was calculated for all measured spectra. For each material and lens focal length, the average and standard deviation was calculated from the resulting ensemble. The standard deviation was taken as the measurement error. A plot of the average field strengths as a function of both material and focal length is plotted in Figure 49.

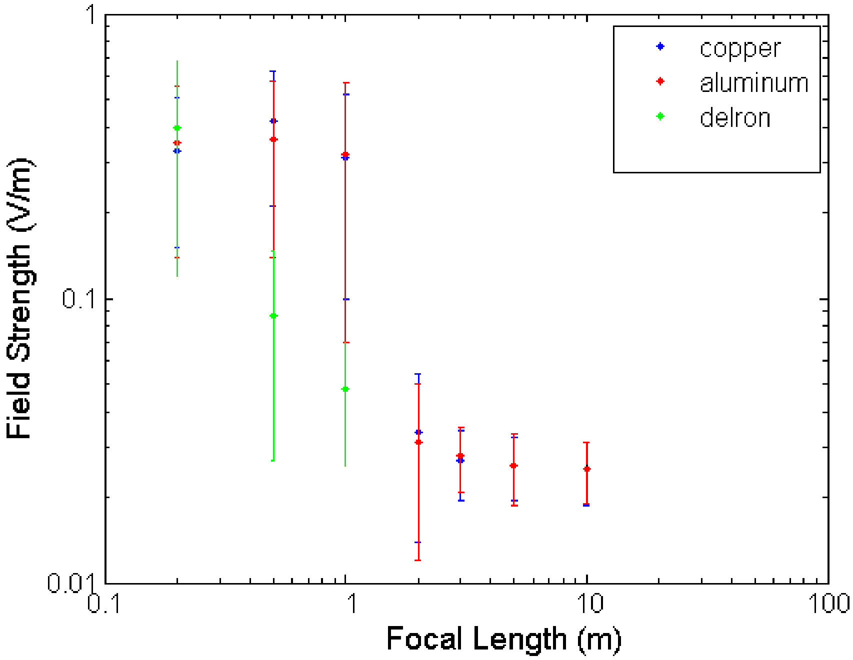

Figure 49: Integrated RF pulse field strength as a function of focal length.

For the three materials investigated, RF emission field strength was less than 0.04 *V/m* when lens focal lengths of 2 *m* or more were used. When the focal length is reduced to 1 *m*, an order of magnitude increase in measured field strength is observed for copper and aluminum, for which a RF field strength of 0.31 *V/m* and 0.32 *V/m* are obtained. However, increases in field strength when the lens focal length is further reduced for these materials is minimal, with a maximum field of 0.42 *V/m* and 0.36 *V/m* obtained for copper and aluminum respectively using a 50 *cm* lens while further reduction in lens focal length results in a minor reduction in measured field strength for both materials.

A similar pattern is observed for delron. Here, the onset of the order of magnitude increase in field strength is delayed, and a field comparable to those obtained for copper and aluminum at focal lengths of 1 *m* or less required a 20 *cm* focal length lens.

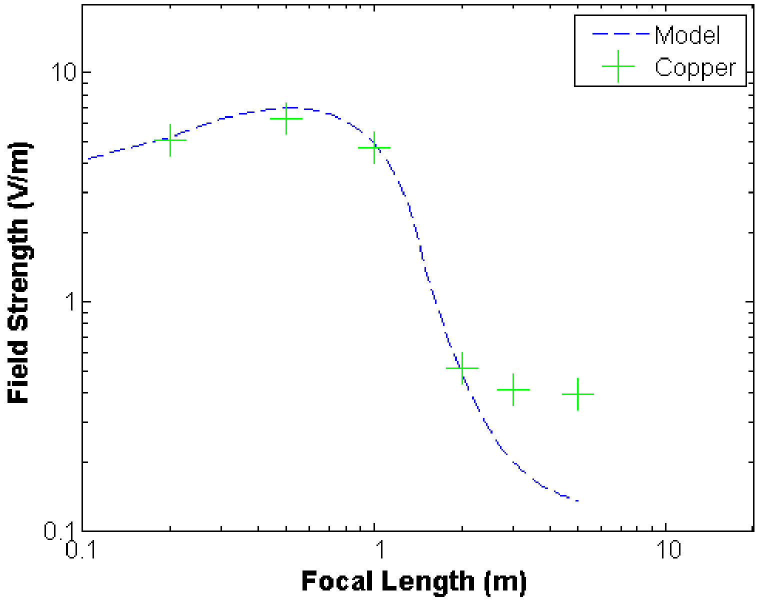

Figure 50: Comparison of simulation results to data for filament-matter induced RF radiation.

The focal length dependence observed in is unusual in that the observed field strengths seemed to be separated into two discrete plateaus, with field strength values observed for focal lengths of 1 *m* or less being an order of magnitude greater than those observed for 2 *m* or more. From Equation 181, a continual increase of RF radiation field strength with lens focal length would be expected. However, the plasma critical density limits the charge carriers that can be extracted from the material, resulting in the saturation of the measured field once sufficient irradiance is obtained. Once the extraction limit is reached, decreases in focal length only reduces the material surface available for free electron extraction, resulting in a gradual reduction in RF field strength with decreasing focal length, explaining the first plateau.

In the case of increasing focal length, natural filamentation will maintain a peak on-axis irradiance of approximately $5 \cdot 10^{13}\ W/cm^2$ over a $100\ \mu m$ diameter, ensuring a minimal level of electron extraction even as the focal length approaches infinity. In addition to this effect, the noise limits the detection threshold of the measurements, as can be seen from Figure 48. These effects collectively result in the second plateau.

With the exception of the noise, all of these effects have been incorporated into the numerical model discussed in the beginning of this chapter. Simulation results for copper are shown in Figure 50. Agreement is obtained between simulation and experiment for lens focal lengths of 2 *m* or less. The model underestimates the field strengths obtained at 3 and 5 *m* because it does not account for noise.

5.6 Conclusion

Measurable broadband, fast-pulsed RF radiation can be obtained by focusing laser filaments onto a variety of solid media. The resulting pulses are only a few nanoseconds in duration and are sufficiently broadband to fill the spectra under investigation. The pulse polarization is consistent with a dipole radiator aligned to the laser propagation direction.

By modeling the RF source as a stream of filament driven avalanche ionized electrons traveling away from the irradiated material at the electron thermal velocity, a dipole radiation source was obtained. Focality resolved FIRF measurements could be accurately calculated using the simulated dipole radiator for focal lengths as great as 2 *m*, and could likely be extended to longer focal lengths if the effect of noise on the RF measurements could be reconciled with the model. This suggest the observed RF radiation is a consequence of a sub-picosecond stream of breakdown electrons resulting from the filament-matter interaction, as opposed to a slower thermal process.

CHAPTER 6: MICROWAVE GUIDING USING FILAMENTS

The most straightforward application of the conductive channels that lie within the core of the filaments is to guide electric current directly along the plasma. In this regard, laser filaments have been employed to trigger and guide high-voltage discharges along the laser propagation path, in the hopes of eventually achieving laser guided lightning. Such laser assisted discharges have been demonstrated at distances up to 4 *m* and result in straighter discharge paths then obtained for the normal dielectric breakdown of air [130].

More recently, laser filaments have been employed as waveguides. In 2007, Dormidonov et al. claimed an array of plasma filaments could be used as a waveguide for microwave frequency radiation, which would be confined by the array as microwave frequencies fall below the filament plasma frequency [12]. Musin et al made a similar claim, but on the basis of index guiding along the filament array [18]. Guiding of microwaves with filaments were experimentally demonstrated by Chateauneuf et al., using a 100 *TW* laser system to produce a cylindrical array of filaments 45 *mm* in diameter, which guided microwaves in a manner described by Dormidonov [13]. A separate means of guiding microwaves was investigated by Bogatov et al, in which a filament was used in conjunction with a copper wire to form a twin-lead transmission line capable of transmitting a 24 *GHz* microwave signal [131].

Recent research suggests that filamenting non-diffracting beams are a promising source of waveguiding geometries. In 2008, Polesana et al claimed pulsed ultrafast Bessel beams could be used to produce filamentation [132]. This was demonstrate by Akturk et al. and Polynkin et al., who used Bessel filaments to produce plasma channels of 1 *m* and 2.25 *m* in length respectively

[133] [104]. Among their findings, Bessel filaments were found to produce plasma channels that were both longer and more stable than their equivalent Gaussian counterparts, characteristic which are desirable for microwave guiding applications. Previously, Fan et al. generated a cylindrical plasma sheath 10 μm in diameter using a 5th order Bessel beam produced using 100 *ps* pulses [134]. However, the peak irradiance of 2.5 TW/cm^2 obtained in the experiment was not sufficient to obtain filamentation.

It is believed that the phenomenon investigated in the previous chapters can be readily adapted to the end of microwave guiding using transient plasma and filament structures, and that microwave guiding experiments are a natural and logical extension of the investigations that have been undertaken on the previous topics. To this end, various guiding structures that can be obtained through the application of filaments and non-diffracting beams are theoretically investigated.

6.1 Filaments as Waveguiding Elements

Laser filaments in air under normal circumstances possess several properties that are consistently reproducible despite changes in the laser pulses and experimental conditions used in their generation. These properties include the filament peak irradiance, the filament core diameter, and the filament plasma density. Such consistency in filament properties are desirable in that they enabled evaluation of filament guiding structures prior to establishing the particular properties of the laser pulse used in their generation. However, such consistency is also problematic when it is desired to modify filament properties to improve their radiation guiding characteristics.

Filaments possess two properties which enable them to guide radiation. The 50-100 μm transient plasma present in the filament core possesses a resistivity of $40\ k\Omega/m$ [82] [101]. Given the electron density in filaments of at least $10^{16}\ cm^{-3}$, the resulting plasma frequency of the core is 5.6 – 17.8 *THz*, well above the operating frequency of conventional RF and microwave communication systems. Filaments can therefore be employed as conductors [90], to either guide lower frequency RF radiation as a transmission line by conducting RF current through a pair of two or more electromagnetically coupled filaments, or as a waveguide at microwave and THz frequency, by confining traveling wave modes within an array of conductive filaments.

Alternatively, the refractive index drop associated with a filament can be used to theoretically guide electromagnetic waves of any frequency. By arranging multiple filaments such that a refractive index drop occurs with increasing distance from the optical axis, a dielectric guiding structure can be obtained, operating in a manner analogous to optical fiber. In both cases, arranging and maintaining the correct filament geometries, and if necessary, finding a means to modify undesirable filament properties, is critical in obtaining effective guiding structures.

6.2 Synthesis of Guiding Structures

All filament based microwave guiding structure needs to have a definite transverse cross section which maintains its geometry during propagation. While the mechanisms for maintaining shape and geometry are already present in the filamentation process, multi-filamentation proves to be far more chaotic and difficult to maintain. To improve the quality and control of a multi-filamentation process, geometry maintaining light pulses with several irradiance peaks, each corresponding to a filament, would be ideal. Such beams are the non-diffracting beams discussed in Chapter 3, which have already been shown to influence filament propagation in Chapter 4.

Generating structured beams ideal for microwave guiding requires the generation of arbitrary transverse beam profiles. As discussed previously, Bessel beams form a basis for scalar (uniformly polarized) electromagnetic waves that are particularly effective in describing radially symmetric structures, implying any microwave guiding structure can be obtained through a suitable superposition of Bessel beams. However, it is quite possible an infinite superposition of Bessel beams will be required to obtain a specific geometry. Thus, optimal beam guiding geometries should enable both efficient guiding while simultaneously requiring a small number of Bessel beams to synthesize, or alternatively an efficient method for generating a large to infinite superposition of Bessel beams.

6.3 Filament Transmission Line

While the conductive plasma channel within a filament can be used in the direct conduction of current, the high impedance of $40\ k\Omega/m$ [101] obtained using individual filaments requires the use of high-voltage power supplies to drive current over extended distances. Alternatively, multiple filaments can be used to synthesize transmission line structures from plasma channels, which can be used in the transport of radio-frequency and microwave signals.

Transmission line theory will be used to analyze the guiding properties of these plasma channel arrangements. In general, signal propagation along transmission lines is described by the equations [135]

$$\frac{\partial^2 V}{\partial x^2} - \gamma^2 V = 0 \tag{194}$$

$$\frac{\partial^2 I}{\partial x^2} - \gamma^2 I = 0 \tag{195}$$

where the propagation constant γ is defined by the distributed resistance (R), the distributed conductance (C), the distributed inductance (L), and the distributed leakage conductance (G) through

$$\gamma^2 = (R + i\omega L)(G + i\omega C) \tag{196}$$

Equations 194 and 195 have the solutions

$$V(x) = V_+ \exp(-\gamma x) + V_- \exp(\gamma x) \tag{197}$$

$$I(x) = I_+ \exp(-\gamma x) + I_- \exp(\gamma x) \tag{198}$$

which are related by the line impedance

$$\frac{V}{I} = Z = \frac{R + i\omega L}{\gamma} = \sqrt{\frac{R + i\omega L}{G + i\omega C}} \tag{199}$$

The simplest transmission line structure is the twin-lead or ladder line. This transmission line is composed of two parallel conductors. Signals traveling along the line drive alternating current in both conductors with a relative potential difference between the conductor pair, resulting in a time varying electric field. The electric field propagates between the conductors supported by current at either end. Such ladder lines represent the simplest wave guiding structures that can be obtained using laser filaments, requiring the simultaneous generation of only two parallel filaments.

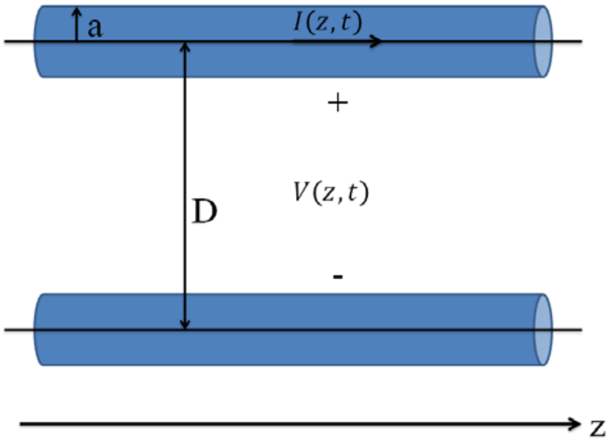

Figure 51: Depiction of a twin-lead line with relevant dimensions.

Ladder line properties are well understood and are given by [135]

$$R = \frac{\sigma}{\pi a^2} \tag{200}$$

$$L = \frac{\mu}{\pi} \operatorname{arccosh}\left(\frac{D}{2a}\right) \tag{201}$$

$$G = \frac{\pi \sigma_l}{\operatorname{arccosh}\left(\frac{D}{2a}\right)} \tag{202}$$

$$C = \frac{\pi \epsilon}{\operatorname{arccosh}\left(\frac{D}{2a}\right)} \tag{203}$$

for perfectly cylindrical, symmetric conductors. Here, a is the radius of the individual conductors, σ is the conductance of the lines, σ_l is the leakage conductance between the lines, and D is the spacing between the axes of each conductor. To evaluate filament based ladder lines, the following parameters are used to represent filaments [82] [101]

$$a = 50\ \mu m \tag{204}$$

$$G \cong 0 \tag{205}$$

$$\epsilon = \epsilon_0 \tag{206}$$

$$\mu = \mu_0 \tag{207}$$

$$R = 40 \frac{k\Omega}{m} \tag{208}$$

The requirement that equations 201 and 203 have non-singular, real values introduces the additional restriction that

$$D > 100\ \mu m \tag{209}$$

These values can be used to calculate γ by substituting $G = 0$ along with equations 201 and 203 into Equation 196 gives

$$\gamma = \sqrt{i \frac{\pi \epsilon_0 \omega R}{\operatorname{arccosh}\left(\frac{D}{2a}\right)} + \frac{\omega^2}{c^2}} \tag{210}$$

Separating γ into its real and imaginary components

$$\gamma = \alpha + i\zeta \tag{211}$$

Equation 210 can be expressed as a combination of loss (α) and phase (ζ) terms

$$\alpha = \left[\left(\frac{\pi \epsilon_0 \omega R}{\operatorname{arccosh}\left(\frac{D}{2a}\right)} \right)^2 + \left(\frac{\omega}{c}\right)^4 \right]^{\frac{1}{4}} \cos\left[\arctan\left(\frac{\pi R}{2\mu_0 \omega \operatorname{arccosh}\left(\frac{D}{2a}\right)} \right) \right] \tag{212}$$

$$\zeta = \left[\left(\frac{\pi \epsilon_0 \omega R}{\operatorname{arccosh}\left(\frac{D}{2a}\right)} \right)^2 + \left(\frac{\omega}{c}\right)^4 \right]^{\frac{1}{4}} \sin\left[\arctan\left(\frac{\pi R}{2\mu_0 \omega \operatorname{arccosh}\left(\frac{D}{2a}\right)} \right) \right] \tag{213}$$

The transmission line performance can now be evaluated by solving equations 212 and 213 using the values listed in equations 204 to 209.

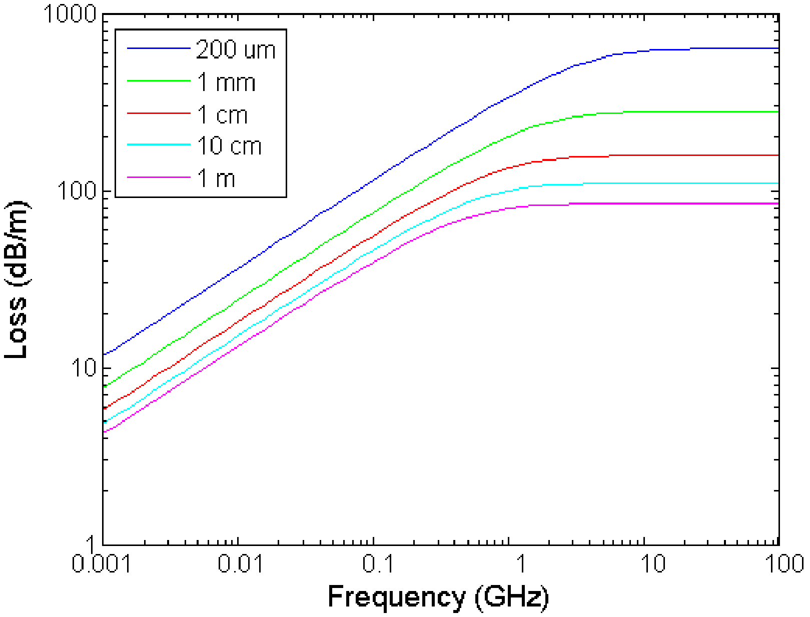

Figure 52: Frequency dependent propagation losses of twin-lead filament lines of various spacings.

The transmission line losses were calculated from Equation 212 using MATLAB. The results are shown in Figure 52. Acceptable losses of 10 *dB/m* or less are obtained for frequencies below 10 *MHz*. Unfortunately, the plasma resulting from filamentation only persist for 1 *ns* [101], making the guiding structure suitable only for frequencies over 1 GHz.

To make use of filament twin-lead lines for guiding, either the losses need to be reduced for frequencies over 1 *GHz*, or filament plasma needs to persist for at least a microsecond. Fortunately, a means of extending the duration of the plasma channel is available using a series of laser pulses, where the initial laser pulses is used to form the filament according to the physics described in Chapter 4, and one of more subsequent pulses, typically nanoseconds in duration [136], are used to heat the plasma within the filament. This igniter-heater approach to filamentation has proved to extend plasma channel lifetimes to at least 1 μs [137] [138], sufficiently long to support *MHz* frequency guiding on the twin-lead transmission line.

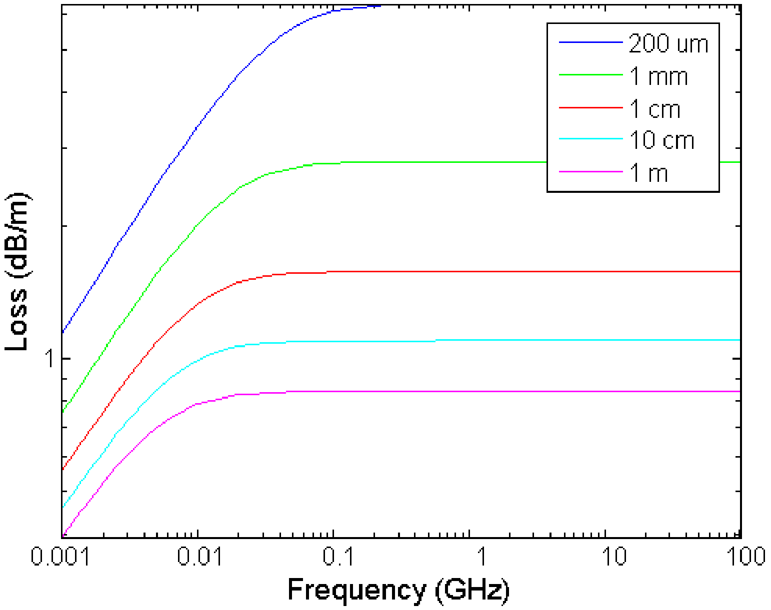

Figure 53: Frequency dependent losses of twin-lead lines of various spacings possessing conductivity 100 times that of unaugmented laser filaments.

The effect of increasing filament conductivity on transmission line performance was also investigated. By increasing filament conductivity by a factor of 100 to obtain a line impedance of $400\ \Omega/m$, losses can be kept below 10 dB/m over the entire frequency range investigated, as shown in Figure 53. These calculations demonstrate that the performance of filament transmission lines can be improved in both transmission efficiency and bandwidth by several orders of magnitude if an effective means of increasing filament conductivity can be identified.

Further improvements in transmission line performance can be obtained using a twisted pair transmission line. A twisted pair is a twin-lead line is composed of two conductors which are twisted along a central axis. The twisted pair arrangement is a geometric modification to the twin-lead line that improves EMI resistance and reduces radiation losses along the transmission line. A filament analog to such transmission lines can readily be obtained from the helical filaments demonstrated in Chapter 4.

From the theory devised for filament transmission lines, an experimental procedure for the filament guiding of microwave radiation can be devised. First either multiple femtosecond pulses are used to generate a pair of parallel propagating filaments, are multiple filaments are obtained from a specially prepared ultrafast pulse, as in the case of helical beams. A several hundred millijoule nanosecond laser pulse with a delay up to 1 *ms* is then focused onto the filament plasma channels using an axicon [136]. A microsecond to sub-microsecond radio-frequency pulse using a 10-100 *MHz* carrier and synchronized with the nanosecond laser is then coupled onto the filament. If this procedure is carried out correctly, the guiding of the RF pulse along the filament pair is expected.

6.4 Waveguiding Using Filaments

Electromagnetic waves of frequency below the plasma frequency

$$\omega_p = \sqrt{\frac{ne^2}{\epsilon_0 m}} \qquad \textbf{(214)}$$

treat the associated plasma as a conductor and are unable to propagate through the plasma. Under such conditions, the plasma could be employed as the boundary of a waveguide. In the case where the plasma is generated through laser filamentation, the plasma electron density will fall in the range

$$n_e = 10^{16} - 10^{17}\frac{1}{cm^3} \qquad \textbf{(215)}$$

yielding a plasma frequency of

$$f_p = 2\pi\omega_p = 2\pi\sqrt{\frac{\left(10^{16} - 10^{17}\frac{1}{cm^3}\right)\cdot\frac{10^6 cm^3}{m^3}\cdot(1.60\cdot 10^{-19}C)^2}{8.854\cdot 10^{-12}\frac{F}{m}\cdot 9.11\cdot 10^{-31}\,kg}} = 5.6 - 17.8\,THz \qquad \textbf{(216)}$$

Assuming a cylindrical filament geometry can be obtained for which the electric field of a guided wave is zero for a radius of $r = r_0$, with an interior void of plasma, then for $r < r_0$ the electric field using the waveguide can be described using the equations

$$\left[\frac{\partial^2}{\partial r^2} + \frac{1}{r}\frac{\partial}{\partial r} + \frac{1}{r^2}\frac{\partial^2}{\partial\phi^2} + \frac{\omega^2}{c^2} - k^2\right]E_z = 0 \qquad \textbf{(217)}$$

$$\left[\frac{\partial^2}{\partial r^2}+\frac{1}{r}\frac{\partial}{\partial r}+\frac{1}{r^2}\frac{\partial^2}{\partial \phi^2}+\frac{\omega^2}{c^2}-k^2\right]B_z=0 \tag{218}$$

where the remaining vector components are described by

$$E_r=\frac{i}{\frac{\omega^2}{c^2}-k^2}\left(k\frac{\partial E_z}{\partial r}+\frac{\omega}{r}\frac{\partial B_z}{\partial \phi}\right) \tag{219}$$

$$E_\phi=\frac{i}{\frac{\omega^2}{c^2}-k^2}\left(\frac{k}{r}\frac{\partial E_z}{\partial \phi}-\omega\frac{\partial B_z}{\partial r}\right) \tag{220}$$

$$B_r=\frac{i}{\frac{\omega^2}{c^2}-k^2}\left(k\frac{\partial B_z}{\partial r}-\frac{\omega}{rc^2}\frac{\partial E_z}{\partial \phi}\right) \tag{221}$$

$$B_\phi=\frac{i}{\frac{\omega^2}{c^2}-k^2}\left(\frac{k}{r}\frac{\partial B_z}{\partial \phi}+\frac{\omega}{c^2}\frac{\partial E_z}{\partial r}\right) \tag{222}$$

The electric and magnetic fields may be obtained by first solving for longitudinal components of the electromagnetic field and then acquiring the remaining components by substituting into the above equations (see Appendix F). The solutions to the above equations are

$$E_z=E_{z,0}J_m(k_\perp r)\exp(im\phi) \tag{223}$$

$$B_z=B_{z,0}J_m(k_\perp r)\exp(im\phi) \tag{224}$$

where

$$k_{\perp}^{2} = \frac{\omega^{2}}{c^{2}} - k^{2} \tag{225}$$

The boundary condition requires

$$J_m(k_{\perp} r_0) = 0 \tag{226}$$

which imposes the condition

$$k_{\perp} \geq \frac{2.40}{r_0} \tag{227}$$

which corresponds to

$$J_0(k_{\perp} r_0) = 0 \tag{228}$$

Observing that

$$k_{\perp} \leq \frac{\omega}{c} \tag{229}$$

then

$$r_0 \geq \frac{2.40c}{\omega} \geq \frac{2.40c}{\omega_p} \geq \frac{2.40 \cdot 3.00 \cdot 10^{8}\, \frac{m}{s}}{2\pi \cdot 5.6\, THz} = 20\ \mu m \tag{230}$$

Therefore any viable filament guiding structure must be at least 40 μm in diameter to prevent the cutoff frequency from exceeding the plasma frequency. Provided this conditions is satisfied, single mode operation is desirable. Single mode operation obtained by ensuring the next order mode is below the cutoff frequency as dictated by the boundary conditions

$$J_1(k_\perp r) = 0 \tag{231}$$

for which

$$k_\perp \leq \frac{3.83}{r_0} \tag{232}$$

thus establishing a range for single mode propagation of

$$0.382\frac{c}{r_0} \leq \nu \leq 0.610\frac{c}{r_0} \tag{233}$$

To synthesize the guiding structure, a hollow array of filaments must be obtained. Such an arrangement can be obtained using an ultrafast pulse with a null at the center of the beam. Observing that in the expansion of any beam in the orthonormal basis

$$E(r,\phi) = \sum_{m=-\infty}^{\infty} b(\phi)\exp(im\phi)\int_0^\infty a(k)J_m(kr)dk \tag{234}$$

where k is the wavenumber, the following relations hold

$$\int_0^\infty a(k)J_0(0)dk \neq 0\,\forall\, a(k)\ s.t. \int_0^\infty a(k)dk \neq 0 \tag{235}$$

$$\int_0^\infty a(k)J_m(0)dk = 0\,\forall\, a(k), m \neq 0 \tag{236}$$

Therefore, it is sufficient to generate a beam with no zero order azimuthal modes to obtain a hollow beam. Because conventional Gaussian beams lack any azimuthal components when expanded in the basis of Equation 234, hollow beams can typically be obtained by transmission of a Gaussian beam through any vortex plate which induces an integer azimuthal phase. As special case, the use of an axicon in series with an azimuthal phase plate of order m can be used to obtain the Bessel beam

$$E(r,\phi) = E_0 J_m(k_\perp r)\exp(im\phi) = E_0 J_m(\beta k r)\exp(im\phi) \tag{237}$$

Such Bessel beams form a series of concentric rings, as in the case of the zero order Bessel beams, but have a null as opposed to a peak on the optical axis. The innermost hollow ring of these Bessel beams will have the highest irradiance, and therefore be the first to filament. The diameter of the innermost ring will be at least

$$d \geq 2\frac{1.8412}{k_\perp} = \frac{3.68}{\beta k} = \frac{0.59\lambda}{\beta} \tag{238}$$

where the minimum diameter corresponds to order ± 1 Bessel beams, while larger diameters are obtained for Bessel beams of order $|m| > 1$.

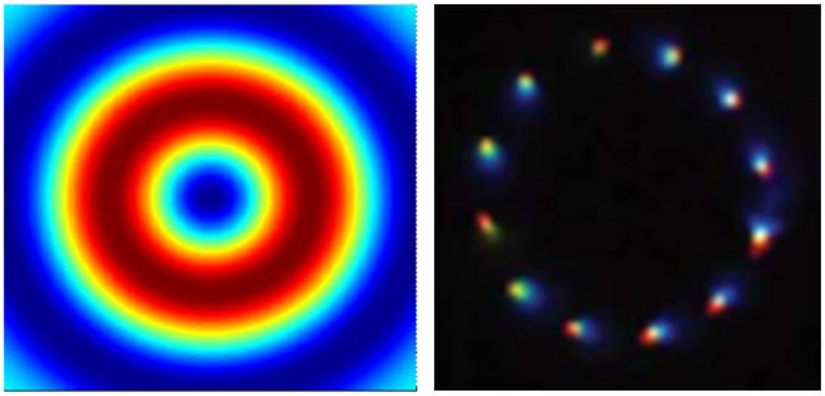

Figure 54: Irradiance profile of a higher order Bessel beam (left) and the filament array resulting from the propagation of a 12th order Bessel beam in water recorded by Shiffler et al. [139]

Review of literature indicates such hollow beam structures will result in the cylindrical arrays which are desirable for guiding if sufficient instantaneous power is available. Filament arrays in water have been obtained by Shiffler et al. using order 4, 8, 12 and 18 Bessel beams [139], obtaining a number of filaments in the array equal to the azimuthal order of the beam, as shown in Figure 53. Because of the higher operating frequency of the cylindrical filament waveguides, and igniter-heater concept need not be employed when using this approach to guiding microwave radiation.

6.5 Index Guiding Using Filaments

While the filament plasma can be used as a surrogate for a conductive waveguide, the refractive index change associated with filamentation can be used in the index guiding of electromagnetic radiation. Index guiding requires a drop in refractive index with increasing distance from the optical axis. Provided this condition is satisfied, then for a cylindrical geometry the guided fields will be described by

$$E_z(r,\phi,z) = AJ_m(\mathrm{k}_\perp \mathrm{r}) \exp(im\phi) \exp(ik_z z) \tag{239}$$

$$H_z(r,\phi,z) = BJ_m(k_\perp r) \exp(im\phi) \exp(ik_z z) \tag{240}$$

the remaining vector components can be retrieved using

$$E_r = \frac{-i}{k^2 n^2 - k_z^2}\left[k_z \frac{\partial E_z}{\partial z} + i\frac{m}{r}\eta_0 H_z\right] \tag{241}$$

$$E_\phi = \frac{1}{k^2 n^2 - k_z^2}\left[k_z \frac{m}{r} E_z + ik\eta_0 \frac{\partial H_z}{\partial r}\right] \tag{242}$$

$$H_r = \frac{-1}{k^2n^2 - k_z^2}\left[ik_z\frac{\partial H_z}{\partial r} + \frac{k^2n^2}{\eta_0}\frac{m}{r}E_z\right] \tag{243}$$

$$H_\phi = \frac{-i}{k^2n^2 - k_z^2}\left[ik_z\frac{m}{r}H_z + \frac{k^2n^2}{\eta_0}\frac{\partial E_z}{\partial z}\right] \tag{244}$$

where

$$\eta_0 = \sqrt{\frac{\mu_0}{\epsilon_0}} \tag{245}$$

For $n_1 > n_2$, where n_1 is the refractive index at the interior, the dispersion relation is given by

$$k_\perp^2 + k_z^2 = k^2n_1^2 \tag{246}$$

for the guided modes and by

$$-\gamma^2 + k_z^2 = k^2n_2^2 \tag{247}$$

for the evanescent modes on the exterior. Collectively both these modes are related by

$$u^2 + w^2 = V^2 \tag{248}$$

where

$$u \equiv k_\perp a \tag{249}$$

$$w \equiv \gamma a \tag{250}$$

$$V \equiv ka\sqrt{n_1^2 - n_2^2} \tag{251}$$

and a is the radius of the waveguiding region.

For simplicity, only single mode operation will be considered. Single mode operation requires

$$V < 2.4048 \tag{252}$$

By substituting Equation 251 into Equation 252, the maximum frequency which guarantees single mode operation can be obtained

$$\nu = \frac{\omega}{2\pi} < \frac{0.383}{\sqrt{n_1^2 - n_2^2}} \frac{c}{a} \tag{253}$$

In the case of single mode operation, only the HE_{11} modes will be confined. These modes are described by

$$E_z(r, \phi) = AJ_1(k_\perp r) \exp(i\phi) \tag{254}$$

$$H_z(r, \phi) = BJ_1(\kappa r) \exp(i\phi) \tag{255}$$

$$E_r(r, \phi) = E_0 J_0(k_\perp r) \tag{256}$$

$$E_\phi(r, \phi) = iE_0 J(k_\perp r) \tag{257}$$

$$H_r(r, \phi) = -iE_0 \left(\frac{k_z}{\mu_0 \omega}\right) J_0(k_\perp r) \tag{258}$$

$$H_\phi(r, \phi) = E_0 \left(\frac{k_z}{\mu_0 \omega}\right) J_0(k_\perp r) \tag{259}$$

where

$$E_0 = -i \frac{Ak_z}{k_\perp} \tag{260}$$

The mode diameter associated with the HE$_{11}$ modes can be approximated as the diameter associated with the first zero of the zero order Bessel function

$$d_{mode} = 2\mathrm{a} = 2 \cdot \frac{2.40}{k_{\perp}} \geq 4.80\frac{c}{\omega} = 0.764\frac{c}{\nu} \tag{261}$$

To establish a lower frequency limit for index guiding, at least 10% of the guided mode is required to remain within the guiding structure

$$d_{mode} \leq 20\mathrm{a} \tag{262}$$

The corresponding frequency constraint is

$$\nu \geq 0.038\frac{c}{a} \tag{263}$$

Combining this restriction with that obtain from Equation 253 results in the additional restriction

$$\frac{0.383}{\sqrt{n_1^2 - n_2^2}}\frac{c}{a} > 0.038\frac{c}{a} \tag{264}$$

or

$$n_1^2 - n_2^2 < 100 \tag{265}$$

The numerical aperture for such an index guiding structure is given by

$$NA = n_0 \sin\theta_m = \sqrt{n_1^2 - n_2^2} \tag{266}$$

To evaluate index guiding using filaments, three refractive indices will be considered. The refractive index of air is

$$n_0 = 1.000293 \tag{267}$$

the refractive index in the filament core due to the Kerr effect is

$$\begin{aligned} n_{kc} = n_0 + n_2 I &= 1.000293 + 3 \cdot 10^{-19} \frac{cm^2}{W} \left(10^{13} - 10^{14} \frac{W}{cm^2}\right) \\ &= 1.000296 - 1.00034 \end{aligned} \tag{268}$$

and the refractive index resulting from the formation of an air plasma in the filament

$$n = n_0 - \frac{\rho}{2\rho_c} = 1 - \frac{Ne^2}{2m_e \epsilon_0 \omega^2} = 1 - 1.59 \cdot 10^{-3} \frac{cm^3}{s^2} \frac{10^{16} \frac{1}{cm^3}}{\omega^2} = 1 - \left(\frac{635\ MHz}{\nu}\right)^2 \tag{269}$$

Equation 269 is only valid for guiding waves with frequencies over 635 MHz.

The refractive index change in the peripheral field due to the Kerr effect can safely be neglected as

$$n_{kp} = n_0 + n_2 I = 1.000293 + \ 3 \cdot 10^{-19} \frac{cm^2}{W} \left(10^{11} - 10^{12} \frac{W}{cm^2}\right) \approx 1.000293 = n_0 \tag{270}$$

If the Kerr effect is used as the means of index guiding, the limit for single mode operation is

$$\nu < \frac{115\ GHz \cdot mm}{a} (107 - 408) = (12.3\ THz - \ 46.9\ THz) \frac{mm}{a} \tag{271}$$

However, the numerical aperture is limited to

$$NA \leq 0.00245 - 0.00938 \tag{272}$$

which makes coupling radiation into the waveguiding structure extremely difficult.

If the plasma refractive index is used for index guiding then

$$\nu < \frac{115\ GHz \cdot mm}{a}\left[\left(\frac{898\ MHz}{\nu}\right)^{2} - \left(\frac{635\ MHz}{\nu}\right)^{4}\right]^{-\frac{1}{2}} \tag{273}$$

rearranging gives

$$a < 128\ mm\left[1 - \left(\frac{449\ MHz}{\nu}\right)^{2}\right]^{-\frac{1}{2}} \tag{274}$$

Equation 274 indicates that for index guiding using filament plasma, single mode operation can be obtained for all frequencies provided the plasma cylinder diameter is less than 25 *cm* across. Given the energy requirements to generate such a structure, it is likely most practical filament index guiding schemes will automatically satisfy this requirement. The restriction can alternatively be expressed as

$$\left(\frac{449\ MHz}{\nu}\right)^{2} + \left(\frac{128\ mm}{a}\right)^{2} > 1 \tag{275}$$

The numerical aperture for this guiding mechanism is

$$NA = \sqrt{\left(\frac{898\ MHz}{\nu}\right)^{2} - \left(\frac{635\ MHz}{\nu}\right)^{4}} \tag{276}$$

In the limit of large frequencies, $\nu \gg 635\ MHz$, Equation 276 reduced to

$$NA = \frac{898\ MHz}{\nu} \tag{277}$$

Unlike the Kerr index guiding case, index guiding using the plasma enables scaling of the numerical aperture by altering the frequency of the guided waves, making coupling of radiation into the structure far more practical.

CHAPTER 7: CONCLUSION

Several methods of overcoming diffraction have either been evaluated theoretically, demonstrated experimentally, or evaluated using both approaches.

Non-diffracting beams have been shown to provide exceptional control over beam propagation, enabling laser beams to curve and spiral in a manner contradictory to the behavior of conventional laser beams. The behavior of non-diffracting beams can be thoroughly and accurately described using scalar diffraction theory, in particular by employing the Fresnel diffraction integral. Through the proper understanding of diffraction theory, beam geometry, shape and dimension can be dictated through the proper modification of the beam wavefront.

Laser filamentation is a process which manifests automatically for pulses of sufficient instantaneous power, but can be readily adapted to control beam propagation. Filamentation enables the propagation of confined pulses over enormous distances and the generation of conductive plasma channels in air. Filamentation can be controlled through proper control and preparation of the laser pulse wavefront. The techniques developed for the generation and control of non-diffracting beams can be adapted to the preparation of laser filaments, which can be used to provide control over multiple filamentation. Thus filament arrays can be engineering using correctly designed non-diffracting beams.

Laser filaments proved to be an ideal means to deliver the energy necessary to generate a remote plasma source of RF radiation. Because the electric field associated with the filament was on the threshold of dielectric breakdown responsible for the generation of electrons needed in the generation of RF radiation, preparation of the filament was necessary to obtain an irradiance sufficient to generate a strong RF pulse. If the proper measures are taken, filament driven plasmas provide fast pulsed, broadband sources of radiation which can be generated at considerable distances.

Engineered filaments, whether obtained through preparation using non-diffracting beams or other means, provide a novel means to guide RF and microwave radiation. As few as two filaments can be used to construct filament arrays which act as transmission lines, suitable for the guidance of RF radiation below 100 *MHz* provided and igniter-heater technique is employed to extend the lifetime of the filament plasma. For higher frequencies, filament arrays can be employed as waveguides, guiding radiation by either using the filament plasma as a conductive boundary or the associated index modification for index guiding. These techniques should provide excellent means to confine radiation in the atmosphere, but require experimental investigation.

Collectively, the techniques which have been investigated provide a range of methods to combat diffraction effects and deliver radiant energy. With further refinement, these measures should prove to be effective under a wide variety of circumstances.

7.1 Contingencies

Despite the elegant solutions which presented themselves theoretically, a number of severe problems hampered experimental progress on the topics under investigation.

The serial configuration used for helical beam synthesis was easy to implement and align. Unfortunately, the double angle axicons proved difficult to fabricate. Those acquired from manufacturers did not match specifications. This resulted in additional alignment problems and reduction in the helical beam propagation distance. This also resulted in a mismatch between the helical beam propagation characteristics predicted using theory and those observed in the laboratory. The latter problem was corrected by mapping the surface of the axicons using a Zygo microscope and using the Zygo data in place of the specifications to carry out the theoretical calculations. To avoid all problems associated with bulk axicon fabrication errors, phase plates that can be used in place of these specialized axicons have been designed and are currently being tested (see Section 2.2.1).

Additional problems manifest when helical beams are generated using multi-millijoule pulses, which are necessary for the generation of filaments. Although a damage threshold of $500\ mJ/cm^2$ was calculated from ablation test carried out on the phase plates, the phase plates used to induce azimuthal phase lags suffered optical damage at far lower fluences during experiments. When making the first attempt to generate helical filaments, photodarkening on the 5 *mm* azimuthal phase plates was observed for pulse energies in excess of 5 *mJ*. Upon replacing the 5 *mm* phase plates with 10 *mm* phase plates, white light generation, a precursor to more permanent optical damage, was observed for pulse energies in excess of 12 *mJ*. Fortunately, pulse energies of 12 *mJ* proved sufficient for helical filament generation in the latter case. Methods of increasing phase plate area are being investigated to further increase helical beam pulse energy.

Depending on experimental conditions, the RF signals obtained in the filament induced RF radiation experiments would be obscured by other local RF sources. Particularly problematic were the Pockels cells and associated electronics used in the MTFL laser. These systems would generate a burst of RF radiation at approximately the same time the filament induced RF pulses would be observed. RF shielding was found to reduce the Pockels cell noise, but the resulting reduction in RF power was not sufficient to prevent the Pockels cells from obscuring the filament induced pulses. Ultimately, the RF experiments had to be moved to the 50 *m* laser range to place sufficient distance between the Pockels cells and the horn antennas to prevent the Pockels cell noise from contaminating the measurements, and additional RF filters were placed in series with the antenna to better reject Pockels cell noise.

7.2 Future Prospects

The helical beams investigated in Chapter 3 are one among a potentially infinite number of non-diffracting beam structures which can be synthesized through the modification of laser beam wavefronts guided by the understanding of diffraction field. As previously discussed, many such structures have already been investigated, including curving Airy beams and spiraling zero-order Bessel beams. The generation of larger, more complicated non-diffracting beam arrays is a natural extension of this line of research. For some geometries, large beam arrays can be readily obtained. In the case of helical beam synthesis, using vortex plates that provide m^{th} order azimuthal charges in place of unit azimuthal charges will result in arrays of *2m* beams.

Of particular interest is the generation of non-diffracting arrays of composed of two or more concentric rings of beams. If such arrays could be generated with energy sufficient for filamentation, they could be employed as the waveguiding structures described in Chapter 6. Because of the control that would be available using this method, it may be possible to generate geometries suitable for photonic bandgap waveguiding.

7.2.1 Fresnel Axicons

Axicons have proven to be an effective means to generate Bessel beams. However, considerable difficulty has been encountered in fabricating precise double angle axicons required for by the serial configuration used in helical beam synthesis. As an alternative to conventional axicons, the use of Fresnel axicons for Bessel beam generation has been employed. Fresnel axicons are radially symmetric blazed gratings whose first order mode diffracts and an angle identical to that obtained with a conventional axicons. This approach is advantageous in that a double angle axicon can be obtained by fabricating a Frensel axicon using two distinct grating periods. There are problems associated with this approach, as device performance is wavelength specific and dispersion occurs when using the device with ultrafast pulses. Despite these problems, initial test indicate Fresnel axicons yield higher quality beams than their bulk counterpart, and reduce the time and difficulty associated with conducting helical beam experiments significantly.

The use of diffractive gratings also presents an additional approach to the synthesis of helical beams or any other beam structure obtained through the superposition of non-diffracting beams. By making use of multiple grating diffraction modes, two separate non-diffracting beams can be obtained simultaneously, without the need to separate the beam into two separate radial sections. Such an approach could enable the generation of longer helical beams without the need to increase the system aperture. This approach may very well represent to future of non-diffracting beam synthesis and merits future investigation.

7.2.2 Photonic Time-Stretch Microwave Detection

The broadband nature of filament-induced RF radiation investigated in Chapter 5 creates considerable experimental difficult, as the equipment used to analyze the radiation is limited both in bandwidth and sample rate. While the spectra being investigated potentially extends into the THz frequency, the single-shot communication signal analyzer used in the experiment was limited to 4 GHz. Oscilloscopes of greater bandwidth and sample rate are commercially available, but are prohibitively expensive. While the heterodyne system described in Chapter 5 was an effective and cost effective means to circumvent these problems, employing this system is both time consuming and partially dependent upon the shot-to-shot stability of the radiation being investigated.

A technique known as photonic-time stretch has been devised to increase the effective bandwidth and sample rate of analog-to-digital converters by two orders of magnitude [140], achieving effective sample rates as one tera-sample per second [141]. Photonic-time stretch employs broadband electro-optic modulators to modulate chirped ultrafast pulses with an analog signal. This creates and time to wavelength mapping between the analog signal and the ultrafast pulse. By further chirping the ultrafast pulse, the relative temporal duration between different points along the analog signal is increase in proportion to the duration of the ultrafast pulse as the different spectral components of the ultrafast pulse are separated further in time. This has the effect of slowing the dynamic of the analog signal, greatly increasing to time resolution extracted when the signal is analyzed using an analog-to-digital converter.

This technique can be applied to analyze an unknown, fast pulsed microwave signal by routing the signal from a broadband antenna to an electro-optic modulator. This would enable true single-shot analysis of microwave spectra well in excess of 40 GHz. Bandwidth limitations are dictated both by the bandwidth of the microwave front end and by the effective bandwidth of the analog-to-digital signal converter used after the time-stretch, which is a product of the signal converter bandwidth and the stretch factor. A current bandwidth limitation of 100 GHz is estimated [142], based on the maximum bandwidth of state-of-the-art microwave components that are commercially available.

The chief drawback of this method that many analog-to-digital converters operating in parallel are required to analyze a continuous time-stretched signal. However, because the signal of interest are microwave pulses no greater than a few nanoseconds in duration with arbitrary temporal spacing between events, only a single analog-to-digital converter is required. Consequently, photonic-time stretch is far easier and cheaper to implement for this particular application than it is to implement in general.

Cost estimates have been carried out for a preliminary photonic-stretch design intended to enable 100 *GHz* bandwidth single shot measurements to be carried out using our existing 4 *GHz* oscilloscope. System cost estimates, which included the microwave circuitry, optics, and ultrafast laser, but omitting any required antennas, indicate the system could be purchased and assembled for no more than $40,000. This makes the system an attractive alternative to the several hundred thousand dollar single-shot 10-20 *GHz* oscilloscopes which are currently available.

APPENDIX A: PHYSICAL CONSTANTS

Speed of Light: $c = 3.00 \cdot 10^{8}\,\frac{m}{s}$

Permittivity of Free Space: $\epsilon_0 = 8.854 \cdot 10^{-12}\,\frac{F}{m}$

Permeability of Free Space: $\mu_0 = 4\pi \cdot 10^{-7}\,\frac{H}{m}$

Electron Charge: $e = 1.60 \cdot 10^{-19} C$

Electron Mass: $m_e = 9.11 \cdot 10^{-31} kg$

APPENDIX B: GAS PROPERTIES

Air

Density: $\rho_{at} = 1.2\,\frac{kg}{m^3} = 1.2 \cdot 10^{-6}\,\frac{kg}{cm^3}$

Number Density: $N_{at} = 5.16 \cdot 10^{25}\,\frac{1}{cm^3} = 5.16 \cdot 10^{19}\,\frac{1}{cm^3}$

Nitrogen

Ionization Energy: $U_i = 15.576\ eV$

Multiphoton Ionization Cross-Section, 800 nm: $\sigma_{11} = 6.31 \cdot 10^{-140}\,\frac{cm^{22}}{W^{11} \cdot s}$

Oxygen

Ionization Energy: $U_i = 12.063\ eV$

Multiphoton Ionization Cross-Section, 800 nm: $\sigma_8 = 2.81 \cdot 10^{-96}\,\frac{cm^{16}}{W^8 \cdot s}$

APPENDIX C: KNOWN INTEGRALS

$$\int_0^\infty \exp(-q^2x^2)\,dx = \frac{\sqrt{\pi}}{2q}$$

$$\int_0^u \exp(-q^2x^2)\,dx = \frac{\sqrt{\pi}}{2q}\operatorname{erf}(qu)$$

$$\int_0^\infty \exp(-iq^2x^2)\,dx = \frac{\sqrt{\pi}}{2q}\exp\left(-i\frac{\pi}{4}\right)$$

$$\int_0^u \exp(-iq^2x^2)\,dx = \frac{\sqrt{\pi}}{2q}\exp\left(-i\frac{\pi}{4}\right)\operatorname{erf}\left[qu\exp\left(i\frac{\pi}{4}\right)\right]$$

$$\int \exp[-(ax^2+2bx+c)]\,dx = \frac{1}{2}\sqrt{\frac{\pi}{a}}\exp\left(\frac{b^2-ac}{a}\right)\operatorname{erf}\left(\sqrt{a}x-\frac{b}{\sqrt{a}}\right)$$

APPENDIX D: METHOD OF STATIONARY PHASE

Given

$$I = \int f(x) \exp[i\phi(x)]\, dx$$

Then the integral can be approximated by expanding $\phi(x)$ in a Taylor series about x_0 where $\frac{\partial\phi(x_0)}{\partial x} = 0$ and evaluating $f(x)$ at x_0. The Taylor expansion about this point is

$$\phi(x) \approx \phi(x_0) + \frac{1}{2}\frac{\partial^2\phi(x_0)}{\partial x^2}(x - x_0)^2$$

Under these conditions the integral I reduces to

$$I = f(x_0) \exp[i\phi(x_0)] \int \exp\left[\frac{i}{2}\frac{\partial^2\phi(x_0)}{\partial x^2}(x - x_0)^2\right] dx$$

APPENDIX E: NONLINEAR SCHRODINGER EQUATION

The nonlinear Schrodinger equation has been widely applied in literature, and is derived below.

Starting with the wave equation

$$\vec{\nabla} \times \left(\vec{\nabla} \times \vec{E}\right) + \frac{1}{c^2}\frac{\partial^2 \vec{E}}{\partial t^2} = -\frac{1}{\epsilon_0 c^2}\frac{\partial^2 \vec{P}}{\partial t^2} \tag{278}$$

$$\vec{\nabla}^2 \vec{E} - \frac{1}{c^2}\frac{\partial^2 \vec{E}}{\partial t^2} = \frac{1}{\epsilon_0 c^2}\frac{\partial^2 \vec{P}}{\partial t^2} + \vec{\nabla}\left(\vec{\nabla} \cdot \vec{E}\right) \tag{279}$$

where the polarization term is given by

$$\vec{P}(t) = \epsilon_0 \int_{-\infty}^{\infty} \chi_1(t - t_1)\vec{E}(t_1)\partial t_1 + \epsilon_0 \int_{-\infty}^{\infty} \chi_3(t - t_1, t - t_2, t - t_3)\left(\vec{E}(t_1) \cdot \vec{E}(t_2)\right)\vec{E}(t_3)\partial t_1 \partial t_2 \partial t_3 \tag{280}$$

The nonlinear Schrodinger equation is obtained by making the envelope approximation

$$\vec{E} = A(x, y, z)\exp[i(kz - \omega t)]\,\hat{e} + A(x, y, z)\exp[-i(kz - \omega t)]\,\hat{e} \tag{281}$$

For calculations using this approximation, both exponential terms will not be used. Instead, exponential terms will be chosen for each calculation such that the results produce only the positive fundamental frequency. It will further be assumed that the media is polarized in the direction of the electric field, and the incident electromagnetic wave is uniformly polarized. Under such assumptions, the electromagnetic field can be treated as a scalar field.

Let

$$\vec{P}(t) = P(t)\hat{e} \tag{282}$$

correspond to

$$\vec{E}(t) = E(t)\hat{e} \tag{283}$$

and, take

$$\vec{\nabla}\left(\vec{\nabla}\cdot\vec{E}\right) = 0 \tag{284}$$

Under these assumptions the wave equation simplifies to

$$\nabla^2 E - \frac{1}{c}\frac{\partial^2 E}{\partial t^2} = \frac{1}{\epsilon_0 c^2}\frac{\partial^2 P}{\partial t^2} \tag{285}$$

Given the linear susceptibility

$$P_L(t) = \epsilon_0 \int_{-\infty}^{\infty} \chi_1(t - t_1)E(t_1)\partial t_1 \tag{286}$$

and substituting the envelope expansion into the linear susceptibility gives

$$P_L(t) = \epsilon_0 A \exp(ikz) \int_{-\infty}^{\infty} \chi_1(t - t_1)\exp(i\omega t_1)\partial t_1 \tag{287}$$

Making the change of variables$\tau = t - t_1$, and enforce causality, $\chi(t) = 0$ for $t < 0$, then

$$\begin{aligned} P_L &= -\epsilon_0 A \exp[i(kz - \omega t)] \int_{\infty}^{-\infty} \chi_1(\tau)\exp(i\omega\tau)\,\partial\tau \\ &= \epsilon_0 A \exp[i(kz - \omega t)] \int_{-\infty}^{\infty} \chi_1(\tau)\exp(i\omega\tau)\,\partial\tau \end{aligned} \tag{288}$$

apply the definition of the Fourier transform results in

$$P_L = \epsilon_0 A \hat{\chi}_1(-\omega)\exp[i(kz - \omega t)] \tag{289}$$

Assuming that $\chi_1(t)$ is real, $\hat{\chi}_1(\omega) = \hat{\chi}_1(-\omega)$, then

$$P_L = \epsilon_0 A \hat{\chi}_1(\omega)\exp[i(kz - \omega t)] \tag{290}$$

Substituting gives

$$\frac{\partial^2 P_L}{\partial t^2} = -\omega^2 \epsilon_0 A \hat{\chi}(\omega) \exp[i(kz - \omega t)] \tag{291}$$

The nonlinear polarization is given by

$$P_{NL} = \epsilon_0 \int_{-\infty}^{\infty} \chi_3(t - t_1, t - t_2, t - t_3) E(t_1) E(t_2) E(t_3) \partial t_1 \partial t_2 \partial t_3 \tag{292}$$

Substituting into the envelope expansion

$$\begin{gathered} P_{NL} = \ 3\epsilon_0 |A|^2 A \exp(ikz) \\ \cdot \int_{-\infty}^{\infty} \chi_3(t - t_1, t - t_2, t - t_3) \exp(-i\omega t_1) \exp(i\omega t_2) \exp(-i\omega t_3) \partial t_1 \partial t_2 \partial t_3 \end{gathered} \tag{293}$$

and making the change of variables

$$\tau_1 = t - t_1 \tag{294}$$

$$\tau_2 = t - t_2 \tag{295}$$

$$\tau_3 = t - t_3 \tag{296}$$

results in

$$\begin{gathered} P_{NL} = -3\epsilon_0 |A|^2 A \exp[i(kz - \omega t)] \\ \cdot \int_{\infty}^{-\infty} \chi_3(\tau_1, \tau_2, \tau_3) \exp(i\omega \tau_1) \exp(-i\omega \tau_2) \exp(i\omega \tau_3) \, \partial \tau_1 \partial \tau_2 \partial \tau_3 \end{gathered} \tag{297}$$

$$\begin{gathered} P_{NL} = 3\epsilon_0 |A|^2 A \exp[i(kz - \omega t)] \\ \cdot \int_{-\infty}^{\infty} \chi_3(\tau_1, \tau_2, \tau_3) \exp(i\omega \tau_1) \exp(-i\omega \tau_2) \exp(i\omega \tau_3) \, \partial \tau_1 \partial \tau_2 \partial \tau_3 \end{gathered} \tag{298}$$

Applying the definition of the Fourier transform gives

$$P_{NL} = 3\epsilon_0 |A|^2 A \hat{\chi}_3(\omega, -\omega, \omega) \exp[i(kz - \omega t)] \tag{299}$$

Substitution yields

$$\frac{\partial^2 P_{NL}}{\partial t^2} = -3\omega^3 \epsilon_0 |A|^2 A \hat{\chi}_3(\omega, -\omega, \omega) \exp[i(kz - \omega t)] \tag{300}$$

Expanding the Laplacian

$$\nabla^2 E = \frac{\partial^2 E}{\partial z^2} + \nabla_\perp^2 E \tag{301}$$

and substituting the envelope expansion given in Equation 119 into $\nabla^2 E$ yields

$$\nabla^2 E = \left[\frac{\partial^2 A}{\partial z^2} + 2ik\frac{\partial A}{\partial z} - k^2 A + \nabla_\perp^2 A\right] \exp[i(kz + \omega t)] \tag{302}$$

Substituting the envelope expansion into $\frac{\partial^2 E}{\partial t^2}$ gives

$$\frac{\partial^2 E}{\partial t^2} = \frac{\omega^2}{c^2} A \exp[i(kz - \omega t)] \tag{303}$$

Returning to the Helmholtz equation

$$\nabla^2 E - \frac{1}{c^2}\frac{\partial^2 E}{\partial t^2} = \frac{1}{\epsilon_0}\frac{\partial^2 P}{\partial t^2} \tag{304}$$

Substitute the envelope expansion terms and divide by $\exp[i(kz - \omega t)]$

$$\frac{\partial^2 A}{\partial z^2} + 2ik\frac{\partial A}{\partial z} - k^2 A + \nabla_\perp^2 A + \frac{\omega^2}{c^2} A = -\frac{\omega^2}{c^2} A \hat{\chi}_1(\omega) - \frac{3\omega^2}{c^2} |A|^2 A \hat{\chi}_3(\omega, -\omega, \omega) \tag{305}$$

Making the approximation $\left|\frac{\partial^2 A}{\partial z^2}\right| \ll \left|2ik\frac{\partial A}{\partial z}\right|$ and rearranging gives

$$2ik\frac{\partial A}{\partial z} - k^2 A + \nabla_\perp^2 A + \frac{\omega^2}{c^2}[1 + \hat{\chi}_1(\omega)]A = -\frac{3\omega^2}{c^2} |A|^2 A \hat{\chi}_3(\omega, -\omega, \omega) \tag{306}$$

Establishing the dispersion relation

$$k^2 = \frac{\omega^2}{c^2}[1 + \hat{\chi}_1(\omega)] \tag{307}$$

And substitute into the wave equation yields the nonlinear Schrodinger equation.

$$2ik\frac{\partial A}{\partial z} + \nabla_\perp^2 A + 3k^2 \frac{\hat{\chi}_3(\omega, -\omega, \omega)}{1 + \hat{\chi}_1(\omega)}|A|^2 A = 0 \tag{308}$$

APPENDIX F: WAVEGUIDING EQUATIONS

Starting with Maxwell's equations

$$\vec{\nabla} \cdot \vec{E} = 0 \tag{309}$$

$$\vec{\nabla} \cdot \vec{B} = 0 \tag{310}$$

$$\vec{\nabla} \times \vec{E} = -\frac{\partial \vec{B}}{\partial t} \tag{311}$$

$$\vec{\nabla} \times \vec{B} = \frac{1}{c^2}\frac{\partial \vec{E}}{\partial t} \tag{312}$$

Assuming solutions of the form

$$\vec{E} = \vec{E}_0(r,\phi)\exp[i(kz - \omega t)] \tag{313}$$

$$\vec{B} = \vec{B}_0(r,\phi)\exp[i(kz - \omega t)] \tag{314}$$

And expanding in cylindrical coordinates

$$\vec{\nabla} \cdot \vec{E} = \frac{1}{r}(rE_r) + \frac{1}{r}\frac{\partial E_\phi}{\partial \phi} + \frac{\partial E_z}{\partial z} = 0 \tag{315}$$

$$\vec{\nabla} \cdot \vec{B} = \frac{1}{r}(rB_r) + \frac{1}{r}\frac{\partial B_\phi}{\partial \phi} + \frac{\partial B_z}{\partial z} = 0 \tag{316}$$

$$\vec{\nabla} \times \vec{E} = \left[\left(\frac{1}{r}\frac{\partial E_z}{\partial \phi} - ikE_\phi\right)\hat{r} + \left(ikE_r - \frac{\partial E_z}{\partial r}\right)\hat{\phi} + \frac{1}{r}\left(\frac{\partial}{\partial r}\left(rE_\phi\right) - \frac{\partial E_r}{\partial \phi}\right)\hat{z}\right]\exp[i(kz - \omega t)] \tag{317}$$

$$\vec{\nabla} \times \vec{B} = \left[\left(\frac{1}{r}\frac{\partial B_z}{\partial \phi} - ikB_\phi\right)\hat{r} + \left(ikB_r - \frac{\partial B_z}{\partial r}\right)\hat{\phi} + \frac{1}{r}\left(\frac{\partial}{\partial r}\left(rB_\phi\right) - \frac{\partial B_r}{\partial \phi}\right)\hat{z}\right]\exp[i(kz - \omega t)] \tag{318}$$

$$\frac{\partial \vec{E}}{\partial t} = -i\omega E_r \hat{r} - i\omega E_\phi \hat{\phi} - i\omega E_z \hat{z} \tag{319}$$

$$\frac{\partial \vec{B}}{\partial t} = -i\omega B_r \hat{r} - i\omega B_\phi \hat{\phi} - i\omega B_z \hat{z} \tag{320}$$

Solving Maxwell’s equations with this expansion

$$\frac{\partial}{\partial r}\left(rE_\phi\right) - \frac{\partial E_r}{\partial \phi} = i\omega r B_z \tag{321}$$

$$\frac{1}{r}\frac{\partial E_z}{\partial \phi} - ikE_\phi = i\omega B_r \tag{322}$$

$$ikE_r - \frac{\partial E_z}{\partial r} = i\omega B_\phi \tag{323}$$

$$\frac{\partial}{\partial r}\left(rB_\phi\right) - \frac{\partial B_r}{\partial \phi} = -\frac{i\omega r}{c^2} E_z \tag{324}$$

$$\frac{1}{r}\frac{\partial B_z}{\partial \phi} - ikB_\phi = -\frac{i\omega}{c^2} E_r \tag{325}$$

$$ikB_z - \frac{\partial B_z}{\partial r} = -\frac{i\omega}{c^2} E_\phi \tag{326}$$

And rearranging

$$k^2 E_r = k\omega B_\phi - ik\frac{\partial E_z}{\partial r} \tag{327}$$

$$k^2 E_\phi = -k\omega B_r - \frac{ik}{r}\frac{\partial E_z}{\partial \phi} \tag{328}$$

$$\frac{\omega^2}{c^2}B_r = -\frac{k\omega}{c^2}E_\phi - \frac{i\omega}{rc^2}\frac{\partial E_z}{\partial \phi} \tag{329}$$

$$\frac{\omega^2}{c^2}B_\phi = \frac{k\omega}{c^2}E_r + \frac{i\omega}{c^2}\frac{\partial E_z}{\partial r} \tag{330}$$

$$\frac{\omega^2}{c^2}E_r = k\omega B_\phi + \frac{i\omega}{r}\frac{\partial B_z}{\partial \phi} \tag{331}$$

$$\frac{\omega^2}{c^2}E_\phi = -k\omega B_r - i\omega\frac{\partial B_z}{\partial r} \tag{332}$$

$$k^2 B_r = -\frac{k\omega}{c^2}E_\phi - ik\frac{\partial B_z}{\partial r} \tag{333}$$

$$k^2 B_\phi = \frac{k\omega}{c^2}E_r - \frac{ik}{r}\frac{\partial B_z}{\partial \phi} \tag{334}$$

Further rearranging

$$E_r = \frac{i}{\frac{\omega^2}{c^2} - k^2}\left(k\frac{\partial E_z}{\partial r} + \frac{\omega}{r}\frac{\partial B_z}{\partial \phi}\right) \tag{335}$$

$$E_\phi = \frac{i}{\frac{\omega^2}{c^2} - k^2}\left(\frac{k}{r}\frac{\partial E_z}{\partial \phi} - \omega\frac{\partial B_z}{\partial r}\right) \tag{336}$$

$$B_r = \frac{i}{\frac{\omega^2}{c^2} - k^2}\left(k\frac{\partial B_z}{\partial r} - \frac{\omega}{rc^2}\frac{\partial E_z}{\partial \phi}\right) \tag{337}$$

$$B_\phi = \frac{i}{\frac{\omega^2}{c^2} - k^2}\left(\frac{k}{r}\frac{\partial B_z}{\partial \phi} + \frac{\omega}{c^2}\frac{\partial E_z}{\partial r}\right) \quad \textbf{(338)}$$

and substituting

$$\frac{i}{\frac{\omega^2}{c^2} - k^2}\left[\frac{k}{r}\frac{\partial}{\partial r}\left(r\frac{\partial E_z}{\partial r}\right) + \frac{\omega}{r}\frac{\partial^2 B_z}{\partial r \partial \phi} + \frac{k}{r^2}\frac{\partial^2 E_z}{\partial \phi^2} - \frac{\omega}{r}\frac{\partial^2 B_z}{\partial \phi \partial r}\right] + ikE_z = 0 \quad \textbf{(339)}$$

$$\frac{i}{\frac{\omega^2}{c^2} - k^2}\left[\frac{k}{r}\frac{\partial}{\partial r}\left(r\frac{\partial E_z}{\partial r}\right) + \frac{\omega}{r}\frac{\partial^2 B_z}{\partial r \partial \phi} + \frac{k}{r^2}\frac{\partial^2 E_z}{\partial \phi^2} - \frac{\omega}{r}\frac{\partial^2 B_z}{\partial \phi \partial r}\right] + ikE_z = 0 \quad \textbf{(340)}$$

Further rearranging yields

$$\left[\frac{\partial^2}{\partial r^2} + \frac{1}{r}\frac{\partial}{\partial r} + \frac{1}{r^2}\frac{\partial^2}{\partial \phi^2} + \frac{\omega^2}{c^2} - k^2\right]E_z = 0 \quad \textbf{(341)}$$

$$\left[\frac{\partial^2}{\partial r^2} + \frac{1}{r}\frac{\partial}{\partial r} + \frac{1}{r^2}\frac{\partial^2}{\partial \phi^2} + \frac{\omega^2}{c^2} - k^2\right]B_z = 0 \quad \textbf{(342)}$$

REFERENCES

[1] J. M. Cowley, Diffraction Physics, New York: North-Holland, 1981.

[2] A. Yariv and Y. Pochi, Photonics: Optical Electronics in Modern Communications, Sixth Edition, New York: Oxford University Press, 2007.

[3] Z. Bouchal, "Nondiffracting Optical Beams: physical properties, experiments and applications," *Czechoslovak Journal of Physics,* vol. 53, no. 7, pp. 537-578, 2003.

[4] D. McGloin and K. Dholakia, "Bessel beams: diffraction in a new light," *Contemporary Physics,* vol. 46, no. 1, pp. 15-28, 2005.

[5] G. A. Siviloglou, J. Broky, A. Dogariu and Christodoulides, "Observation of Accelerating Airy Beams," *Physical Review Letters,* vol. 99, p. 213901, 2007.

[6] N. Barbieri, M. Weidman, G. Katona, M. Baudelet, Z. Roth, E. Johnson, G. Siviloglou, D. Christodoulides and M. Richardson, "Double helical laser beams based on interfering first-order Bessel beams," *Journal of the Optical Society of Ameria A,* vol. 28, no. 7, pp. 1462-1469, 2011.

[7] B. La Fontaine, F. Vidal, Z. Jiang, C. Y. Chien, D. Comtois, A. Desparois, T. W. Johnston, J.-C. Kieffer and H. Pepin, "Filamentation of ultrashort pulse laser beams resutling from their propagation over long distances in air," *Physics of Plasmas,* vol. 6, no. 5, pp. 1615-1621, 1999.

[8] M. Mazilou, D. J. Stevenson, F. Gunn-Moore and K. Dholakia, "Light beats the spread: "non-diffracting" beams," *Laser Photonics Review,* vol. 4, no. 4, pp. 529-547, 2009.

[9] M. Rodriguez, R. Bourayou, G. Mejean, J. Kasparian, J. Yu, E. Salmon, A. Scholz, B. Stecklum, J. Eisloffel, U. Laux, A. P. Hatzes, R. Sauerbrey, L. Woste and J.-P. Wolf, "Kilometer-range nonlinear propagation of femtosecond laser pulses," *Physical Review E,* vol. 69, p. 036607, 2004.

[10] P. Sprangle, J. R. Penano and B. Hafizi, "Propagation of intense short laser pulses in the atmosphere," *Physical Review E,* vol. 66, p. 046418, 2002.

[11] M. Henriksson, J.-F. Daigle, F. Theberge, M. Chateauneuf and J. Dubois, "Laser guiding of Tesla coil high voltage discharges," *Optics Express,* vol. 20, no. 4, pp. 12721-12728, 2012.

[12] A. E. Dormidonov, V. V. Valuey, V. L. Dmitriev, S. A. Shlenov and V. P. Kandidov, "Laser Filament Induced Microwave Waveguide in Air," *Proceedings of SPIE,* vol. 6733, p. 2S, 2007.

[13] M. Chateauneuf, S. Payeur, J. Dubois and J.-C. Keiffer, "Microwave guiding in air by a cylindrical filament array waveguide," *Applied Physics Letters,* vol. 92, p. 091104, 2008.

[14] A. Ting, K. Krushelnick, H. R. Burris, A. Fisher, C. Manka and C. I. Moore, "Backscattered supercontinuum emission from high-intensity laser-plasma interactions," *Optics Letters,* vol. 21, no. 15, pp. 1096-1098, 1996.

[15] E. V. Suvorov, R. A. Akhmedzhanov, D. A. Fadeev, I. E. Ilyakov, V. A. Mironov and B. V. Shishkin, "Terahertz emission from a metallic surface induced by a femtosecond optic pulse," *Optics Letters,* vol. 37, no. 13, pp. 2520-2522, 2012.

[16] J. S. Pearlman and G. H. Dahlbacka, "Emission of rf radiation from laser-produced plasmas," *Journal of Applied Physics,* vol. 49, no. 1, pp. 457-459, 1978.

[17] H. Nakajima, Y. Shimada, T. Somekawa, M. Fujita and K. A. Tanaka, "Nondestructive Sensor Using Microwaves from Laser Plasma by Subnanosecond Laser Pulses," *IEEE Geoscience and Remote Sensing Letters,* vol. 6, no. 4, pp. 718-722, 2009.

[18] R. R. Musin, M. N. Shneider, A. M. Zheltikov and R. B. Miles, "Guiding radar signals by arrays of laser-induced filaments: finite-difference analysis," *Applied Optics,* vol. 46, no. 23, pp. 5593-5597, 2007.

[19] A. Galvanauskas, M. E. Fermann, D. Harter, K. Sugden and I. Bennion, "All-fiber femtosecond pulse amplification circuit using chirped Bragg gratings," *Applied Physics Letters,* vol. 66, no. 9, pp. 1053-1055, 1995.

[20] A. Anderson, F. Kucking, T. Prikoszovits, M. Hofer, Z. Cheng, C. C. Meacsu, M. Scharrer, S. Rammler, P. S. J. Russell, G. Tempea and A. Assion, "Multi-mJ carrier envelope phase stabilized few-cycle pulses generated by a tabletop laser system," *Applied Physics B: Lasers and Optics,* 2011.

[21] R. Ell, U. Morgner, F. X. Kartner, J. G. Fujimoto, E. P. Ippen, V. Scheuer, G. Angelow, T. Tschudi, M. J. Lederer, A. Boiko and B. Luther-Davies, "Generation of 5-fs pulses and octave-spanning spectra directly from a Ti:sapphire laser," *Optics Letters,* vol. 26, no. 6, pp. 373-375, 2001.

[22] J. Zweiback, T. Ditmire and M. D. Perry, "Femtosecond time-resolved studies of the dynamics of noble-gas cluster explosions," *Physical Review A Rapid Communications,* vol. 59, no. 5, pp. R3166-R3169, 1999.

[23] C. V. Shank, R. Yen and C. Hirlimann, "Time-Resolved Reflectivity Measurements of Femtosecond-Optical Pulse-Induced Phase Transitions in Silicon," *Physical Review Letters,* vol. 50, no. 6, pp. 454-457, 1983.

[24] X. Liu, D. Du and G. Mourou, "Laser Ablation and Micromachining with Ultrashort Laser Pulses," *IEEE Journal of Quantum Electronics,* vol. 33, no. 10, pp. 1706-1716, 1997.

[25] R. R. Gattass and E. Mazur, "Femtosecond laser micromachining in transparent materials," *Nature Photonics,* vol. 2, pp. 219-225, 2008.

[26] T. J. Yu, S. K. Lee, J. H. Sung, J. W. Yoon, T. M. Jeong and J. Lee, "Generation of high-constrast, 30 fs, 1.5 PW laser pulses from chirped-pulse amplification Ti:sapphire laser," *Optics Express,* vol. 20, no. 9, pp. 10807-10815, 2012.

[27] R. W. Boyd, Nonlinear Optics Third Edition, New York: Academic Press, 2008.

[28] J. Kasparian, R. Sauerbrey and S. L. Chin, "The critical laser intensity of self guiding light filaments in air," *Applied Physics B,* vol. 71, pp. 877-879, 2000.

[29] E. T. J. Nibbering, P. F. Curley, G. Grillon, B. S. Prade, M. A. Franco, F. Salin and M. A., "Conical emissions from self-guided femtosecond pulses in air," *Optics Letters,* vol. 21, no. 1, pp. 62-64, 1996.

[30] W. T. Silfvast, Laser Fundamentals Second Edition, Cambridge: Cambridge University Press, 2004.

[31] P. Maine, D. Strickland, P. Bado, M. Pessot and G. Mourou, "Generation of Ultrahigh Peak Power Pulses by Chirped Pulse Amplification," *IEEE Journal of Quantum Electronics,* vol. 24, no. 2, pp. 398-403, 1988.

[32] R. A. Baumgartner and R. L. Byer, "Optical Parametric Amplification," *IEEE Journal of Quantum Electronics,* Vols. QE-15, no. 6, pp. 432-444, 1979.

[33] I. N. Ross, J. L. Collier, P. Matousek, C. N. Danson, D. Neely, R. M. Allott, D. A. Pepler, C. Hernandez-Gomez and K. Osvay, "Generation of terawatt pulses by use of optical parametric chirped pulse amplification," *Applied Optics,* vol. 39, no. 15, pp. 2422-2427, 2000.

[34] P. Heissler, R. Horlein, M. Stafe, J. M. Mikhailova, Y. Nomura, D. Herrmann, R. Tautz, S. G. Rykovanov, I. B. Foldes, K. Varju, F. Tavella, A. Marcinkevicius, F. Krausz, L. Veisz and G. D. Tsakiris, "Toward single attosecond pulses using harmonic emission from solid-density plasmas," *Applied Physics B Lasers and Optics,* 2010.

[35] E. Treacy, "Optical Pulse Compression With Diffraction Gratings," *IEEE Journal of Quantum Electronics,* Vols. QE-5, pp. 454-458, 1969.

[36] P. Beaud, M. Richardson, E. Miesak and B. Chai, "8-TW 90-fs Cr:LiSAF laser," *Optics Letters,* vol. 18, p. 3, 1993.

[37] M. Richardson, S. Grantham, G. K., G. Shimkaveg and P. Beaud, "10-Tw femtosecond laser plasma facility," *Proceedings of SPIE,* vol. 2633, p. 13, 1995.

[38] J. Durnin, J. J. J. Miceli and J. H. Eberly, "Diffraction-Free Beams," *Physical Review Letters,* vol. 58, no. 15, pp. 1499-1501, 1987.

[39] J. Durnin, "Exact solutions for nondiffracting beams. I. The sclar theory," *Journal of the Optical Society of America A,* vol. 4, no. 4, pp. 651-654, 1987.

[40] Z. Bouchal, "Resistance of nondiffracting vortex beam against amplitude and phase perturbations," *Optics Communications,* vol. 210, pp. 155-164, 2002.

[41] Z. Bouchal, J. Wagner and M. Chlup, "Self-reconstruction of a distorted nondiffracting beam," *Optics Communications,* vol. 151, pp. 207-211, 1998.

[42] J. Broky, G. A. Siviloglou, A. Dogariu and D. N. Christodoulides, "Self-healing properties of optical Airy beams," *Optics Express,* vol. 16, no. 17, pp. 12880-12891, 2008.

[43] G. A. Siviloglou and D. N. Christodoulides, "Accelerating finite energy Airy beams," *Optics Letter,* vol. 32, no. 8, pp. 979-981, 2007.

[44] A. Y. Bekshaev, M. S. Soskin and M. V. Vasnetsov, "Angular momentum of a rotating light beam," *Optics Communications,* vol. 249, pp. 367-378, 2005.

[45] V. Jarutis, A. Matijosius, P. Di Trapani and A. Piskarskas, "Spiraling zero-order Bessel beam," *Optics Letters,* vol. 18, no. 9, pp. 2129-2131, 2009.

[46] A. Matijosius, V. Jarutis and A. Piskarskas, "Generation and control of the spiraling zero-order Bessel beam," *Optics Express,* vol. 18, no. 9, pp. 8767-8771, 2010.

[47] Q. Sun, K. Zhou, G. Fang, Z. Liu and S. Liu, "Generation of spiraling high-order Bessel beams," *Applied Physics B,* 2011.

[48] S. A. Baluyot and N. Hermosa II, "Controllable rotation of optical beams with bored helical phases," *Applied Optics,* vol. 49, no. 4, pp. 673-677, 2010.

[49] S. A. Baluyot and N. Hermosa II, "Intensity profiles and propagation of optical beams with bored helical phase," *Optics Express,* vol. 17, no. 18, pp. 16244-16254, 2009.

[50] F. Gori, G. Guattari and C. Padovani, "Bessel-Gauss Beams," *Optics Communications,* vol. 64, no. 6, pp. 491-494, 1987.

[51] D. J. Griffiths, Introduction to Electrodynamics Third Edition, Upper Saddle River: Prentice Hall, 1999.

[52] J.-Y. Lu, "Designing Limited Diffraction Beams," *IEEE Transactions on Ultrasonics, Ferroelectrics, and Frequency Control,* vol. 44, no. 1, pp. 181-193, 1997.

[53] K. Uchara and H. Kituchi, "Generation of Nearly Diffraction-Free Laser Beams," *Applied Physics B,* vol. 48, pp. 125-129, 1989.

[54] K. Ait-Ameur and F. Sachez, "Gaussian beam conversion using an axicon," *Journal of Modern Optics,* vol. 46, no. 10, pp. 1537-1548, 1999.

[55] J. Pu, H. Zhang and S. Nemoto, "Lens axicons illuminated by Gaussian beams for generation of uniform-axial intensity Bessel feilds," *Optical Engineering,* vol. 39, no. 3, pp. 803-807, 2000.

[56] R. Vasilyeu, A. Dudley, N. Khilo and A. Forbes, "Generating superpositions of higher order Bessel beams," 2009.

[57] J. Turunen, A. Vasara and A. T. Friberg, "Holographic generation of diffraction-free beams," *Applied Optics,* vol. 27, no. 19, pp. 3959-3962, 1988.

[58] M. M. Mendez Otero, G. C. Martinez Jimenz, M. L. Arroyo Carrasco, M. D. Iturbe Catillo and E. Marti Panameno, "Generation of Bessel-Gauss beams by means of computer-generated holograms for Bessel beams," 2006.

[59] W.-X. Cong and N.-X. Chen, "Generation of nondiffracting beams by diffractive phase elements," *Journal of the Optical Society of America A,* vol. 15, no. 9, pp. 2362-2364, 1998.

[60] S. Orlov, K. Regelski, V. Smilgevicius and A. Stabinis, "Propagation of Bessel beams carrying optical vortices," *Optical Communications,* vol. 209, pp. 155-162, 2002.

[61] M. W. Beijersbergen, R. P. C. Coerwinkel, M. Kristensen and J. P. Woerdman, "Helical-wavefront laser beams produced with a spiral phase plate," *Optics Communications,* vol. 112, no. 5, pp. 321-327, 1994.

[62] J. Arlt and K. Dholakia, "Generation of high-order Bessel beams by use of an axicon," *Optics Communications,* vol. 177, pp. 297-301, 2000.

[63] V. Jarutis, R. Paskauskas and A. Stabinis, "Focusing of Laguerre-Gaussian beams by axicon," *Optics Communications,* vol. 184, pp. 105-112, 2000.

[64] S. Chavez-Cerda, G. S. McDonald and G. H. C. New, "Nondiffracting beams: travelling, standing, rotating and spiral waves," *Optics Communications,* vol. 123, pp. 225-233, 1996.

[65] S. Chavez-Cerda, Meneses-Nava, M. A. and J. Miguel Hickmann, "Interference of traveling nondiffracting beams," *Optics Letters,* vol. 23, no. 24, pp. 1871-1873, 1998.

[66] T. Cizmar, V. Kollarova, X. Tsampoula, F. Gunn-Moore, Z. Bouchal and K. Dholakia, "Generation and control of multiple Bessel beams for optical micromanipulation," *Proccedings of SPIE,* vol. 7038, p. 70380Q, 2008.

[67] T. Cizmar, V. Kollarova, X. Tsampoula, F. Gunn-Moore, W. Sibbett, Z. Bouchal and K. Dholoakia, "Generation of multiple Bessel beams for a biophotonics workstation," *Optics Express,* vol. 16, no. 18, pp. 14024-14035, 2008.

[68] C. Paterson and R. Smith, "Helicon waves: propagation-invariant waves in rotating coordinate systems," *Optics Communications,* vol. 124, pp. 131-140, 1996.

[69] K. W. Madison, F. Chevy, W. Wohlleben and J. Dalibard, "Vortex Formation in a Stirred Bose-Einstein Condensate," *Physical Review Letters,* vol. 84, no. 5, pp. 806-809, 2000.

[70] L. Paterson, M. P. MacDonald, J. Arlt, W. Sibbett, P. E. Bryant and K. Dholakia, "Controlled Rotation of Optically Trapped Microscopic Particles," *SCIENCE,* vol. 292, pp. 912-914, 2001.

[71] M. P. MacDonald, L. Paterson, K. Volke-Sepulveda, J. Arlt, W. Sibbet and K. Dholakia, "Creation and Manipulation of Three-Dimensional Optically Trapped Structures," *SCIENCE,* vol. 296, pp. 1101-1103, 2002.

[72] S.-H. Lee, Y. Roichman and D. G. Grier, "Optical solenoid beams," *Optics Express,* vol. 18, no. 7, pp. 6988-6993, 2010.

[73] P. Zhang, S. Huang, Y. Hu, D. Hermandez and Z. Chen, "Generation and nonlinear self-trapping of optical propelling beams," *Optics Letters,* vol. 35, pp. 3129-3131, 2010.

[74] A. Greengard, Y. Y. Schechner and R. Piestn, "Depth from diffracted rotation," *Optics Letters,* vol. 32, no. 2, pp. 181-183, 2006.

[75] S. R. P. Pavani, A. Greengard and R. Piestum, "Three-dimensional localization with nanometer accuracy using a detector-limited double-helix point spread function system," *Applied Physics Letters,* vol. 95, no. 2, p. 021103, 2009.

[76] S. R. P. Pavani, M. A. Thompson, J. S. Biteen, S. J. Lord, N. Liu, R. J. Twieg, R. Piestun and W. Moerner, "Three-dimensional, single-molecule fluorescence imaging beyond the diffraction limit by using a double-helix point spread function," *PNAS,* vol. 106, no. 9, pp. 2995-2999, 2009.

[77] C. Rotschild, S. M., A. Barak, R. A. El-Ganainy, E. Lifshitz, D. N. Christodoulides and M. Segev, "Complex Nonlinear Optp-Fluidity," *Frontiers in Optics, OSA Technical Digest,* 2008.

[78] T. Carmon, R. Uzdin, C. Pigier, Z. H. Musslimani, M. Segev and A. Nepomnyashchy, "Rotating Propeller Solitions," *Physical Review Letters,* vol. 87, no. 14, p. 143901, 2001.

[79] A. S. Desyatnikov and Y. S. Kivshar, "Rotating Optical Soliton Clusters," *Physical Review Letters,* vol. 88, no. 5, p. 053901, 2002.

[80] A. S. Desyatnikov, D. Buccoliero, M. R. Dennis and Y. S. Kivshar, "Suppression of Collapse for Spiraling Elliptic Soltions," *Physical Review Letters,* vol. 104, no. 5, p. 053902, 2010.

[81] M. Pitchumani, H. Hockel, W. Mohammed and E. G. Johnson, "Additive lithography for fabrication of diffractive optics," *Applied Optics,* vol. 41, no. 29, pp. 6176-6181, October 2002.

[82] A. Couairon and A. Mysyrowicz, "Femtosecond filamentation in transparent media," *Physics Reports,* vol. 441, pp. 47-189, 2007.

[83] A. Talebpour, J. Yang and S. Chin, "Semi-empirical model for the rate of tunnel ionization of N2 and O2 molecules in an intense Ti:Sapphire laser pulse," *Optics Communications,* vol. 163, pp. 29-32, 1999.

[84] A. Braun, G. Korn, X. Liu, D. Du, J. Squier and G. Mourou, "Self-channeling of high-peak-power femtosecond laser pulses in air," *Optics Letters,* vol. 20, no. 1, pp. 73-75, 1995.

[85] S. L. Chin, S. A. Hosseinim, W. Liu, Q. Luo, F. Theberge, N. Abozbek, A. Becker, V. P. Kandidov, O. G. Kosareava and H. Schroeder, "The propagation of powerful femtosecond laser pulses in optical media: physics, application, and new challenges," *Canadian Journal of Physics,* vol. 83, pp. 863-905, 2005.

[86] W. Liu and S. L. Chin, "Direct measurement of the critical power of femtosecond Ti:sapphire laser pulse in air," *Optics Express,* vol. 13, no. 15, pp. 5750-5755, 2005.

[87] R. Y. Chiao, E. Garmire and C. H. Townes, "Self-Trapping of Optical Beams," *Physical Review Letters,* vol. 13, no. 15, pp. 479-482, 1964.

[88] K. D. Moll and A. L. Gaeta, "Self-Similar Optical Wave Collapse: Observation of the Townes Profile," *Physical Review Letters,* vol. 90, no. 20, p. 203902, 2003.

[89] H. Yang, J. Zhang, Y. Li, J. Zhang, Y. Li, Z. Chen, H. Teng, Z. Wei and Z. Sheng, "Characteristics of self-gudied laser plasma channels generated by femtosecond laser pulses in air," *Physical Review E,* vol. 66, no. 1, p. 016406, 2002.

[90] S. Tzortzakis, M. A. Franco, Y.-B. Andre, A. Chiron, B. Lamouroux, B. Prade and Mysyrowicz, "Formation of a conducting channel in air by self-guided femtosecond laser pulses," *Physical Review E,* vol. 60, no. 4, pp. R3505-R3507, 1999.

[91] J.-F. Daigle, A. Jaron-Becker, S. Hosseini, T.-J. Wang, Y. Kamali, G. Roy, A. Becker and S. L. Chin, "Intensity clamping measurement of laser filaments in air at 400 and 800 nm," *Physical Review A,* vol. 82, no. 2, p. 023405, 2010.

[92] A. A. Ionin, S. I. Kudryashov, S. V. Makarov, L. V. Seleznev and D. V. Sinitsyn, "Multiple Filamentation of Intense Femtosecond Laser Pulses in Air," *JETP Letters,* vol. 90, no. 6, pp. 423-427, 2009.

[93] Z.-Q. Hao, J. Zhang, X. Lu, T.-T. Xi, Y.-T. Li, X.-H. Yuan, Z.-Y. Zheng, Z.-H. Wang, W.-J. Ling and Z.-Y. Wei, "Spatial evolution of multiple filaments in air induced by femtosecond laser pulses," *Optics Express,* vol. 14, no. 2, pp. 773-778, 2006.

[94] W. Liu, J.-F. Gravel, F. Theberge, A. Becker and S. Chin, "Background reservoir: its crucial role for long-distance propagation of femtosecond laser pulses in air," *Applied Physics B: Lasers and Optics,* vol. 80, pp. 857-860, 2005.

[95] S. Eisenmann, J. Penano, P. Sprangle and A. Zigler, "Effect of an Energy Reservoir on the Atmospheric Propagation of Laser-Plasma Filaments," *Physical Review Letters,* vol. 100, no. 15, p. 155003, 2008.

[96] M. Kolesik and J. V. Moloney, "Self-healing femtosecond light filaments," *Optics Letters,* vol. 29, no. 6, pp. 590-592, 2004.

[97] F. Courvoisier, V. Boutou, J. Kasparian and E. Salmon, "Ultraintense light filaments transmitted through clouds," *Applied Physics Letters,* vol. 83, no. 2, pp. 213-215, 2003.

[98] M. L. Boas, Mathematical Methods in the Physical Sciences Second Edition, New York: John

Wiley & Sons, Inc., 1983.

[99] G. P. Agrawal, Nonlinear Fiber Optics, San Diego: Academic Press, Inc., 1989.

[100] K. Konno and H. Suzuki, "Self-Focussing of Laser Beam in Nonlinear Media," *Physica Scripta,* vol. 20, pp. 382-386, 1979.

[101] H. D. Ladouceur, A. P. Baronavski, D. Lohrmann, P. W. Grounds and P. G. Girardi, "Electrical conductivity of a femtosecond laser generated plasma channel in air," *Optics Communications,* vol. 189, pp. 107-111, 2001.

[102] A. Couairon, "Dynamics of femtosecond filamentation from saturation of self-focusing laser pulses," *Physical Review A,* vol. 68, no. 1, p. 015801, 2003.

[103] D. Faccio, A. Matijosius, A. Dubietis, R. Piskarskas, A. Varanavicius, E. Gaizauskas, A. Piskarskas, A. Couairon and P. Di Trapani, "Near- and far-field evolution of laser pulse filaments in Kerr media," *Physical Review E,* vol. 72, no. 3, p. 037601, 2005.

[104] P. Polykin, M. Kolesik, A. Roberts, D. Faccio, P. Di Trapani and J. Moloney, "Generation of extended plasma channels in air using femtosecond Bessel beams," *Optics Express,* vol. 16, no. 20, pp. 15733-15740, 2008.

[105] D. Abdollahpour, P. Panagiotopoulos, M. Turconi, O. Jedrkiewicz, D. Faccio, P. Di Trapani, A. Couairon, D. G. Papazoglou and S. Tzortzakis, "Long spatio-temporally stationary filaments in air using short pulse UV laser Bessel beams," *Optics Express,* vol. 17, no. 7, pp. 5052-5057, 2009.

[106] S. Akturk, B. Zhou, M. Franco, A. Couairon and A. Mysyrowicz, "Generation of long plasma channels in air by foucisng ultrashort laser pulses with an axicon," *Optics Communications,* vol. 282, pp. 129-134, 2009.

[107] P. Polynkin, M. Kolesik and J. Moloney, "Extended filamentation with temporally chirped femtosecond Bessel-Gauss beams in air," *Optics Express,* vol. 17, no. 2, pp. 575-584, 2009.

[108] P. Polynkin, M. Kolesik, J. V. Molony, G. A. Siviglou and D. N. Christodoulides, "Curved Plasma Channel Generation Using Ultraintense Airy Beams," *SCIENCE,* vol. 324, pp. 229-232, 2009.

[109] P. Polynkin, M. Kolesik and J. Moloney, "Filamentation of Femtosecond Laser Airy Beams in Water," *Physical Review Letters,* vol. 103, p. 123902, 2009.

[110] H. Nakajima, Y. Shimada, T. Somekawa, M. Fujita and K. A. Tanaka, "Nondestructive Sensor Using Microwaves from a Laser Plasma," *Plasma and Fusion Research: Letters,* vol. 4, p. 003,

2009.

[111] H. Hamster, A. Sullivan, S. Gordon, W. White and R. W. Falcone, "Subpicosecond Electromagnetic Pulses from Intense Laser-Plasm Interaction," *Physical Review Letters,* vol. 71, no. 17, pp. 2725-2728, 1993.

[112] C.-C. Cheng, E. M. Wright and J. V. Moloney, "Generation of Electromagnetic Pulses from Plasma Channels Induced by Femtosecond Light Strings," *Physical Review Letters,* vol. 87, no. 21, p. 213001, 2001.

[113] S. Tzortzakis, G. Mechain, G. Patalano, Y.-B. Andre, P. B., M. Franco and Mysyrowicz, "Coherent subterahertz radiation from femtosecond infrared filaments in air," *Optics Letters,* vol. 27, no. 21, pp. 1944-1946, 2002.

[114] P. Sprangle, J. R. Penano, B. Hafizi and C. A. Kapetanakos, "Ultrashort laser pulses and electromagnetic pulse generation in air and on dielectric surfaces," *Phyiscal Review E,* vol. 69, p. 066415, 2004.

[115] B. Forestier, A. Houard, M. Durand, Y. B. Andre, B. Prade, J.-Y. Dayignac, F. Perret, C. Pichot, M. Pellet and A. Mysyrowicz, "Radiofrequency conical emission from femtosecond filaments in air," *Applied Physics Letters,* vol. 96, p. 141111, 2010.

[116] F. S. Felber, "Dipole radio-frequency power from laser plasmas with no dipole moment," *Applied Physics Letters,* vol. 86, p. 231501, 2005.

[117] Z.-Y. Chen, J.-F. Li, J. Li and Q.-X. Peng, "Microwave radiation mechanims in a pulse-laser irradiated Cu foil target revisited," *Physica Scripta,* vol. 83, p. 055503, 2011.

[118] D. von der Linde and H. Schuler, "Breakdown threshold and plasma formation in femtosecond laser-solid interaction," *Journal of the Optical Society of America B,* vol. 13, no. 1, pp. 216-222, 1996.

[119] D. von der Linde, K. Sokolowski-Tinten and J. Bialkowski, "Laser-solid interaction in the femtosecond time regime," *Applied Surface Science,* vol. 109, no. 110, pp. 1-10, 1997.

[120] Z. Chen and S. S. Mao, "Femtosecond laser-induced electronic plasma at metal surfaces," *Applied Physics Letters,* vol. 93, p. 051506, 2008.

[121] Z. Chen and A. Bogaerts, "Laser ablation of Cu and plume expansion into 1 atm ambient gas," *Journal of Applied Physics,* vol. 97, p. 063305, 2005.

[122] K. Furusawa, K. Takahashi, H. Kumagai, K. Midorikawa and M. Obara, "Ablation characteristics of Au, Ag, and Cu metals using a femtosecond Ti:sapphire laser," *Applied Physics A,* vol. 69, pp. S359-S366, 1999.

[123] D. R. Lide, CRC Handbook of Chemistry and Physics, 82nd Edition, CRC Press, 2001.

[124] D. E. Eastman, "Photoelectric Work Functions of Transition, Rare-Earth, and Noble Metals," *Physical Review B,* vol. 2, no. 1, pp. 1-2, 1970.

[125] E. G. Gamaly, A. V. Rode, V. T. Tikhonchuk and B. Luther-Davies, "Ablation of solids by femtosecond lasers: ablation mechanism and ablation thresholds for metals and dielectrics," *Physical Review A,* 2001.

[126] S. Luan, H. Hippler, H. Schwier and H. O. Lutz, "Electron Emission from Polycrystalline Copper Surfaces by Multi-Photon Absorption," *Europhysics Letters,* vol. 9, no. 5, pp. 489-494, 1989.

[127] M. Lenzner, J. Kruger, S. Sartania, Z. Cheng, C. Spielman, G. Mourou, E. Kautek and F. Krausz, "Femtosecond Optical Breakdwon in Dielectrics," *Physical Review Letters,* vol. 80, no. 18, pp. 4076-4079, 1998.

[128] C. A. Balanis, Antenna Theory: Analysis and Design Second Edition, John Wiley & Sons, Inc., 1997.

[129] J. D. Jackson, Classical Electrodynamics Third Edition, John Wiley & Sons, Inc., 1988.

[130] M. Rodriguez, R. Sauerbrey, H. Wille, L. Woste, T. Fujii, Y.-B. Andre, A. Mysyrowicz, L. Klingbeil, K. Rethmeier, W. Kalkner, J. Kasparian, E. Salmon, J. Yu and J.-P. Wolf, "Triggering and guiding megavolt discharges by use of laser-induced ionized filaments," *Optics Letters,* vol. 27, no. 9, pp. 772-774, 2002.

[131] N. A. Bogatov, A. I. Kuznetsov, A. I. Smimov and A. N. Stepanov, "Propagation of Microwave Signals along a Two-Wire Line with a Laser Filament for a Conductor," *18th International Conference on Microwave and Telecommunication Technology,* p. 739, 2008.

[132] P. Polesana, M. Franco, A. Couairon, D. Faccio and P. Di Trapani, "Filamentation in Kerr media from pulsed Bessel beams," *Physical Review A,* vol. 77, p. 043814, 2008.

[133] S. Akturk, B. Zhou, B. Pasquiou, A. Houard, M. Franco, A. Couairon and A. Mysyrowicz, "Generation of long plasma channels in air by using axicon-generated Bessel beams," in *CLEO/QELS*, 2008.

[134] J. Fan, E. Parra, I. Alexeev, K. Y. Kim, H. M. Milchberg, L. Y. Margolin and L. N. Pyatnitskii, "Tubular plasma generation with a high-power hollow Bessel beam," *Physical Review E,* vol. 62, no. 6, pp. R7603-R7606, 2000.

[135] K. Chang, RF and Microwave Wireless Systems, New York: John Wiley & Sons, Inc., 2000.

[136] B. Zhou, S. Akturk, B. Prade, Y.-B. Andre, A. Houard, Y. Liu, M. Franco, C. D'Amico, E. Salmon, Z.-Q. Hao, N. Lascoux and A. Mysyrowicz, "Revival of femtosecond laser plasma filaments in air by a nanosecond laser," *Optics Express,* vol. 17, no. 14, pp. 11450-11456, 2009.

[137] B. Zhou, S. Akturk, B. Prade, Y.-B. Andre, A. Houard, Y. Liu, M. Franco, C. D'Amico, E. Salmon, Z.-Q. Hao, N. Lascoux and A. Mysyrowicz, "Long Time Revival of femtosecond laser plasma filaments in air," in *OSA/CLEO/IQEC*, 2009.

[138] X.-L. Liu, X. Lu, J.-L. Ma, L.-B. Feng, X.-l. Ge, Y. Zheng, Y.-T. Li, L.-M. Chen, Q.-L. Dong, W.-M. Wang, Z.-H. Wang, H. Teng, Z.-Y. Wei and J. Zhang, "Long lifetime air plasma channel generated by femtosecond laser pulse sequence," *Optics Express,* vol. 20, no. 6, pp. 5968-5973, 2012.

[139] S. Shiffler, P. Polynkin and J. Moloney, "Self-focusing of femtosecond diffraction-resistant vortex beams in water," *Optics Letters,* vol. 36, no. 19, pp. 3834-3836, 2011.

[140] F. Coppinger, A. S. Bhushan and B. Jalali, "Photonic Time Stretch and Its Application to Analog-to-Digital Conversion," *IEEE Transactions on Microwave Theory and Techniques,* vol. 47, no. 7, pp. 1309-1314, 1999.

[141] Y. Han, O. Boyraz and B. Jalali, "Tera-sample per second real-time waveform digitizer," *Applied Physics Letters,* vol. 87, no. 24, p. 241116, 2005.

[142] D. Chen, H. R. Fetterman, A. Chen, W. H. Steier, L. R. Dalton, W. Wang and Y. Shi, "Demonstration of 110 GHz electo-optic polymer modulators," *Applied Physics Letters,* vol. 70, no. 25, pp. 3335-3337, 1997.

[143] B. C. Stuart, M. D. Feit, S. Herman, A. M. Ribenchik, B. W. Shore and M. D. Perry, "Optical ablation by high-power short-pulse lasers," *Journal of the Optical Society of America B,* vol. 13, no. 2, pp. 459-468, 1996.

[144] P. Martin, S. Vivirito and G. Petite, "Photo-induced processes in laser irradiation of a metal surface," *Journal of Physics B,* vol. 33, pp. 767-782, 2000.